mathematics

Article

Mathematical Modeling and Simulation of Energy-Constrained Pavement Crack Maintenance Using XFEM-Based Crack Evolution and AI-Driven Repair Strategy Optimization

Nawal Louzi [1], Mohammad Q. Al-Jamal [2,*], Mahmoud AlJamal [3], Ayoub Alsarhan [4], Nayef H. Alshammari [5], Khalid Hamad Alnafisah [6], Mohammed Kamel Aleinzi [7] and Sami Aziz Alshammari [8,*]

1 Civil Engineering Department, Al-Ahliyya Amman University, Amman 19111, Jordan; n.alouzi@ammanu.edu.jo
2 Department of Renewable Energy, Technical Faculty, Jadara University, P.O. Box 733, Irbid 21110, Jordan
3 Department of Cybersecurity, Science and Information Technology, Irbid National University, Irbid 21110, Jordan; m.aljamal@inu.edu.jo or mahmood.yj.98@gmail.com
4 Department of Information Technology, Faculty of Prince Al-Hussien bin Abdullah, The Hashemite University, Zarqa 13133, Jordan; ayoubm@hu.edu.jo
5 Department of Computer Science, Faculty of Computers and Information Technology, University of Tabuk, Tabuk 47512, Saudi Arabia; nh.alshammari@ut.edu.sa
6 Department of Computer Sciences, Faculty of Computing and Information Technology, Northern Border University, Rafha 91431, Saudi Arabia; khalid.alnafisah@nbu.edu.sa
7 Department of Information Systems, Faculty of Computing and Information Technology, Northern Border University, Rafha 91431, Saudi Arabia
8 Department of Information Technology, Faculty of Computing and Information Technology, Northern Border University, Rafha 91431, Saudi Arabia
* Correspondence: m.aljamal@jadara.edu.jo (M.Q.A.-J.); sami.alshammari@nbu.edu.sa (S.A.A.)

Abstract

This study presents a mathematical modeling and simulation framework for pavement crack maintenance under limited work zone energy availability. The framework combines crack evolution, thermal repair, interface behavior, and maintenance decision-making within a unified structural–thermal–energy formulation. A three-dimensional multilayer flexible pavement model is developed with an XFEM-enriched region in the aged asphalt surface layer, a localized repair zone, cohesive interface behavior, and wheel-loading stages before and after maintenance. Rather than assuming constant heating, the repair heat flux is governed by a photovoltaic battery-dependent amplitude function, allowing the model to reflect practical variations in available energy. The simulation generated a dataset containing crack geometry, pavement properties, repair zone dimensions, loading conditions, heat flux intensity, heating duration, bonding quality, XFEM damage status, stress response, temperature distribution, interface damage, energy feasibility, durability, and service life gain. These variables were used to develop the Crack–Energy–Repair Interaction Graph Network (CERIG-Net), which represents each maintenance case as a physics-guided heterogeneous graph and ranks delayed repair, crack sealing, localized patching, thin overlay, and deep repair. The thin overlay strategy reduced final crack length from 94.7 mm to 53.8 mm, lowered maximum stress from 3.85 MPa to 2.22 MPa, achieved a durability index of 0.86, and extended service life by 6.7 years.

Keywords: mathematical modeling; pavement infrastructure; XFEM crack propagation; energy-constrained maintenance; AI-based repair optimization

MSC: 74S05; 74R10; 74F05; 68T07; 90C29

Academic Editor: Noureddine Lakouari

Received: 12 July 2026
Revised: 19 August 2026
Accepted: 22 August 2026
Published: 1 September 2026

1. Introduction

Road pavements form a major part of transportation infrastructure and require continuous maintenance in order to remain safe, reliable, and economically serviceable. Their condition gradually declines under repeated traffic loading, temperature variation, moisture exposure, material aging, and accumulated structural damage. Among the different forms of pavement deterioration, cracking is particularly important because a small surface defect can develop into a wider structural problem. Once initiated, a crack may propagate through the asphalt layers, increase local stress concentration, weaken the surrounding material, and create paths for water infiltration, which further accelerates pavement deterioration [1]. Timely maintenance can slow this process, but selecting the appropriate repair strategy remains difficult because conventional decisions are commonly based on visual inspection, empirical indices, or generalized deterioration thresholds. Although these approaches are useful for routine assessment, they may not describe the local fracture processes that control crack growth or explain how the pavement responds after repair [2]. A more detailed simulation-based approach is needed to represent crack evolution, repair activation, stress redistribution, and post-maintenance performance under realistic operating conditions.

Mathematical and numerical modeling provide an effective means of examining pavement behavior before physical maintenance is carried out. Finite-element analysis can represent pavement as a multilayer structural system and account for material properties, boundary conditions, traffic loading, repair geometry, and localized damage within a controlled computational environment [3]. The extended finite-element method (XFEM) is especially useful for crack analysis because it can simulate crack initiation and propagation without repeatedly changing the finite-element mesh as the crack path develops [4]. Recent studies have also highlighted the influence of temperature on pavement crack evolution [5]. In parallel, photovoltaic systems have gained attention in pavement-related energy applications because road surfaces provide a large area for renewable energy harvesting [6]. However, these research directions are usually examined separately. Many numerical investigations concentrate on crack mechanics, repair geometry, or stress redistribution, while the energy required to carry out the repair is commonly assumed to be continuously available.

This assumption can be restrictive in practical pavement maintenance. The success of a thermally assisted repair depends not only on the selected treatment but also on the energy available at the work zone, the heating duration, the temperature reached within the repair area, and the bond formed between the existing pavement and the repair material. Crack sealing studies have shown that material condition, failure mechanism, and treatment quality strongly influence maintenance performance [1]. simulations of patched pavement have likewise demonstrated that repair geometry and loading position can alter stress concentration, crack development, and interface response [7]. At the same time, pavement-based renewable energy technologies are receiving increasing attention because road surfaces offer considerable potential for solar, thermal, piezoelectric, and thermoelectric energy harvesting [8]. Nevertheless, the power supplied by a photovoltaic battery system may vary during maintenance and may not support a constant heat input throughout the treatment period. Consequently, a repair strategy that performs well under ideal heating conditions may become less effective or even infeasible when practical energy limitations are considered. Recent energy-aware engineering research has shown the value of linking physical performance with energy-efficient design decisions [9]. Related system-level studies have also emphasized the importance of combining environmental objectives, lifecycle considerations, and intelligent decision support in a unified framework [10]. These considerations motivate a coupled pavement model that accounts for structural deterioration, thermal conditioning, energy availability, interface performance, and long-term repair effectiveness.

https://doi.org/10.3390/math14173149

The present study addresses this need by formulating pavement crack maintenance as a structural and thermal energy modeling and optimization problem. A three-dimensional multilayer flexible pavement model is developed with an XFEM-enriched crack region in the aged asphalt surface layer, a localized repair zone, cohesive repair interface behavior, and wheel-loading stages before and after maintenance. Recent numerical studies have confirmed the usefulness of finite-element modeling for examining crack development under realistic pavement conditions [5]. Other investigations have shown that patch configuration can significantly affect stress redistribution and the post-repair mechanical response of asphalt pavement [7]. Mixed-mode fracture research has further demonstrated the importance of representing crack opening, sliding, fracture–energy interaction, and progressive damage when simulating material failure [11]. In the proposed framework, the thermal repair process is controlled through an energy-dependent heat flux amplitude rather than an ideal constant heat source. The simulation can distinguish between cases receiving sufficient photovoltaic battery energy and cases in which thermal conditioning is restricted by the available work zone energy. The modeled responses include crack growth, XFEM damage state, maximum principal stress, vertical displacement, repair zone temperature, interface stress, interface damage, repair durability, energy feasibility, and expected service life improvement. Together, these outputs describe how pavement condition, repair energy, bonding quality, and post-repair structural performance interact.

Although multiphysics simulations can explain pavement behavior under different repair conditions, maintenance planning also requires a consistent method for comparing alternative treatments. Recent reviews have shown that machine learning techniques are increasingly used in pavement management for condition assessment, deterioration prediction, maintenance planning, and infrastructure decision support [12]. More recently, graph-based learning has been introduced into pavement engineering to capture relational information that conventional tabular learning architectures do not explicitly represent. Existing graph convolutional and spatiotemporal graph approaches have mainly been applied to pavement condition prediction, roadway spatial dependencies, deterioration forecasting, and preventive maintenance support [13,14]. Graph neural networks have also been investigated as computational surrogates for predicting three-dimensional pavement structural responses from finite element-generated data, including physics-informed formulations in which mechanical constraints are incorporated into the learning process [15,16]. These developments demonstrate the potential of graph learning in pavement engineering; however, their graph representations are primarily designed for road network relationships, condition evolution, or structural response approximation rather than for modeling the coupled mechanisms governing a localized crack repair operation.

Nevertheless, many existing pavement-management approaches still process condition indicators as independent tabular variables or focus on only one part of the pavement deterioration and maintenance process. As such, they do not explicitly integrate the physical relationships among crack state, material properties, thermal treatment, energy availability, repair interface condition, structural recovery, and maintenance outcome within a single decision model. To address this limitation, the present study introduces the Crack–Energy–Repair Interaction Graph Network (CERIG-Net). Each simulated maintenance case is expressed as a physics-guided heterogeneous graph containing crack state, material property, energy availability, thermal conditioning, repair interface, structural response, and repair strategy nodes. Information is exchanged through graph message passing and attention-based interaction learning, while physics-guided constraints preserve consistency among the predicted structural, thermal, and energy responses. The distinguishing characteristic of CERIG-Net consists of the physical semantics assigned to its heterogeneous graph and the maintenance decision problem represented by that graph. Unlike graph formulations in which nodes primarily correspond to roadway segments, pavement locations, computational points, or general condition indicators, CERIG-Net represents the interacting physical and operational domains of an individual pavement repair event. The graph preserves the causal progression from crack geometry and material state to structural response, energy-dependent thermal conditioning, repair interface bonding, post-repair deterioration, durability, and maintenance decision. In this way, it integrates XFEM crack evolution, fracture properties, PV-battery energy availability, repair zone heating, cohesive interface degradation, structural recovery, and service life response within a unified graph learning architecture. Moreover, unlike pavement GNN surrogate models that terminate at condition or structural response prediction, CERIG-Net combines multi-output physical response prediction with energy feasibility assessment, predictive uncertainty estimation, and physics-constrained ranking of competing maintenance strategies. The model predicts the main repair performance indicators and ranks delayed repair, crack sealing, localized patching, thin overlay, and deep repair according to crack growth control, stress reduction, energy feasibility, interface durability, and service life extension.

The main contributions of this study are summarized as follows:

- A unified simulation-to-decision framework couples XFEM crack evolution, repair interface damage, energy-constrained thermal conditioning, and post-repair pavement performance.
- A repair model incorporating a photovoltaic battery directly links available energy to heat delivery, bonding quality, structural recovery, durability, and repair feasibility.
- CERIG-Net introduces a physics-guided heterogeneous crack–energy–repair graph in which crack state, material properties, energy availability, thermal conditioning, repair interface behavior, structural response, and candidate maintenance actions are represented as physically connected node types. Unlike pavement GNNs developed primarily for condition forecasting or structural response approximation, CERIG-Net jointly performs multi-physics repair response prediction, uncertainty-aware energy feasibility assessment, and physics-constrained maintenance strategy ranking under structural, thermal, interface, energy, durability, and service life requirements.

2. Literature Review

Wang et al. [7] investigated the mechanical performance of patched asphalt pavements with different patching shapes using two-dimensional and three-dimensional finite-element simulations. Their study addressed the problem that differences between patched and unpatched asphalt mixtures can generate stress and strain concentrations near the repair interface, which may accelerate secondary cracking and interface debonding. The objective of their work was to evaluate how rectangular, stair-shaped, and trapezoidal patch geometries affect crack propagation, thermal stress behavior, and interface debonding in repaired asphalt pavement. Numerically, their study used finite-element models to simulate top-down and bottom-up crack propagation, thermal cooling from approximately 150 °C to 30 °C, and interface debonding behavior under different tire loading positions. Their findings showed that patching shape meaningfully affects the internal mechanical response of patched pavement, especially the distribution of stress concentration, crack propagation tendency, and interface debonding risk. These findings confirm that the repair zone should not be treated as a simple uniform patch but as a geometrically and mechanically active part of the pavement system. However, their work focused mainly on patch shape mechanics and did not integrate energy-limited repair heating, PV battery-controlled heat flux, cohesive thermal repair interface behavior, or AI-based ranking of repair strategies. The present study extends this direction by coupling XFEM crack evolution, energy-constrained thermal conditioning, repair interface damage, and CERIG-Net repair strategy optimization within a single simulation-driven framework.

Du et al. [17] examined the influence of patching on asphalt pavement cracking performance using a macrostructure-based heterogeneous finite-element method. Their research problem was that asphalt patching changes the local material continuity and structural composition of the pavement, which can alter crack resistance, crack path development, and stress redistribution, while many conventional repair analyses simplify patched pavements as homogeneous systems. Their objective was to evaluate the effect of asphalt patching mixture on cracking performance under service loading conditions. Numerically, the authors established a heterogeneous asphalt pavement-patching mixture model in ABAQUS and used XFEM to characterize crack propagation from a predefined initial crack. Their findings showed that patching characteristics affect crack resistance and stress redistribution, demonstrating that finite-element and XFEM-based simulation can provide a more realistic understanding of repaired pavement cracking behavior than simplified empirical repair assessment. However, their work remained focused on mechanical cracking response and did not consider repair heating as an energy-constrained process. It also did not connect XFEM outputs with thermal conditioning, interface bonding quality, energy feasibility, or AI-based selection among multiple repair strategies. The present study addresses this limitation by generating coupled XFEM, thermal, interface, and energy feasibility outputs, which are used to train CERIG-Net for optimal pavement repair strategy selection.

Zhang et al. [18] studied solar energy harvesting from photovoltaic/thermal pavement systems and evaluated their energy performance while considering ground influence. Their research problem was that while pavement-integrated PV/T systems can harvest solar and thermal energy, their performance is highly dependent on operating conditions such as solar irradiance, water flow rate, water tank capacity, heat exchange, and ground interaction. The objective of the study was to quantify the energy behavior of PV/T pavement and identify how operating parameters affect thermal efficiency and energy output. Their numerical findings showed that a water flow rate higher than 0.2 L/s was recommended for a 100 L water tank and that the system thermal efficiency could reach 41.47% under 1000 W/m^2 solar irradiance, with ground influence estimated at 11.38%. They also reported that small water tanks may lead to higher water temperature but lower system thermal efficiency, with values of approximately 9.3% and 12.17% for the compared metropolitan cases. These results confirm the importance of considering energy availability and operating conditions in pavement-integrated renewable energy systems. However, their study focused on harvesting energy from pavement rather than using available PV-battery energy as a direct operational constraint for pavement crack repair. The present study builds on this energy-aware pavement direction by converting PV-battery availability into an energy-limited repair heat flux amplitude that controls thermal conditioning, interface bonding quality, repair feasibility, and post-repair durability.

Chen et al. [8] reviewed technologies and efficiencies for harvesting energy from pavements, including asphalt solar collectors, photovoltaic pavements, piezoelectric systems, and thermoelectric generators. Their study addressed the problem that pavements are large exposed infrastructure surfaces capable of harvesting solar, thermal, and mechanical energy, but different harvesting technologies vary in efficiency, maturity, environmental sensitivity, and practical applicability. The objective of their review was to synthesize the major pavement energy harvesting approaches and compare their working principles, technical potential, and possible infrastructure applications. Their findings showed that pavement-based energy harvesting can support localized energy demands such as sensing, lighting, charging, monitoring, and smart road infrastructure. The review also emphasized that pavement energy systems are strongly affected by environmental conditions, material configuration, installation method, and energy-conversion efficiency. However, the reviewed literature mainly treated pavement energy as a harvested output or auxiliary power source, rather than as a constraint that directly governs the quality of a maintenance operation. The present study fills this operational gap by treating PV-battery energy as a direct control variable for repair heat flux, thermal conditioning duration, interface bonding, energy feasibility, and AI-based repair decision-making.

Tamagusko et al. [12] reviewed machine learning applications in road pavement management, with emphasis on pavement condition assessment, deterioration prediction, maintenance planning, and decision support. Their research problem was that road agencies increasingly require intelligent tools to process pavement data and support maintenance decisions, yet many ML applications remain fragmented, data-dependent, and weakly connected to pavement physics. The objective of their study was to analyze state-of-the-art ML techniques and identify challenges and future directions for pavement management systems. Their findings showed that machine learning can improve pavement condition prediction, refine data processing workflows, enhance deterioration modeling, and support maintenance decision-making. However, the reviewed studies generally relied on inspection data, condition indicators, imaging outputs, or network-level pavement management records. They were not directly coupled with FE/XFEM crack simulation, thermal conditioning behavior, cohesive repair interface response, or energy feasibility constraints. The present study addresses this gap by developing CERIG-Net as a physics-guided graph learning model trained on simulation-derived crack, thermal, interface, energy, durability, and repair strategy outputs rather than on pavement management indicators alone.

Latifi et al. [19] proposed a deep reinforcement learning framework for predictive maintenance planning of road assets while integrating lifecycle assessment and lifecycle cost analysis. Their research problem was how to determine maintenance and rehabilitation type and timing while balancing pavement condition, economic cost, and environmental impact. The objective of their work was to develop an intelligent long-term maintenance planning framework using reinforcement learning. Methodologically, they used long-term pavement performance data to develop a predictive deep neural network environment, then compared reinforcement learning policy models, including DQN and PPO. Their numerical findings showed that PPO was preferred because of better convergence and higher sample efficiency, and their case study generated a 20-year maintenance and rehabilitation plan for a six-lane 23 km highway in Texas while maintaining the road condition within an excellent range. Their study also considered International Roughness Index and rutting depth as pavement indicators, while excluding cracking metric due to insufficient data availability. These findings demonstrate the value of AI-based sequential decision-making for pavement maintenance planning. However, their framework operated at the road asset or network planning level, and did not simulate localized XFEM crack propagation, repair zone thermal conditioning, cohesive interface damage, or energy-limited repair execution. The present study advances this direction by shifting the decision problem from network-level maintenance scheduling to localized crack repair optimization based on coupled simulation outputs combining structural and thermal energy modeling.

Yao et al. [20] developed a deep reinforcement learning approach for long-term pavement maintenance planning. Their research problem was that pavement maintenance is a sequential decision-making process affected by deterioration, budget limitations, and long-term performance requirements, making conventional rule-based or short-term optimization methods insufficient for adaptive maintenance planning. The objective of their work was to develop a DRL-based maintenance decision model capable of learning long-term maintenance policies and improving cost-effectiveness. Their findings showed that the DRL model could learn improved maintenance strategies and keep pavement condition within an acceptable range while enhancing long-term maintenance cost-effectiveness. The study demonstrated that reinforcement learning can provide more adaptive planning decisions than conventional maintenance logic. However, their work focused on policy-level pavement maintenance and did not incorporate localized FE/XFEM crack evolution, energy-constrained repair heating, repair interface bonding, or simulation-generated multi-physics repair outputs. The present study addresses this gap by proposing a localized crack maintenance framework in which CERIG-Net ranks repair strategies using XFEM crack suppression, stress reduction, thermal adequacy, interface durability, energy feasibility, and service life gain.

Boonsiripant et al. [13] compared deep neural networks (DNNs) and graph convolutional networks (GCNs) for road surface condition prediction using the International Roughness Index (IRI). Their research addressed the need for pavement condition prediction models capable of incorporating spatial relationships among connected highway sections that are not explicitly represented by conventional independent feature learning approaches. The objective of their study was to determine whether graph-based representation of roadway sections could improve pavement-condition prediction relative to a conventional DNN while accounting for information on roadway condition and maintenance history. Methodologically, highway sections were represented as graph-connected spatial entities, and the GCN was evaluated against a DNN for IRI prediction. Their results demonstrated that graph convolution can capture relational information among pavement sections, although its advantage depends strongly on the connectivity and information structure of the road network. The study established the applicability of graph learning to pavement condition assessment, but its graph semantics remained centered on spatial relationships among highway sections and condition prediction. It did not represent localized XFEM crack evolution, energy-dependent thermal repair, cohesive interface degradation, or multi-strategy repair optimization. CERIG-Net differs by constructing a heterogeneous graph in which nodes represent interacting physical and operational components of an individual crack repair process rather than only spatially connected road sections.

Zhou and Al-Qadi [15] developed a graph neural network-based pavement simulator to accelerate prediction of three-dimensional flexible pavement structural responses obtained from finite-element analysis. Their research problem arose from the considerable computational cost associated with detailed three-dimensional FE pavement simulations, which can restrict repeated parametric evaluation and rapid structural assessment. The objective of their work was to develop a GNN surrogate capable of learning pavement response evolution while retaining the spatial connectivity of the original finite-element computational domain. Methodologically, three-dimensional FE pavement simulations were transformed into graphs in which computational nodes and their connectivity were represented explicitly, and message-passing operations were used to predict pavement structural responses under tire loading. Their findings demonstrated that the GNN could reproduce FE-generated response patterns with substantially lower computational demand after training, confirming the effectiveness of graph-based surrogate modeling for pavement mechanics. Nevertheless, the model was primarily designed for structural-response approximation. It did not represent XFEM crack propagation, energy-dependent repair heating, PV-battery availability, cohesive repair interface degradation, predictive uncertainty, or maintenance strategy ranking as interacting graph entities. CERIG-Net extends this direction by shifting graph learning from pavement-response approximation toward a coupled crack–energy–repair decision problem.

Lu et al. [14] developed a Spatial–Temporal Graph Attention Network (STGAT) for pavement condition prediction and preventive-maintenance assessment within digital twin-enabled highway management. Their research addressed the difficulty of predicting pavement deterioration when condition data are heterogeneous and exhibit both spatial dependence among roadway sections and temporal evolution across inspection periods. The objective was to construct a graph learning framework capable of exploiting spatial and temporal relationships while supporting the identification of pavement sections requiring preventive maintenance. Methodologically, heterogeneous pavement condition measurements were represented using a spatiotemporal graph architecture that combined graph attention with temporal learning. Their results demonstrated improved pavement condition prediction and showed that graph-derived outputs could support preventive maintenance assessment. Nevertheless, the graph representation primarily captured spatiotemporal relationships among roadway sections and evolving pavement condition indicators. It did not explicitly represent the mechanistic sequence connecting local crack geometry, fracture behavior, repair energy availability, thermal conditioning, interface bonding, post-repair structural recovery, and treatment feasibility. CERIG-Net addresses this distinction by representing these coupled physical and operational domains as heterogeneous node types within a localized pavement repair graph and by using their interactions to rank alternative maintenance actions.

Liu and Al-Qadi [16] advanced graph-based pavement modeling by proposing a physics-informed graph neural network for three-dimensional spatiotemporal structural response prediction of flexible pavements. Their research problem was that purely data-driven GNN surrogates may reproduce numerical training responses without explicitly enforcing the mechanics governing pavement deformation and stress transfer, potentially reducing physical consistency and robustness outside closely represented training states. Their objective was to incorporate mechanical knowledge directly into graph learning while maintaining the computational efficiency of a data-driven surrogate. The proposed framework transformed three-dimensional finite-element pavement responses into graph representations and incorporated physics-based constraints associated with displacement, strain, stress, and equilibrium into the learning process. Their results showed that incorporating physical constraints improved the robustness and consistency of graph-based pavement-response prediction compared with purely data-driven modeling. This work provides important evidence that pavement GNNs can benefit from explicit mechanics-based regularization; however, the framework remains primarily a structural response simulator in which graph topology originates from the pavement computational domain. It does not formulate a heterogeneous maintenance-interaction graph linking XFEM crack evolution, PV-battery energy constraints, thermal repair, cohesive interface damage, repair durability, service life gain, predictive uncertainty, and strategy ranking. CERIG-Net therefore extends physics-guided pavement graph learning from structural response prediction to multi-physics energy-constrained repair decision optimization.

Jiang et al. [21] investigated crack propagation mechanisms and intelligent fracture response prediction in asphalt pavements subjected to moving vehicle loads. Their study addressed the difficulty of evaluating crack evolution when the local crack tip response is simultaneously affected by traffic loading and pavement structural properties. Guided by fracture mechanics theory, the authors developed a three-dimensional asphalt pavement model in ABAQUS containing a longitudinal crack and evaluated the evolution of the Mode-I and Mode-II stress intensity factors, K_{I} and K_{II}, under variations in vehicle speed, load magnitude, layer thickness, and elastic modulus. Their results showed that lower vehicle speeds and increased tire contact pressure intensify the crack-driving response, while reductions in surface-layer thickness and increases in surface-layer elastic modulus significantly increase the stress intensity factors and consequently the susceptibility to crack propagation. In comparison, variations in the base and sub-base parameters produced relatively smaller effects on the crack tip response. The study further integrated the finite-element results with a backpropagation neural network for rapid prediction of K_{I} and K_{II}, achieving average prediction errors below 3%. These findings provide recent numerical evidence that pavement crack evolution is strongly governed by localized fracture mechanics, moving load conditions, and surface layer characteristics, and also demonstrate the value of intelligent prediction for efficient crack condition assessment. However, the study focused on pre-repair crack propagation and stress intensity prediction, and did not examine maintenance activation, energy-dependent thermal treatment, cohesive repair interface degradation, or optimization among alternative repair strategies. The present framework extends this fracture-oriented direction by coupling XFEM crack evolution with repair execution, thermal energy availability, interface behavior, and AI-assisted maintenance decision-making.

Collectively, the existing literature demonstrates substantial progress in finite-element crack modeling, renewable pavement energy systems, machine learning-based pavement management, reinforcement learning-based maintenance planning, and graph-based pavement prediction. However, these research directions remain largely separate. Existing pavement GNNs generally represent either spatial relationships among road sections, the temporal evolution of pavement conditions, or computational connectivity for structural response approximation. Even recent physics-informed GNN formulations primarily use mechanics-based constraints to improve pavement response prediction. A unified graph learning framework that explicitly represents XFEM crack evolution, material fracture behavior, repair energy availability, thermal conditioning, cohesive interface response, structural recovery, durability, service life extension, uncertainty, and candidate repair strategies as interacting heterogeneous entities remains insufficiently addressed. This gap motivates CERIG-Net, in which the novelty lies not merely in applying graph neural learning to pavement engineering but in constructing a physics-guided crack–energy–repair interaction graph that connects multi-physics response prediction directly with energy feasibility assessment and constrained maintenance strategy ranking.

3. Methodology

The proposed methodology is formulated as a finite element-driven simulation framework for investigating energy-constrained pavement crack maintenance operations under XFEM-based crack evolution and AI-based repair strategy optimization. The simulation model, implemented as Pavement_XFEM_EnergyRepair, represents a multilayer flexible pavement structure composed of five main layers: aged asphalt surface, binder asphalt layer, granular base layer, granular sub-base layer, and sub-grade. The overall computational sequence is organized into four principal simulation phases: pre-repair service loading, XFEM crack initiation and propagation, energy-limited thermal conditioning of the repair zone, and post-repair service loading. This sequence enables the framework to capture the mechanical condition of the cracked pavement before maintenance, the crack growth response during deterioration, the influence of energy-limited repair heating, and the structural performance of the repaired pavement after maintenance.

The finite-element environment is designed to represent the pavement maintenance problem as a coupled structural–thermal repair process rather than a conventional static pavement response model. As illustrated in Figure 1, the initial crack is embedded within a designated XFEM domain in the aged asphalt layer, while the surrounding repair zone is activated as the main treatment region. Localized mesh refinement is applied around both the crack zone and the repair zone to improve the numerical resolution of crack tip stress concentration, repair edge stress redistribution, and interface response. The pavement block is constrained using a fixed bottom boundary condition and side restraints, while the upper surface is subjected to a service load region representing traffic-induced wheel loading. In addition, the repair stage includes a thermal boundary condition defined through heat flux and convection/film conditioning, enabling the model to simulate temperature-assisted crack repair under realistic work-zone constraints.

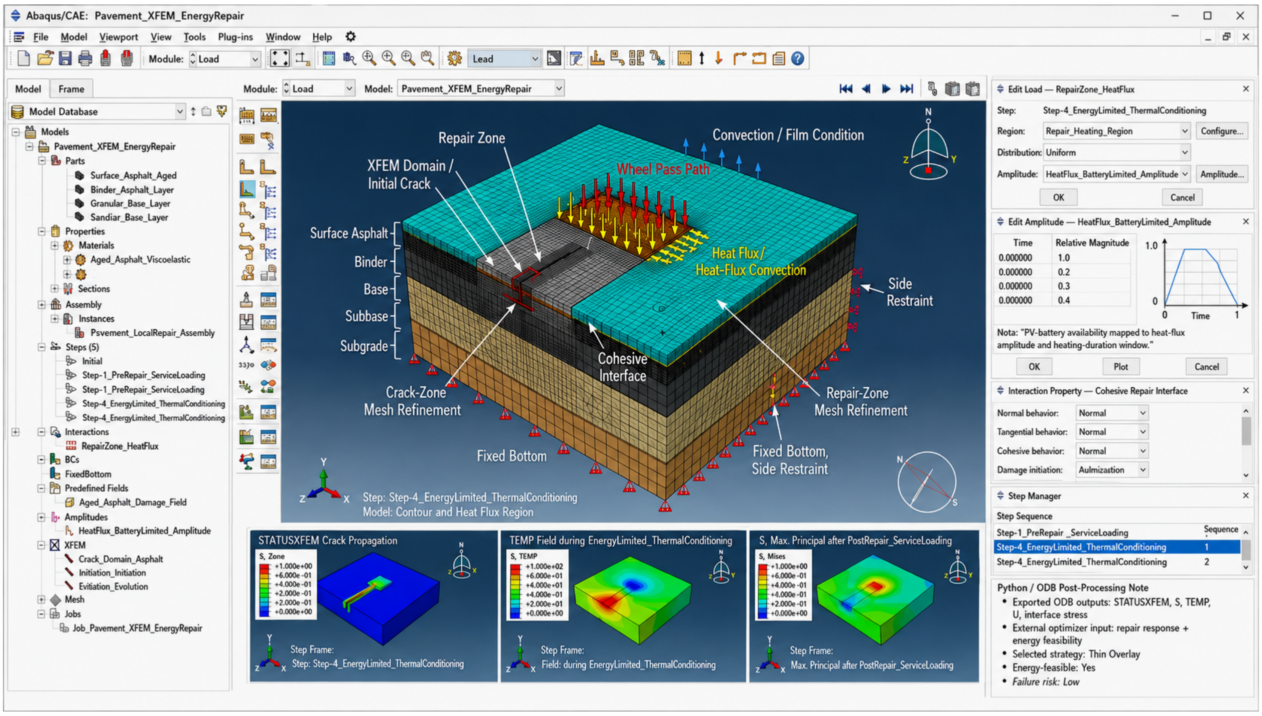

Figure 1. Abaqus-based simulation environment for energy-constrained pavement crack maintenance operations under XFEM-based crack evolution and AI-based repair strategy optimization.

The energy-limited repair operation is explicitly modeled in the simulation using Step 4: Energy Limited Thermal Conditioning and the Repair Zone Heat Flux load definition; see Figure 1. In this step, the repair heat input is not considered a free thermal source; rather, it is controlled by the Heat Flux Battery-Limited Amplitude function, which maps the available amount of PV-battery energy to the length of the repair heating duration and the history of the applied heat flux. The displayed amplitude profile is relative to the amplitude, and the data points are time-dependent and energy-limited rather than following a constant heating basis. The interaction panel also outlines the cohesive repair surface, normal behavior, tangential behavior, cohesive behavior, and damage initiation, which allow the model to determine whether the repaired section will be able to hold together after thermal conditioning and subsequent loading during service. In the illustrated simulation case, the postprocessing note details the choice of repair strategy, the energy feasibility state, and the predicted failure risk state, demonstrating how the simulation can contribute directly to maintenance strategy assessment.

The simulation results are then translated into a structured computational dataset which is used in the optimization stage of the AI-based repair strategy. As presented in the lower result preview panels in Figure 1, the extracted finite-element responses are STATUSXFEM crack propagation, the temperature field during energy-limited thermal conditioning, the maximum principal stress after post-repair service loading, and the repair interface stress response. The outputs are matched with the controlled input variables, including the crack geometry, size of the repair zone, properties of the pavement layers, amplitude of heat flux, duration of the heat conditioning, bonding quality, boundary conditions, and loading level. These form the basis under which the AI layer considers potential maintenance interventions such as patching, thin overlay, delayed repair, and deeper repair. In the proposed framework, the simulation is still the main scientific tool for modeling the pavement crack maintenance; the AI is employed as a second decision support tool to find the most effective repair strategy that can reduce crack propagation and stress concentration, meet the energy feasibility criteria, increase the durability of the repair, and maximize the service life gain of the pavement after crack maintenance.

3.1. Development of the Finite-Element Pavement Model

Our finite-element pavement model was developed to represent the structural response of a cracked flexible pavement section subjected to traffic loading and repair-related thermal conditioning. The model consists of a multilayer pavement system composed of an aged asphalt surface layer, binder asphalt layer, granular base, granular sub-base, and sub-grade foundation. Each layer was assigned mechanical and thermal properties suitable for pavement response simulation, including elastic modulus, Poisson's ratio, density, thermal conductivity, specific heat, and thermal expansion coefficient. The aged asphalt layer was treated as the critical damage-prone region because it contains the initial crack and the repair zone, while the lower granular and soil layers were included to reproduce realistic load transfer and support conditions. The lower boundary of the sub-grade was fixed in the vertical direction, and lateral restraints were applied to prevent unrealistic rigid-body movement while still allowing the pavement structure to deform under wheel loading. A surface contact load region was defined to represent the tire–pavement interaction, while thermal boundary conditions were introduced in the repair zone to simulate temperature-assisted maintenance operations.

Mesh refinement was applied around the crack region, repair interface, and wheel load contact area to capture high stress gradients, crack tip response, and post-repair stress redistribution with sufficient numerical accuracy. The pavement layers away from the damaged zone were meshed more coarsely to reduce computational cost while preserving the accuracy of the local fracture and repair response. The finite-element model provides the mechanical foundation for the later XFEM crack evolution simulation, since the stress, strain, displacement, and temperature fields generated in this stage control crack initiation, crack propagation, and repair zone performance. In this framework, the finite-element model is not used only to observe general pavement deformation; rather, it acts as the computational base for evaluating how crack geometry, layer stiffness, boundary conditions, wheel loading, repair zone configuration, and energy-limited thermal conditioning jointly influence pavement maintenance effectiveness and post-repair durability.

Table 1 summarizes the geometric, mechanical, and thermal input properties adopted for the multilayer flexible pavement model used in the finite-element simulation. The pavement structure was defined using six layers with a total modeled depth of 1670 mm, consisting of a 50 mm aged asphalt surface layer, 70 mm binder asphalt layer, 100 mm asphalt base layer, 200 mm granular base, 250 mm granular sub-base, and 1000 mm compacted sub-grade. The asphalt layers were assigned relatively high elastic stiffness values of 3500, 4200, and 4800 MPa for the aged surface, binder, and asphalt base layers, respectively, reflecting their dominant role in carrying wheel-induced tensile and compressive stresses. In contrast, the granular base, granular sub-base, and sub-grade were assigned lower stiffness values of 450, 220, and 80 MPa, respectively, allowing the model to reproduce realistic stress attenuation and vertical load transfer through the pavement foundation. Thermal parameters were also included because the proposed repair process involves energy-limited heat flux and thermal conditioning; therefore, thermal conductivity values ranged from 1.10 to 1.80 W/m·K, specific heat ranged from 760 to 920 J/kg·K, and thermal expansion coefficients ranged from 8.0×10^{-6} to 2.5×10^{-5} 1/K. The aged asphalt surface layer was assigned the highest thermal expansion coefficient of 2.5×10^{-5} 1/K and a specific heat of 920 J/kg·K, making it the most critical layer for evaluating thermally induced stress redistribution around the XFEM crack and repair zone during energy-constrained maintenance heating.

Table 1. Pavement layer geometry, material, and thermal properties used in the finite-element simulation.

Pavement Layer	Thickness (mm)	Elastic Modulus (MPa)	Poisson's Ratio	Density (kg/m^3)	Thermal Conductivity (W/m·K)	Specific Heat (J/kg·K)	Thermal Expansion Coefficient (1/K)
Aged asphalt surface layer	50	3500	0.35	2350	1.20	920	2.5×10^{-5}
Binder asphalt layer	70	4200	0.34	2380	1.15	900	2.3×10^{-5}
Asphalt base layer	100	4800	0.33	2400	1.10	880	2.1×10^{-5}
Granular base layer	200	450	0.38	2100	1.60	780	1.2×10^{-5}
Granular sub-base layer	250	220	0.40	2000	1.80	760	1.0×10^{-5}
Compacted sub-grade	1000	80	0.45	1850	1.35	850	8.0×10^{-6}

Table 2 defines the complete finite-element parameter set used to reproduce the pavement crack repair simulation and distinguishes the nominal values adopted in the reference case from the minimum–maximum ranges used to examine physically admissible variations. The model domain is represented by a 3000 mm by 2000 mm pavement block with a total depth of 1670 mm, discretized using C3D8R, C3D8T, and COH3D8 elements. A global mesh size of 25 mm is reduced to 6 mm at the crack tip, 8 mm along the cohesive interface, and 10 mm within the repair zone, yielding approximately 186,400 elements and 205,800 nodes. The fracture-related parameters were selected according to their specific roles in the XFEM damage formulation rather than being treated as interchangeable fitting coefficients. The nominal tensile strength of $\sigma_n^0 = 1.50$ MPa and shear strength of $\tau^0 = 1.08$ MPa define the local traction levels at which crack damage initiates; consequently, larger strength values delay crack initiation, whereas lower values activate damage at smaller stress levels. After initiation, the mode-I and mode-II critical fracture energies of $G_{\text{Ic}} = 500$ N/m and $G_{\text{IIc}} = 675$ N/m govern the energy required for progressive crack opening and sliding, respectively, thereby controlling the rate of post-initiation crack extension. The adopted nominal values were selected within the physically admissible ranges listed in Table 2 and were assessed against experimentally supported XFEM crack propagation behavior reported for asphalt materials [4,22–24]. The repair interface was calibrated separately from the bulk XFEM crack domain because it represents bonding and debonding between the existing pavement and repair material. The normal and shear interface stiffnesses of $K_n = 3.0 \times 10^6$ MPa/m and $K_s = 1.75 \times 10^6$ MPa/m control the initial elastic traction–separation response before damage, while the interface tensile and shear strengths define the onset of cohesive degradation. The interface fracture energy $G_{\text{int}} = 275$ N/m controls the energy dissipated during progressive debonding after damage initiation. Consequently, the interface damage variable D_{int} is interpreted as an evolving state variable ranging from 0 for an intact interface to 1 for complete separation rather than as an independently fitted material constant. Parameter selection was performed hierarchically by first constraining the fracture and interface quantities to the ranges listed in Table 2, then adopting nominal values that produced stable crack initiation and progressive damage without premature numerical failure, and finally checking that the resulting crack growth response remained consistent with the experimentally supported propagation trends used for external comparison. The repair zone is assigned a nominal modulus of 3750 MPa, while thermal conditioning is driven by a maximum heat flux of 13 kW/m^2 and scaled by a nominal energy amplitude of 0.70 over 15 min, targeting a repair temperature of 70 °C. Mechanical loading is imposed through a 675 kPa tire pressure, an 80 kN standard axle, and up to 10^5 loading cycles. The selected time increments, convergence tolerances, and element density limits further reduce numerical instability and ensure that the predicted responses remain insensitive to mesh refinement during repeated loading. Collectively, this parameter selection procedure provides a physically interpretable and numerically stable basis for evaluating crack initiation, fracture energy-controlled propagation, interface degradation, repair durability, and service life improvement [25].

Table 2. Finite-element discretization, fracture, interface, thermal, loading, and solver parameters adopted in the pavement crack repair model.

Parameter	Symbol	Nominal	Minimum	Maximum	Unit	FE Entity	Analysis Step	Limit/Criterion
Pavement geometry and finite-element discretization								
Model length	L	3000	2500	3500	mm	C3D8R	All steps	$L/W \geq 1.5$
Model width	W	2000	1600	2400	mm	C3D8R	All steps	$W \geq 8r_p$
Total model depth	H	1670	1500	1800	mm	C3D8R	All steps	$H \geq 10h_1$
Surface layer thickness	h_1	50	45	55	mm	C3D8R	All steps	$h_1 > d_0$
Binder layer thickness	h_2	70	60	80	mm	C3D8R	All steps	$h_2/h_1 = 1.20$–1.60
Asphalt base thickness	h_3	100	90	110	mm	C3D8R	All steps	$h_3 \geq 2h_1$
Granular base thickness	h_4	200	180	220	mm	C3D8R	All steps	$h_4 \geq 2h_3$
Granular sub-base thickness	h_5	250	225	275	mm	C3D8R	All steps	$h_5 > h_4$
Sub-grade thickness	h_6	1000	900	1100	mm	C3D8R	All steps	$h_6/H \geq 0.55$
Global mesh size	h_g	25	20	35	mm	C3D8R	All steps	$\Delta\sigma_{\max} < 3\%$
Crack tip mesh size	h_{tip}	6	5	8	mm	XFEM	Crack growth	$h_{\text{tip}}/a_0 \leq 0.20$
Interface mesh size	h_{int}	8	6	12	mm	COH3D8	Repair stage	$h_{\text{int}} \leq t_r/4$
Repair zone mesh size	h_r	10	8	15	mm	C3D8T	Thermal repair	$h_r \leq t_r/3$
Total element count	N_e	186,400	145,000	235,000	elements	Mixed mesh	All steps	$\Delta R_d < 2\%$
Total node count	N_n	205,800	160,000	260,000	nodes	Mixed mesh	All steps	$N_n/N_e = 1.05$–1.20
XFEM crack geometry and fracture parameters								
Initial crack length	a_0	55	35	75	mm	XFEM	Pre-repair	$a_0/L \leq 0.03$
Initial crack depth	d_0	30	15	45	mm	XFEM	Pre-repair	$d_0 < h_1$
Crack inclination	θ_c	12.5	0	25	degree	XFEM	Pre-repair	$0° \leq \theta_c \leq 25°$
XFEM domain width	W_{XFEM}	250	220	300	mm	Enrichment	Crack growth	$W_{\text{XFEM}} \geq 4a_0$
XFEM domain length	L_{XFEM}	450	400	500	mm	Enrichment	Crack growth	$L_{\text{XFEM}} > a_0 + \Delta a$
Normal tensile strength	σ_n^0	1.50	1.20	1.80	MPa	XFEM	Crack growth	$\sigma_n/\sigma_n^0 \geq 1$
Shear strength	τ_0	1.08	0.85	1.30	MPa	XFEM	Crack growth	$\tau/\tau_0 \geq 1$
Mode-I fracture energy	$G_{\text{I}c}$	500	350	650	N/m	XFEM	Crack growth	$G_{\text{I}} \geq G_{\text{I}c}$
Mode-II fracture energy	$G_{\text{II}c}$	675	500	850	N/m	XFEM	Crack growth	$G_{\text{II}} \geq G_{\text{II}c}$
Mixed-mode exponent	η	1.75	1.50	2.00	-	XFEM	Crack growth	$(G_I/G_{Ic})^\eta + (G_{II}/G_{IIc})^\eta \geq 1$
Crack damage variable	D_c	0.50	0	1	-	XFEM	Crack growth	$D_c = 1$ at full separation
Critical crack increment	Δa_c	2.0	1.0	3.0	mm	XFEM	Crack growth	$\Delta a \geq \Delta a_c$

https://doi.org/10.3390/math14173149

Table 2. *Cont.*

Parameter	Symbol	Nominal	Minimum	Maximum	Unit	FE Entity	Analysis Step	Limit/Criterion
Repair zone and cohesive interface parameters								
Repair zone length	L_r	450	300	600	mm	C3D8T	Repair stage	$L_r \geq 5a_0$
Repair zone width	W_r	265	180	350	mm	C3D8T	Repair stage	$W_r \geq W_{\mathrm{XFEM}}$
Repair thickness	t_r	50	30	70	mm	C3D8T	Repair stage	$t_r/h_1 = 0.60$–1.40
Repair modulus	E_r	3750	2500	5000	MPa	C3D8R	Post-repair	$0.70 \leq E_r/E_1 \leq 1.40$
Repair Poisson ratio	ν_r	0.355	0.33	0.38	-	C3D8R	Post-repair	$0 < \nu_r < 0.50$
Repair density	ρ_r	2325	2250	2400	kg/m^3	C3D8T	All repair steps	$\lvert\rho_r - \rho_1\rvert/\rho_1 < 0.10$
Repair conductivity	k_r	1.25	1.00	1.50	W/mK	C3D8T	Thermal repair	$k_r > 0$
Repair specific heat	c_r	900	820	980	J/kgK	C3D8T	Thermal repair	$c_r > 0$
Normal interface stiffness	K_n	3.0×10^6	1.0×10^6	5.0×10^6	MPa/m	COH3D8	Repair stage	$K_n > K_s$
Shear interface stiffness	K_s	1.75×10^6	0.5×10^6	3.0×10^6	MPa/m	COH3D8	Repair stage	$K_s/K_n = 0.30$–0.70
Interface tensile strength	t_n^0	0.90	0.60	1.20	MPa	COH3D8	Post-repair	$t_n/t_n^0 \geq 1$
Interface shear strength	t_s^0	0.675	0.45	0.90	MPa	COH3D8	Post-repair	$t_s/t_s^0 \geq 1$
Interface fracture energy	G_{int}	275	150	400	N/m	COH3D8	Post-repair	$G \geq G_{\mathrm{int}}$
Bonding quality factor	B_q	0.70	0.40	1.00	-	Interface scalar	Repair stage	$B_q \geq 0.60$
Interface damage variable	D_{int}	0.35	0	1	-	COH3D8	Post-repair	$D_{\mathrm{int}} < 0.50$
Thermal repair and PV-battery energy parameters								
Maximum heat flux	q_{max}	13	8	18	kW/m^2	Surface flux	Thermal repair	$q_{\mathrm{max}} \leq 18$
Energy amplitude	$A_E(t)$	0.70	0.20	1.00	-	Amplitude	Thermal repair	$0 \leq A_E(t) \leq 1$
Applied heat flux	q_{repair}	9.10	1.60	18.00	kW/m^2	Surface flux	Thermal repair	$q_{\mathrm{repair}} = A_E q_{\mathrm{max}}$
Heating duration	t_h	15	5	25	min	Transient step	Thermal repair	$t_h \leq 25$
Initial temperature	T_0	27.5	20	35	°C	Temperature field	Initial step	$T_0 < T_{\mathrm{tar}}$
Target temperature	T_{tar}	70	55	85	°C	Temperature output	Thermal repair	$T_r \geq 55$°C
Peak repair temperature	T_{peak}	74	55	85	°C	Temperature output	Thermal repair	$55 \leq T_{\mathrm{peak}} \leq 85$
Convection coefficient	h_c	11.5	8	15	W/m^{2}K	Film condition	Thermal repair	$h_c > 0$
Ambient temperature	T_∞	32.5	25	40	°C	Film condition	Thermal repair	$T_\infty < T_{\mathrm{peak}}$
PV power	P_{PV}	6.0	3.0	10.0	kW	Energy input	Thermal repair	$P_{\mathrm{PV}} > 0$
Battery capacity	E_{bat}	12	6	20	kWh	Energy storage	Thermal repair	$E_{\mathrm{bat}} \geq E_{\mathrm{req}}$
Initial state of charge	SOC_0	0.80	0.30	1.00	-	Battery state	Initial step	$\mathrm{SOC}_0 \geq 0.30$
Minimum state of charge	$\mathrm{SOC}_{\mathrm{min}}$	0.20	0.15	0.30	-	Battery limit	Thermal repair	$\mathrm{SOC} \geq \mathrm{SOC}_{\mathrm{min}}$
Required repair energy	E_{req}	8.2	4.0	15.0	kWh	Energy demand	Thermal repair	$E_{\mathrm{avail}} \geq E_{\mathrm{req}}$
Available repair energy	E_{avail}	9.6	3.0	20.0	kWh	Energy supply	Thermal repair	$E_{\mathrm{avail}} = \mathrm{SOC}_0 E_{\mathrm{bat}}$
Energy feasibility index	F_E	1	0	1	-	Binary state	Thermal repair	$F_E = \mathbb{I}(E_{\mathrm{avail}} \geq E_{\mathrm{req}})$

Table 2. *Cont.*

Parameter	Symbol	Nominal	Minimum	Maximum	Unit	FE Entity	Analysis Step	Limit/Criterion
Traffic loading, solver controls, and response limits								
Tire contact pressure	p	675	550	800	kPa	Surface pressure	Pre/Post-repair	$p \leq 800$
Contact patch radius	r_p	110	90	130	mm	Contact area	Pre/Post repair	$A_p = \pi r_p^2$
Standard axle load	P_{std}	80	70	90	kN	Surface pressure	Pre/Post-repair	$P_{\text{std}} = 80 \pm 10$
Heavy axle load	P_{heavy}	110	100	120	kN	Surface pressure	Sensitivity step	$P_{\text{heavy}} > P_{\text{std}}$
Loading cycles	N	4.0×10^4	1.0×10^3	1.0×10^5	cycles	Cyclic history	Pre/Post-repair	$N \leq 10^5$
Initial time increment	Δt_0	1.0×10^{-3}	1.0×10^{-5}	1.0×10^{-2}	s	Solver control	All steps	$\Delta t_0 < \Delta t_{\text{max}}$
Maximum time increment	Δt_{max}	0.10	0.05	0.20	s	Solver control	All steps	$\Delta t_{\text{max}} \leq 0.20$
Maximum equilibrium iterations	N_{iter}	25	15	40	iterations	Newton–Raphson	All steps	$N_{\text{iter}} \leq 40$
Force residual tolerance	ε_F	5.0×10^{-3}	1.0×10^{-3}	1.0×10^{-2}	-	Convergence control	All steps	$\varepsilon_F \leq 10^{-2}$
Displacement tolerance	ε_u	1.0×10^{-3}	1.0×10^{-4}	5.0×10^{-3}	-	Convergence control	All steps	$\varepsilon_u \leq 5 \times 10^{-3}$
Maximum principal stress	σ_{max}	2.22	1.80	3.85	MPa	Field output	Post-repair	$\sigma_{\text{max}} < \sigma_{\text{max,pre}}$
Final crack length	a_f	53.8	50.0	94.7	mm	XFEM output	Post-repair	$a_f < a_{\text{no-repair}}$
Crack growth reduction	$R_{\Delta a}$	43.2	0	60	%	Derived output	Post-repair	$R_{\Delta a} > 0$
Stress reduction	R_σ	42.3	0	60	%	Derived output	Post-repair	$R_\sigma > 0$
Durability index	R_d	0.86	0.40	1.00	-	Derived output	Post-repair	$R_d \geq 0.80$
Service life gain	ΔN_f	6.7	0	10	year	Derived output	Post-repair	$\Delta N_f > 0$

3.2. XFEM-Based Crack Evolution and Maintenance Repair Simulation

The crack evolution stage was formulated using the extended finite-element method (XFEM) to simulate crack initiation, crack propagation, and post-repair crack response within the aged asphalt surface layer without requiring continuous remeshing of the crack path. In the proposed simulation, the initial crack was embedded inside the XFEM-enriched region of the aged asphalt layer, while the surrounding repair zone was activated later to represent crack sealing, localized patching, or thin overlay maintenance. The XFEM displacement field was expressed by enriching the conventional finite-element approximation with discontinuous and crack tip functions, as follows [26]:

$$\mathbf{u}^h(\mathbf{x}) = \sum_{i\in I} N_i(\mathbf{x})\mathbf{u}_i + \sum_{j\in J} N_j(\mathbf{x})H(\mathbf{x})\mathbf{a}_j + \sum_{k\in K} N_k(\mathbf{x}) \sum_{\alpha=1}^{4} F_\alpha(\mathbf{x})\mathbf{b}_k^\alpha \tag{1}$$

where $N_i(\mathbf{x})$ is the standard shape function, $\mathbf{u}_i$ is the conventional nodal displacement vector, $H(\mathbf{x})$ is the Heaviside enrichment function used to represent displacement discontinuity across the crack surface, $F_\alpha(\mathbf{x})$ denotes the crack tip asymptotic enrichment functions, and $\mathbf{a}_j$ and $\mathbf{b}_k^\alpha$ are the additional enriched degrees of freedom. This formulation allowed the crack to propagate through the asphalt layer according to the local stress and fracture response rather than being restricted to predefined element boundaries, which is essential for representing realistic pavement crack growth under repeated wheel loading and thermal repair conditions.

The XFEM enrichment was embedded within the governing thermomechanical balance equations of the pavement domain. Because the wheel loading and repair stages were treated as quasi-static mechanical processes, the local mechanical equilibrium equation was written as

$$\nabla \cdot \boldsymbol{\sigma} + \mathbf{b} = \mathbf{0} \qquad \text{in } \Omega, \tag{2}$$

where $\boldsymbol{\sigma}$ is the Cauchy stress tensor, $\mathbf{b}$ is the body force vector, and Ω denotes the pavement domain. The thermomechanical constitutive response was expressed through decomposition of the total strain into mechanical and thermal components

$$\boldsymbol{\varepsilon} = \boldsymbol{\varepsilon}^e + \boldsymbol{\varepsilon}^{th}, \qquad \boldsymbol{\varepsilon}^{th} = \alpha_T(T - T_{\text{ref}})\mathbf{I}, \tag{3}$$

$$\boldsymbol{\sigma} = \mathbf{C} : \left(\boldsymbol{\varepsilon} - \boldsymbol{\varepsilon}^{th}\right), \tag{4}$$

where $\mathbf{C}$ is the material constitutive tensor, α_T is the coefficient of thermal expansion, T is the current temperature, T_{ref} is the reference temperature, and $\mathbf{I}$ is the second-order identity tensor. This formulation allows the temperature field generated during thermal conditioning to contribute directly to pavement deformation and stress redistribution.

The transient temperature field during repair conditioning was governed by conservation of thermal energy:

$$\rho c_p \frac{\partial T}{\partial t} = \nabla \cdot (k\nabla T) + Q \qquad \text{in } \Omega_T \tag{5}$$

where ρ is the material density, c_p is the specific heat capacity, k is the thermal conductivity, Q represents an internal volumetric heat source when present, and Ω_T denotes the thermal analysis domain. In the present repair formulation, the energy supplied by the PV battery system was imposed primarily as a surface heat flux boundary condition over the repair region Γ_r rather than as an internal volumetric source:

$$-k\nabla T \cdot \mathbf{n} = q_{\text{repair}}(t) = A_E(t)q_{\max} \qquad \text{on } \Gamma_r \tag{6}$$

where **n** is the outward unit normal vector, $q_{\max}$ is the maximum allowable repair heat flux, and $A_E(t)$ is the normalized PV battery-dependent energy availability amplitude. Thus, the available electrical energy state enters the thermomechanical problem through the thermal boundary condition rather than through an artificial modification of the pavement material properties. When $A_E(t) = 1$, the repair system can sustain the prescribed maximum heat flux, whereas $A_E(t) < 1$ represents an energy-limited condition in which the thermal boundary input is reduced. The resulting temperature field is subsequently transferred to the mechanical problem through the thermal strain term in Equation (3).

Crack initiation was governed by a traction-based damage criterion applied within the XFEM crack domain. The initiation condition was evaluated using the normalized stress ratio between the local crack plane stresses and their corresponding critical strengths. Damage was assumed to initiate when the maximum nominal stress criterion reached unity [27]:

$$f_{\text{init}} = \max\left[\frac{\langle \sigma_n \rangle}{\sigma_n^0}, \frac{|\tau_s|}{\tau_s^0}, \frac{|\tau_t|}{\tau_t^0}\right] \geq 1 \tag{7}$$

where σ_n is the normal traction stress, τ_s and τ_t are the two shear traction components, σ_n^0 is the critical normal tensile strength, and τ_s^0 and τ_t^0 are the corresponding critical shear strengths. Physically, these strength parameters determine the stress level required to activate local fracture: σ_n^0 controls tensile crack opening, whereas τ_s^0 and τ_t^0 control shear-driven damage initiation. The nominal values adopted in the reference simulation, including $\sigma_n^0 = 1.50$ MPa and a nominal shear strength of 1.08 MPa, were selected within the physically admissible ranges reported in Table 2. These quantities are treated as crack initiation parameters rather than crack growth parameters; increasing their values delays the onset of damage, whereas decreasing them causes earlier initiation under the same loading state. The Macaulay bracket $\langle \cdot \rangle$ ensures that only tensile normal traction contributes to crack opening, preventing compressive stresses from producing nonphysical tensile fracture initiation.

$$G_{\text{mix}} = G_I + G_{II} + G_{III}, \tag{8}$$

$$G_{\text{mix}} \geq G_c, \tag{9}$$

where G_I, G_{II}, and G_{III} denote the mode-I oAfter damage initiation, crack extension was governed independently by an energy-based evolution criterion. This distinction is important because the strength parameters determine when fracture begins, whereas the critical fracture energies determine the amount of energy that must be dissipated for the crack to continue propagating. The mixed-mode energy release was expressed as

The progressive crack damage variable D_c was defined over $0 \leq D_c \leq 1$, where $D_c = 0$ represents an undamaged enriched crack surface and $D_c = 1$ denotes complete local separation. Unlike tensile strength or fracture energy, D_c is not an independently prescribed fracture property constant; rather, it is an internal state variable that evolves as damage accumulates according to the selected traction–separation and fracture energy laws. The degradation of effective traction across the damaged crack surface was expressed as [28]:

$$\mathbf{T} = (1 - D_c)\mathbf{T}_0 \tag{10}$$

where $\mathbf{T}_0$ is the undamaged traction vector and $\mathbf{T}$ is the effective traction after damage evolution. As D_c increases, the load-carrying capacity of the cracked material progressively decreases, allowing the model to represent the transition from crack initiation to stable extension and ultimately to severe local separation. This formulation separates three physically distinct stages: stress-controlled damage initiation, crack propagation controlled by fracture energy, and damage-dependent degradation of the local traction transfer capacity.

Progressive degradation of the crack and repair interfaces was represented by a scalar damage variable governed by the maximum effective separation attained during loading. The effective separation was defined as

$$\delta_m = \sqrt{\langle \delta_n \rangle^2 + \delta_s^2 + \delta_t^2}, \tag{11}$$

where δ_n, δ_s, and δ_t are the normal and two tangential separation components, respectively, and the Macaulay bracket prevents compressive normal separation from contributing to tensile damage. For the adopted bilinear traction–separation representation, the scalar damage variable was evaluated as

$$D = \begin{cases} 0, & \delta_m^{\max} \leq \delta_0, \\ \dfrac{\delta_f(\delta_m^{\max} - \delta_0)}{\delta_m^{\max}\left(\delta_f - \delta_0\right)}, & \delta_0 < \delta_m^{\max} < \delta_f, \\ 1, & \delta_m^{\max} \geq \delta_f, \end{cases} \tag{12}$$

where $\delta_m^{\max}$ is the maximum effective separation reached during the loading history, δ_0 is the effective separation at damage initiation, and δ_f is the separation corresponding to complete loss of cohesive load transfer capacity. Damage evolution is irreversible, such that

$$\dot{D} \geq 0, \qquad 0 \leq D \leq 1. \tag{13}$$

For a linear softening law, the complete-separation displacement is related to the critical fracture energy through the area under the traction–separation curve. In an equivalent single-mode representation,

$$G_c = \int_0^{\delta_f} t(\delta)\, d\delta = \frac{1}{2} t_0 \delta_f, \qquad \delta_f = \frac{2G_c}{t_0}, \tag{14}$$

where t_0 is the effective cohesive strength at damage initiation. Under mixed-mode loading, the critical energy was evaluated using the adopted power-law interaction between the fracture energy components:

$$\left(\frac{G_{\mathrm{I}}}{G_{\mathrm{Ic}}}\right)^{\eta} + \left(\frac{G_{\mathrm{II}}}{G_{\mathrm{IIc}}}\right)^{\eta} + \left(\frac{G_{\mathrm{III}}}{G_{\mathrm{IIIc}}}\right)^{\eta} = 1 \tag{15}$$

where G_{Ic}, G_{IIc}, and G_{IIIc} are the critical fracture energies and η is the mixed-mode interaction exponent. The same mathematical damage structure was used for the repair interface, with D_{int} representing interface degradation and the corresponding interface strengths, stiffnesses, and fracture energy G_{int} defining damage initiation and complete separation. Consequently, $D_{\mathrm{int}} = 0$ denotes an intact repair bond, intermediate values represent progressive stiffness and traction degradation, and $D_{\mathrm{int}} = 1$ represents complete local debonding.

The maintenance repair simulation was subsequently introduced by activating a localized repair zone surrounding the propagated crack and assigning a separate cohesive response to the interface between the existing pavement and the repair material. The interface formulation was intentionally distinguished from the XFEM fracture law because it describes bonding and debonding of two adjoining material regions rather than crack propagation through the bulk asphalt. The nominal cohesive traction vector was defined as [29]:

$$\mathbf{t} = \begin{bmatrix} t_n \\ t_s \\ t_t \end{bmatrix} = \begin{bmatrix} K_n & 0 & 0 \\ 0 & K_s & 0 \\ 0 & 0 & K_t \end{bmatrix} \begin{bmatrix} \delta_n \\ \delta_s \\ \delta_t \end{bmatrix}, \tag{16}$$

where t_n, t_s, and t_t are the normal and shear cohesive tractions; K_n, K_s, and K_t are the corresponding interface stiffnesses; and δ_n, δ_s, and δ_t are the normal and shear separations across the repair interface. The interface stiffnesses control the initial slope of the traction–separation response before damage occurs, and as such represent the ability of the bonded repair interface to transfer normal and shear stresses. The nominal values $K_n = 3.0 \times 10^6$ MPa/m and $K_s = 1.75 \times 10^6$ MPa/m were selected within the admissible ranges reported in Table 2 with $K_n > K_s$ in order to represent the different normal and tangential constraint characteristics of the bonded interface.

Damage initiation at the repair interface is controlled by the corresponding cohesive tensile and shear strengths, while the interface fracture energy $G_{\text{int}} = 275$ N/m governs the energy dissipated during progressive debonding after initiation. The interface damage variable D_{int} similarly evolves between 0 and 1, with $D_{\text{int}} = 0$ representing an intact bond and $D_{\text{int}} = 1$ representing complete local separation. Thus, K_n and K_s determine the pre-damage interface stiffness, the cohesive strengths determine the onset of debonding, and G_{int} controls its subsequent evolution. During the energy-constrained thermal conditioning stage, the applied heat flux modifies the repair zone temperature and bonding condition, thereby influencing the interface response and the subsequent evolution of D_{int} under post-repair traffic loading. This formulation enables the model to distinguish between bulk asphalt fracture governed by XFEM and repair interface degradation governed by the cohesive traction–separation law. During the energy-constrained thermal conditioning stage, the repair heat flux was applied to the localized repair zone as a time-dependent boundary input governed by the electrical energy that could be supplied by the combined PV-battery system. Physically, $q_{\max}$ represents the maximum thermal flux that the repair equipment is allowed to deliver to the pavement surface, whereas the actual heat flux may be lower when the instantaneous electrical power or stored battery energy is insufficient to sustain this maximum demand. The available electrical power at time t is represented by the combined contribution of the photovoltaic source and the allowable battery discharge:

$$P_{\text{avail}}(t) = P_{\text{PV}}(t) + P_{\text{bat}}(t) \tag{17}$$

where $P_{\text{PV}}(t)$ denotes the instantaneous photovoltaic contribution and $P_{\text{bat}}(t)$ is the battery power that can be supplied without reducing the state of charge below the prescribed minimum value $SOC_{\min}$. The corresponding normalized energy availability amplitude is defined as

$$A_E(t) = \min\left[1, \frac{\eta_h P_{\text{avail}}(t)}{q_{\max} A_r}\right], \qquad 0 \le A_E(t) \le 1, \tag{18}$$

where η_h is the effective electrical-to-thermal conversion efficiency and A_r is the heated repair area. The denominator $q_{\max} A_r$ represents the thermal power associated with operating the repair system at its maximum prescribed heat flux. When the available PV-battery power is sufficient to satisfy this demand, $A_E(t) = 1$ and the full heat flux can be maintained; when the available power is lower, $A_E(t) < 1$, and the applied thermal flux is reduced proportionally rather than assuming an unrealistically constant heat source. Accordingly, the actual heat flux supplied to the pavement is expressed as

$$q_{\text{repair}}(t) = A_E(t) q_{\max}. \tag{19}$$

The instantaneous power constraint is supplemented by a cumulative energy balance condition over the repair heating interval. The thermal energy delivered to the repair area must satisfy

$$E_{\text{repair}} = \frac{A_r}{\eta_h} \int_0^{t_H} q_{\text{repair}}(t)\, dt \le E_{\text{avail}}, \tag{20}$$

where t_H is the thermal conditioning duration and E_{avail} is the usable PV battery energy available during the repair operation. In the battery representation, the usable stored energy contribution is constrained by the initial and minimum states of charge, while photovoltaic generation contributes additional energy during the heating interval. The energy feasibility indicator is evaluated according to whether the available energy is sufficient to satisfy the required repair energy demand. This formulation assumes that the electrical-to-thermal conversion efficiency is represented by an effective constant η_h over each repair scenario, that PV and battery power are quasi-steady within each numerical thermal increment, and that the heating equipment cannot exceed $q_{\max}$. These assumptions provide a physically interpretable connection between PV battery availability and pavement thermal conditioning while avoiding the unrealistic assumption of unlimited constant heating. Consequently, low-energy states produce smaller $A_E(t)$ values, lower repair zone temperatures, and weaker interface bonding, whereas sufficiently supplied PV battery states allow $A_E(t)$ to approach unity and sustain the thermal conditions required for stronger repair interface recovery. The repair performance index was formulated as follows:

$$R_{\text{perf}} = w_1\left(1 - \frac{\Delta a_{\text{post}}}{\Delta a_{\text{pre}}}\right) + w_2\left(1 - \frac{\sigma_{\max,\text{post}}}{\sigma_{\max,\text{pre}}}\right) + w_3(1 - D_{\text{int}}) + w_4 F_E \tag{21}$$

where Δa_{pre} and Δa_{post} are the crack growth lengths before and after repair, $\sigma_{\max,\text{pre}}$ and $\sigma_{\max,\text{post}}$ are the corresponding maximum principal stresses, D_{int} is the repair interface damage variable, and F_E is the energy feasibility indicator. The weighting coefficients were fixed before repair strategy evaluation as

$$w_1 = 0.40, \qquad w_2 = 0.25, \qquad w_3 = 0.20, \qquad w_4 = 0.15, \qquad \sum_{i=1}^{4} w_i = 1.$$

The coefficients provide a normalized representation of the four physical components of repair effectiveness based on engineering priority, rather than being fitted to the final strategy-ranking results. The largest coefficient, $w_1 = 0.40$, is assigned to crack growth suppression, which is because limiting continued fracture propagation represents the principal structural objective of the maintenance operation. The coefficient $w_2 = 0.25$ represents the importance of reducing maximum principal stress, which controls the post-repair crack driving force and the tendency for subsequent damage accumulation. The interface integrity term is weighted by $w_3 = 0.20$ because progressive interface degradation directly affects load transfer, bonding quality, and long-term repair durability. Finally, $w_4 = 0.15$ represents operational energy feasibility. Its comparatively smaller weight avoids allowing the binary feasibility state to dominate the continuous structural and interface response measures while still penalizing repair conditions that cannot be adequately supported by the available PV battery energy. The weights are dimensionless, non-negative, and sum to unity, ensuring that R_{perf} remains a normalized composite measure with an interpretable contribution from each repair performance component. The same fixed coefficient set was applied to all simulated repair scenarios and candidate maintenance strategies, thereby preventing scenario-specific tuning and ensuring reproducibility of the performance index calculation.

Figure 2 presents the XFEM crack evolution and repair zone activation mechanism as a coupled computational blueprint in which the pavement structure, fracture process, energy-constrained repair action, and output extraction are integrated within a single simulation logic. The central finite-element model represents the multilayer pavement system, including the aged asphalt surface, binder asphalt layer, granular base, granular sub-base, and sub-grade, while the boundary constraints and wheel load contact patch define the structural loading environment that drives crack initiation and propagation. The XFEM damage layer shows how the initial crack evolves through crack tip stress concentration, damage progression, and post-repair crack response without requiring continuous remeshing, enabling the simulation to capture realistic crack path development within the aged asphalt layer. The localized repair zone is activated around the XFEM crack region, where thermal conditioning and repair interface bonding are controlled by an energy-constrained repair layer through battery-limited heat flux and energy feasibility conditions. This integration is important because it links the mechanical effectiveness of pavement maintenance to the actual energy availability of the repair operation rather than assuming ideal repair conditions. The output extraction layer converts the simulated response into measurable indicators, including STATUSXFEM, maximum principal stress, temperature field, interface stress, crack growth length, and service life gain, which together provide a quantitative basis for evaluating the repair durability and selecting the optimal maintenance decision. Overall, the figure demonstrates that the proposed framework does not treat crack repair as a single isolated intervention; instead, it models pavement maintenance as a closed-loop process in which structural damage evolution, energy-limited repair execution, post-repair performance, and feedback for the next repair cycle are continuously connected Table 3.

The crack growth and XFEM damage index response demonstrates the structural benefit of activating the pavement maintenance intervention shown in Figure 3 at $N = 40{,}000$ loading cycles. Before repair, the crack length increases nonlinearly from approximately 35 mm at the initial loading stage to about 48.0 mm at the intervention point, indicating progressive crack propagation under repeated wheel loading. At the same time, the XFEM damage index rises steadily, confirming that the crack growth process is accompanied by continuous stiffness degradation and damage accumulation in the aged asphalt layer. After the energy-constrained maintenance action is applied, the effective crack length is reduced from 48.0 mm to 35.9 mm, showing the immediate structural recovery produced by the localized repair strategy. More importantly, the post-maintenance crack growth curve remains consistently below the unrepaired response, reaching nearly 54 mm at 100,000 cycles compared with approximately 95 mm in the pre-maintenance/no-repair trajectory. This corresponds to an estimated final crack-growth reduction of about 43.3%, while the XFEM damage index is reduced by approximately 45.8%. The repaired pavement also remains below the critical crack threshold of 75 mm for a substantially longer period, producing a service life delay of about 20.8% of the simulated loading cycle range. These results indicate that the proposed maintenance strategy does not unrealistically eliminate crack evolution; rather, it suppresses the crack driving response, delays damage accumulation, and improves post-repair durability under repeated loading, which supports its suitability as a repair strategy within the energy-constrained pavement maintenance simulation framework.

Table 3. XFEM crack, repair interface, and maintenance operation parameters adopted in the pavement crack maintenance simulation.

Parameter Group	Parameter	Adopted Value/Range	Unit	Role in the Simulation
XFEM crack geometry	Initial crack length, a_0	35–75	mm	Defines the initial surface crack severity before maintenance and controls the starting crack driving force.
	Initial crack depth, d_0	15–45	mm	Represents partial-depth cracking within the aged asphalt layer and determines the crack penetration level.
	Crack inclination angle, θ_c	0–25	degree	Captures non-vertical crack orientation caused by combined traffic loading and thermal stress.
	XFEM enriched domain width	250	mm	Defines the local domain in which discontinuous crack enrichment is activated around the damaged zone.
	XFEM enriched domain length	450	mm	Provides sufficient propagation space for crack extension before and after repair activation.
	Refined crack tip mesh size	5–8	mm	Improves numerical resolution around crack tip stress concentration and damage evolution.
Crack initiation and propagation	Critical normal tensile strength, σ_n^0	1.20–1.80	MPa	Controls mode-I crack opening initiation in the aged asphalt material.
	Critical shear strength, $\tau_s^0 = \tau_t^0$	0.85–1.30	MPa	Controls sliding and tearing resistance under mixed-mode crack propagation.
	Mode-I fracture energy, G_I	350–650	N/m	Defines the energy required for crack opening propagation in asphalt.
	Mode-II fracture energy, G_{II}	500–850	N/m	Defines the resistance against shear-driven crack growth under wheel loading.
	Mixed-mode fracture criterion	Power-law interaction	-	Allows crack evolution to depend on combined opening and shear fracture modes.
	Damage initiation criterion	Maximum nominal stress	-	Activates crack damage when normalized tensile or shear stress reaches unity.
	Damage variable range, D_c	0–1	-	Represents the transition from undamaged crack interface to complete crack separation.
Repair-zone configuration	Repair strategy cases	Delay repair; crack sealing; localized patch; thin overlay; deep repair	-	Defines the candidate maintenance strategies evaluated by the simulation and AI optimization stage.
	Localized repair zone length	300–600	mm	Controls the treated area surrounding the crack and affects stress redistribution after repair.
	Localized repair zone width	180–350	mm	Represents the lateral extent of maintenance intervention around the crack path.
	Repair zone thickness	30–70	mm	Controls the mechanical contribution of the repaired material to surface layer recovery.
	Thin overlay thickness	40–60	mm	Represents the selected overlay-type maintenance strategy under energy-feasible repair conditions.
	Repair material modulus, E_r	2500–5000	MPa	Defines the stiffness compatibility between the repair material and aged asphalt layer.
	Repair material Poisson's ratio, ν_r	0.33–0.38	-	Controls lateral deformation and local stress redistribution within the repair zone.

Table 3. *Cont.*

Parameter Group	Parameter	Adopted Value/Range	Unit	Role in the Simulation
Repair interface behavior	Interface normal stiffness, K_n	1.0×10^6–5.0×10^6	MPa/m	Controls normal traction transfer between the existing pavement and repair material.
	Interface shear stiffness, $K_s = K_t$	0.5×10^6–3.0×10^6	MPa/m	Controls tangential load transfer and resistance against repair interface slip.
	Interface tensile strength, t_n^0	0.60–1.20	MPa	Determines the onset of normal debonding at the repair–pavement interface.
	Interface shear strength, $t_s^0 = t_t^0$	0.45–0.90	MPa	Defines the resistance of the repair interface against shear-induced damage.
	Interface fracture energy, G_{int}	150–400	N/m	Controls progressive degradation of the repair interface after damage initiation.
	Bonding quality factor, B_q	0.40–1.00	-	Represents weak, moderate, and strong bonding states after thermal conditioning.
	Interface damage variable, D_{int}	0–1	-	Quantifies progressive repair interface degradation under post-repair service loading.
	Contact behavior	Cohesive traction separation with damage evolution	-	Enables coupled assessment of bonding quality, interface stress, and repair durability.
Thermal repair operation	Maximum repair heat flux, q_{max}	8–18	kW/m^2	Represents the maximum thermal energy input available for repair zone conditioning.
	Energy-limited amplitude, $A_E(t)$	0.0–1.0	-	Scales the applied heat flux according to available PV-battery energy.
	Thermal conditioning duration	5–25	min	Defines the repair heating window allowed by available work zone energy.
	Initial pavement temperature	20–35	°C	Represents ambient pavement temperature before energy-limited repair heating.
	Target repair zone temperature	55–85	°C	Defines the thermal softening/conditioning range required to improve repair bonding.
	Convection coefficient, h_c	8–15	W/m^2·K	Controls heat exchange between pavement surface and surrounding air during repair.
	Ambient air temperature	25–40	°C	Defines external thermal boundary condition during maintenance operation.
Traffic and service loading	Tire contact pressure, p	550–800	kPa	Represents wheel-induced surface pressure during pre-repair and post-repair loading.
	Contact patch radius	90–130	mm	Defines the effective tire–pavement contact area used in service loading.
	Standard axle load	80	kN	Represents the reference traffic loading condition for pavement response evaluation.
	Heavy axle load scenario	100–120	kN	Represents overloaded traffic conditions that accelerate crack growth and repair degradation.
	Loading cycles	1.0×10^3–1.0×10^5	cycles	Defines repeated service loading used to evaluate crack evolution and post-repair durability.
	Load application stage	Pre-repair and post-repair	-	Enables comparison of crack driving response before and after maintenance intervention.
	Critical response outputs	σ_{max}, u_z, Δa, D_c, D_{int}	-	Provides structural response indicators used for dataset generation and repair ranking.

Table 3. *Cont.*

Parameter Group	Parameter	Adopted Value/Range	Unit	Role in the Simulation
Maintenance performance indicators	Crack growth length, Δa	Simulation output	mm	Measures the crack extension before and after repair intervention.
	Crack growth reduction ratio, $R_{\Delta a}$	0–100	%	Quantifies the ability of the repair strategy to suppress further crack propagation.
	Maximum stress reduction, R_{σ}	0–100	%	Measures the decrease in maximum principal stress after repair activation.
	Energy feasibility indicator, F_E	0 or 1	-	Identifies whether available work-zone energy is sufficient to complete the repair operation.
	Repair durability index, R_d	0–1	-	Aggregates crack control, interface integrity, stress reduction, and thermal conditioning effectiveness.
	Service life gain, ΔN_f	Simulation/AI output	years or cycles	Estimates the expected improvement in pavement life after the selected maintenance strategy.

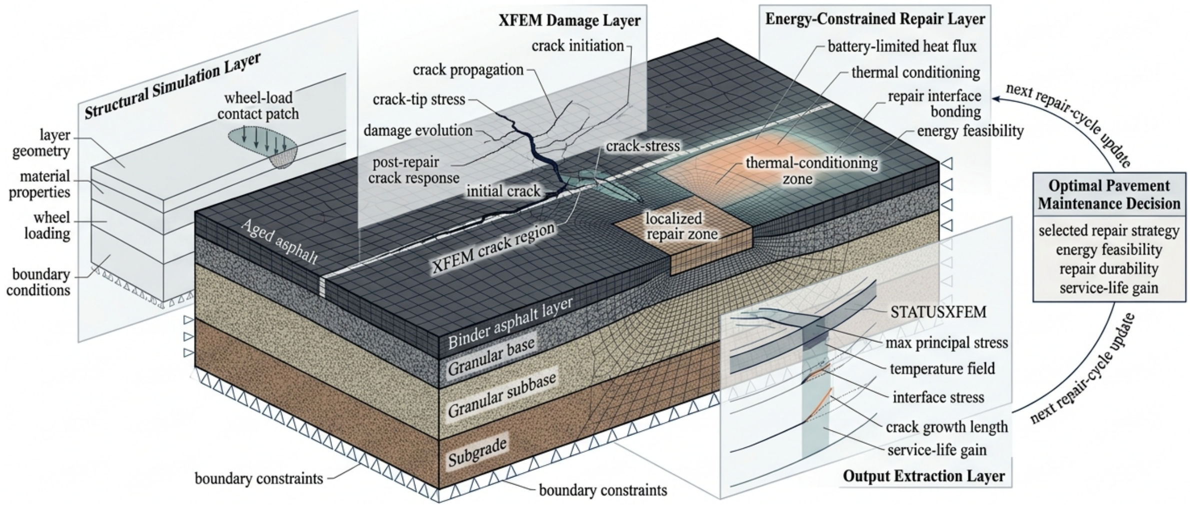

Figure 2. Layered XFEM-based simulation blueprint for energy-constrained pavement crack repair and maintenance decision support.

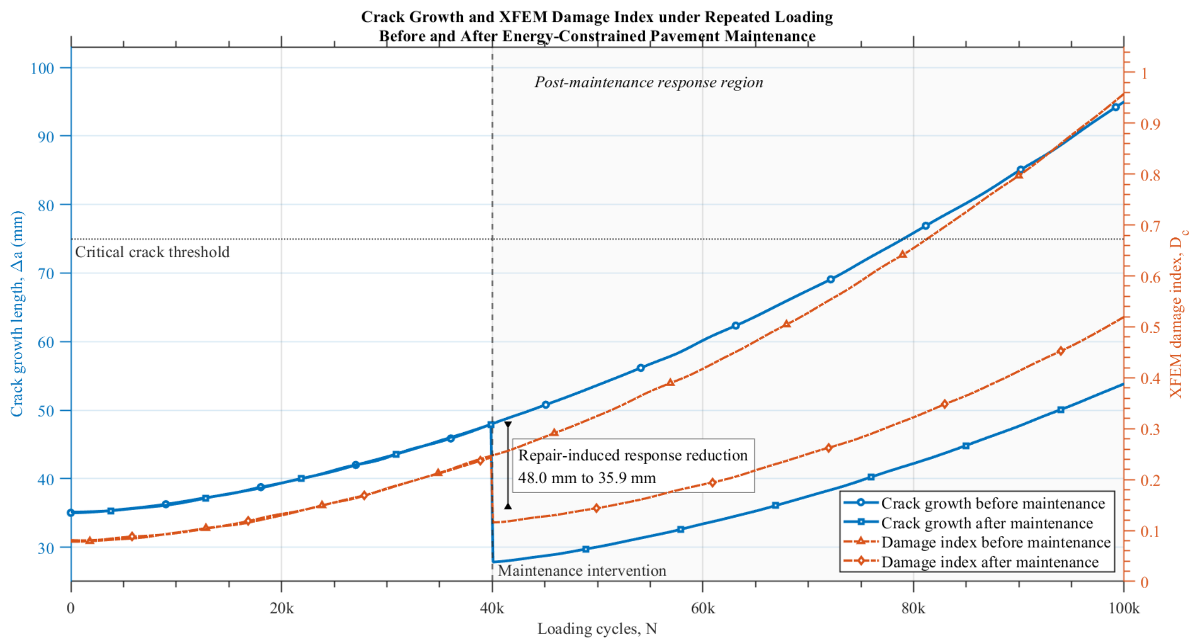

Figure 3. Effect of energy-constrained maintenance on pavement crack growth and XFEM damage evolution under repeated loading.

3.3. Energy-Constrained Repair Scenarios and Generated Dataset

The energy-constrained repair stage was designed to represent the practical limitation that pavement maintenance operations are not always executed under unlimited energy availability. In the proposed simulation, the repair process is activated after XFEM-based crack evolution reaches the intervention stage, and the localized repair zone is subjected to a controlled thermal conditioning process. The repair heat input is governed by a battery-limited amplitude function, where the normalized energy coefficient $A_E(t)$ varies between 0.0 and 1.0 and directly scales the applied heat flux during the maintenance window. The maximum repair heat flux was defined within the range of 8–18 $\mathrm{kW/m^2}$, while the thermal conditioning duration was varied between 5 and 25 min to represent short, moderate, and extended repair heating operations. This formulation allows the simulation to distinguish between energy-feasible and energy-limited repair cases, where insufficient available energy may reduce the repair temperature field, weaken interface bonding, and decrease post-maintenance durability.

The generated repair scenarios combine structural, fracture, thermal, and operational variables to create a comprehensive simulation database. Crack severity was varied using initial crack lengths of 35–75 mm and crack depths of 15–45 mm, while repair zone geometry was represented using repair lengths of 300–600 mm, widths of 180–350 mm, and thicknesses of 30–70 mm. The repair operation was evaluated under different bonding conditions, with the bonding quality factor B_q ranging from 0.40 to 1.00 to represent weak, moderate, and strong repair interface states. Traffic loading was introduced through tire contact pressures of 550–800 kPa, reference axle loading of 80 kN, and heavy axle scenarios of 100–120 kN. These variables were combined with thermal and energy inputs, including battery state of charge, heat-flux amplitude, repair duration, ambient temperature of 25–40 °C, and target repair zone temperature of 55–85 °C. Therefore, each generated scenario represents a distinct pavement maintenance condition in which the structural response depends simultaneously on crack geometry, repair configuration, wheel loading, interface quality, and available repair energy.

After each simulation run, the finite-element and XFEM outputs were extracted and converted into a structured dataset for the AI-based repair strategy optimization stage. The output database includes mechanical responses such as maximum principal stress, vertical displacement, interface stress, crack growth length, and XFEM damage status in addition to thermal and repair operation responses such as temperature field, energy feasibility, heat flux efficiency, repair durability, and service life gain. The repair strategy label was assigned according to the simulated performance of candidate maintenance actions, including delayed repair, crack sealing, localized patch repair, thin overlay, and deep repair intervention. In this way, the generated dataset does not represent arbitrary synthetic data; rather, it is a simulation-derived database constructed from coupled structural and thermal energy responses. This dataset enables the AI model to learn the relationship between pavement condition, repair energy availability, repair quality, and post-maintenance performance, allowing the final optimization process to select the repair strategy that minimizes crack propagation and stress concentration while maximizing durability and service life extension. Although the generated database provides a controlled and physically consistent representation of a wide range of pavement repair conditions, it remains entirely simulation-derived and cannot reproduce every source of variability encountered in field maintenance operations. A potential simulation-to-reality gap may arise from spatial material heterogeneity, construction variability, uncertain pavement aging, moisture and seasonal effects, irregular traffic spectra, imperfect repair placement, field-dependent interface bonding, and measurement noise that are necessarily simplified in the finite-element environment. To reduce the risk of CERIG-Net learning only a narrow numerical domain, the simulation scenarios were intentionally distributed across broad ranges of crack geometry, material and fracture properties, repair-zone dimensions, loading levels, interface conditions, thermal inputs, and PV battery energy states. This parameter variation acts as a physics-based domain randomization mechanism by exposing the learning model to substantially different combinations of pavement condition and repair operation rather than repetitions of a single nominal configuration. In addition, the graph representation used by CERIG-Net preserves explicit material–crack, energy–thermal, thermal–interface, and interface–structural dependency pathways, while the physics-guided loss terms constrain the predicted responses to remain consistent with the governing structural, fracture, thermal, and energy relationships. The uncertainty estimation branch further provides a means of identifying predictions associated with lower confidence when the input condition departs from well-represented regions of the simulation domain. Nevertheless, these mechanisms reduce generalization risk rather than establish direct field generalization. Consequently, application to operational pavement maintenance should include external laboratory and field validation followed where necessary by recalibration, transfer learning, or domain adaptation using measured pavement response and repair performance data. The experimentally supported XFEM comparisons presented in Section 4 provide an initial physical bridge between the numerical crack evolution domain and observed asphalt fracture behavior, while direct field-based validation of CERIG-Net remains an important stage for subsequent deployment. To quantify the influence of input uncertainty on the predicted pavement repair performance, a structured multi-factor sensitivity analysis was performed using the physically admissible parameter ranges defined in Table 4. The investigated variables were grouped into three principal uncertainty domains: material and fracture properties, initial crack geometry, and repair energy availability. The material property analysis considered variations in the asphalt tensile strength from 1.20 to 1.80 MPa, shear strength from 0.85 to 1.30 MPa, mode-I fracture energy G_{Ic} from 350 to 650 N/m, mode-II fracture energy G_{IIc} from 500 to 850 N/m, normal interface stiffness K_n from 1.0×10^6 to 5.0×10^6 MPa/m, shear interface stiffness K_s from 0.5×10^6 to 3.0×10^6 MPa/m, and interface fracture energy G_{int} from 150 to 400 N/m. Initial crack uncertainty was represented by varying the crack length a_0 from 35 to 75 mm, crack depth d_0 from 15 to 45 mm, and crack inclination θ_c from 0° to 25°. Energy-related uncertainty was evaluated through the available ranges of the normalized energy amplitude A_E from 0.20 to 1.00, applied heat flux from 8 to 18 kW/m^2, heating duration from 5 to 25 min, and initial battery state of charge from 30% to 100%. For each parameter variation, the resulting changes in final crack length, maximum principal stress, interface damage D_{int}, repair durability index R_d, energy feasibility state F_E, and service life gain ΔN_f were recorded while the remaining variables were maintained at their nominal reference values. This procedure provides a consistent basis for identifying the parameters that most strongly influence structural recovery, interface integrity, thermal adequacy, and the resulting repair strategy decision.

Figure 4 illustrates how the repair heat flux amplitude is governed by the available PV battery energy during the energy-constrained pavement maintenance operation. The low-energy case, initialized at $SOC_0 = 35\%$ and $PV = 0.35$, reaches only a moderate amplitude plateau of approximately $A_E(t) = 0.65$, remaining close to the minimum feasible heating threshold of 0.60, which indicates that the repair process is possible but thermally limited. In contrast, the medium-energy case ($SOC_0 = 60\%, PV = 0.65$) achieves a stronger heating response of about $A_E(t) = 0.90$, corresponding to an applied heat flux of nearly 16.2 kW/m^2 from the maximum $q_{\max} = 18$ kW/m^2. The high-energy case ($SOC_0 = 85\%, PV = 0.90$) maintains the maximum normalized amplitude $A_E(t) \approx 1.0$ for a longer interval, showing that sufficient stored and renewable energy can sustain the thermal conditioning plateau before the decay phase begins. This figure demonstrates that the repair operation is not modeled as a constant ideal heat source; instead, the available energy directly controls the heating intensity, feasible conditioning duration, and potential repair quality. This supports the proposed methodology by linking the simulated repair performance to realistic energy-constrained work zone conditions.

Table 4. Generated simulation dataset features and target variables for AI-based pavement repair strategy optimization.

Feature Group	Feature/Target Variable	Value or Range	Unit/Type	Purpose in the Generated Dataset
Pavement geometry	Aged asphalt surface thickness	50	mm	Defines the cracked upper layer where XFEM crack initiation and repair activation occur.
	Binder asphalt layer thickness	70	mm	Controls intermediate asphalt stiffness contribution and stress distribution below the surface layer.
	Asphalt base layer thickness	100	mm	Represents lower asphalt support and affects vertical load transfer under wheel loading.
	Granular base thickness	200	mm	Controls load spreading between asphalt layers and lower pavement foundation.
	Granular sub-base thickness	250	mm	Represents intermediate foundation support and affects vertical displacement response.
	Sub-grade depth	1000	mm	Provides lower boundary support and controls global pavement deflection.
Crack geometry	Initial crack length, a_0	35–75	mm	Represents the initial crack severity before maintenance intervention.
	Initial crack depth, d_0	15–45	mm	Defines the penetration depth of cracking within the aged asphalt layer.
	Crack inclination angle, θ_c	0–25	degree	Represents non-vertical crack orientation under combined thermal and traffic effects.
	XFEM enriched domain width	250	mm	Defines the local domain where displacement discontinuity and crack enrichment are activated.
	XFEM enriched domain length	450	mm	Provides sufficient space for crack propagation before and after repair.
	Refined crack tip mesh size	5–8	mm	Controls local numerical resolution around crack-tip stress concentration.
Repair configuration	Repair strategy candidate	Delayed repair; crack sealing; localized patch; thin overlay; deep repair	Class label	Defines the candidate maintenance action evaluated by the AI optimization stage.
	Localized repair zone length	300–600	mm	Controls the longitudinal extent of the treated crack region.
	Localized repair zone width	180–350	mm	Defines the lateral coverage of the repair intervention around the crack path.
	Repair zone thickness	30–70	mm	Controls repair material contribution to surface layer recovery.
	Thin overlay thickness	40–60	mm	Represents overlay-type maintenance when the selected treatment is thin overlay.
	Repair material modulus, E_r	2500–5000	MPa	Defines stiffness compatibility between repair material and aged asphalt surface.

Table 4. *Cont.*

Feature Group	Feature/Target Variable	Value or Range	Unit/Type	Purpose in the Generated Dataset
Interface behavior	Interface normal stiffness, K_n	1.0×10^6–5.0×10^6	MPa/m	Controls normal traction transfer between existing pavement and repair material.
	Interface shear stiffness, $K_s = K_t$	0.5×10^6–3.0×10^6	MPa/m	Controls resistance against shear slip along the repair interface.
	Interface tensile strength, t_n^0	0.60–1.20	MPa	Defines the onset of normal debonding at the repair interface.
	Interface shear strength, $t_s^0 = t_t^0$	0.45–0.90	MPa	Defines the onset of shear-induced interface damage.
	Bonding quality factor, B_q	0.40–1.00	Dimensionless	Represents weak, moderate, and strong bonding states after thermal conditioning.
Energy and thermal inputs	Maximum repair heat flux, $q_{\max}$	8–18	$\mathrm{kW/m^2}$	Defines the maximum thermal input available for repair zone conditioning.
	Energy-limited amplitude, $A_E(t)$	0.0–1.0	Dimensionless	Scales the applied repair heat flux according to PV battery availability.
	Battery state of charge, SOC	20–100	%	Represents the available stored energy for repair equipment operation.
	Thermal conditioning duration	5–25	min	Controls the duration of energy-limited heating applied to the repair zone.
	Initial pavement temperature	20–35	°C	Represents the pavement temperature before repair heating begins.
	Target repair zone temperature	55–85	°C	Defines the thermal conditioning level required to improve repair bonding.
	Convection coefficient, h_c	8–15	$\mathrm{W/m^2 \cdot K}$	Controls heat exchange between the pavement surface and surrounding air.
Traffic loading	Tire contact pressure, p	550–800	kPa	Represents wheel-induced surface pressure during service loading.
	Contact patch radius	90–130	mm	Defines the effective tire–pavement contact area.
	Standard axle load	80	kN	Represents the reference loading case for normal traffic conditions.
	Heavy axle load	100–120	kN	Represents overloaded traffic scenarios that accelerate damage evolution.
	Loading cycles, N	1.0×10^3–1.0×10^5	cycles	Defines repeated service loading used to evaluate pre- and post-repair behavior.
Simulation outputs	XFEM crack status	0–1	Damage state	Indicates whether the crack is inactive, initiated, propagating, or fully damaged.
	Crack growth length, Δa	Simulation output	mm	Measures crack extension before and after maintenance intervention.
	Maximum principal stress, $\sigma_{\max}$	Simulation output	MPa	Quantifies critical tensile stress concentration around the crack and repair zone.
	Vertical displacement, u_z	Simulation output	mm	Measures pavement surface and structural deformation under wheel loading.
	Temperature field, T	Simulation output	°C	Represents repair zone temperature distribution during energy-limited conditioning.
	Interface stress, τ_{int}	Simulation output	MPa	Evaluates stress transfer and potential debonding at the repair interface.
	Interface damage, D_{int}	0–1	Dimensionless	Quantifies progressive degradation of repair interface bonding.
	Energy feasibility indicator, F_E	0 or 1	Binary target	Identifies whether available energy is sufficient to complete the repair operation.

https://doi.org/10.3390/math14173149

Table 4. *Cont.*

Feature Group	Feature/Target Variable	Value or Range	Unit/Type	Purpose in the Generated Dataset
AI target variables	Repair durability index, R_d	0–1	Regression target	Aggregates crack control, stress reduction, interface integrity, and thermal effectiveness.
	Crack growth reduction ratio, $R_{\Delta a}$	0–100	%	Measures the effectiveness of the repair strategy in suppressing crack propagation.
	Maximum stress reduction, R_σ	0–100	%	Measures the reduction in critical stress after repair activation.
	Service life gain, ΔN_f	Simulation/AI output	years or cycles	Estimates the expected extension in pavement service life after maintenance.
	Selected repair strategy, S^*	S0–S4	Class label	Defines the optimal maintenance decision selected from candidate repair alternatives.

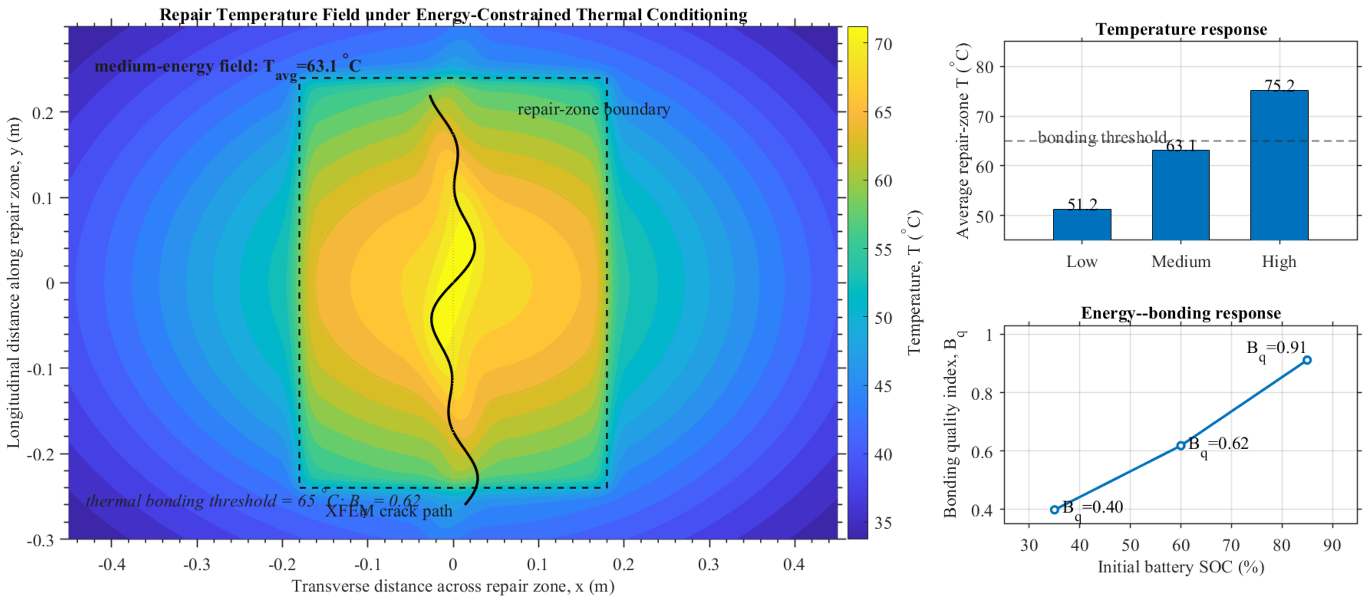

Figure 4. Crack growth suppression and XFEM damage reduction before and after energy-constrained pavement maintenance.

Figure 5 shows the spatial temperature field generated during the medium-energy thermal conditioning case and its effect on repair zone bonding quality. The contour map indicates that the localized repair zone reaches a concentrated thermal field around the XFEM crack path, with an average repair zone temperature of approximately 63.1 °C, which is slightly below the target bonding threshold of 65 °C. This explains why the corresponding bonding quality index remains moderate at $B_q = 0.62$ rather than reaching the stronger bonding response observed under the high-energy condition. The side temperature response plot confirms the energy sensitivity of the repair process: the low-energy case produces only 51.2 °C, the medium case reaches 63.1 °C, and the high-energy case reaches 75.2 °C, clearly exceeding the bonding threshold. Similarly, the bonding response increases from $B_q = 0.40$ at 35% SOC to $B_q = 0.62$ at 60% SOC and $B_q = 0.91$ at 85% SOC. These results indicate that energy availability strongly influences the thermal adequacy of the repair zone, the quality of interface bonding, and the expected durability of the maintenance action. Therefore, the figure provides a direct mechanistic link between battery-supported repair energy, temperature distribution, and post-repair structural reliability.

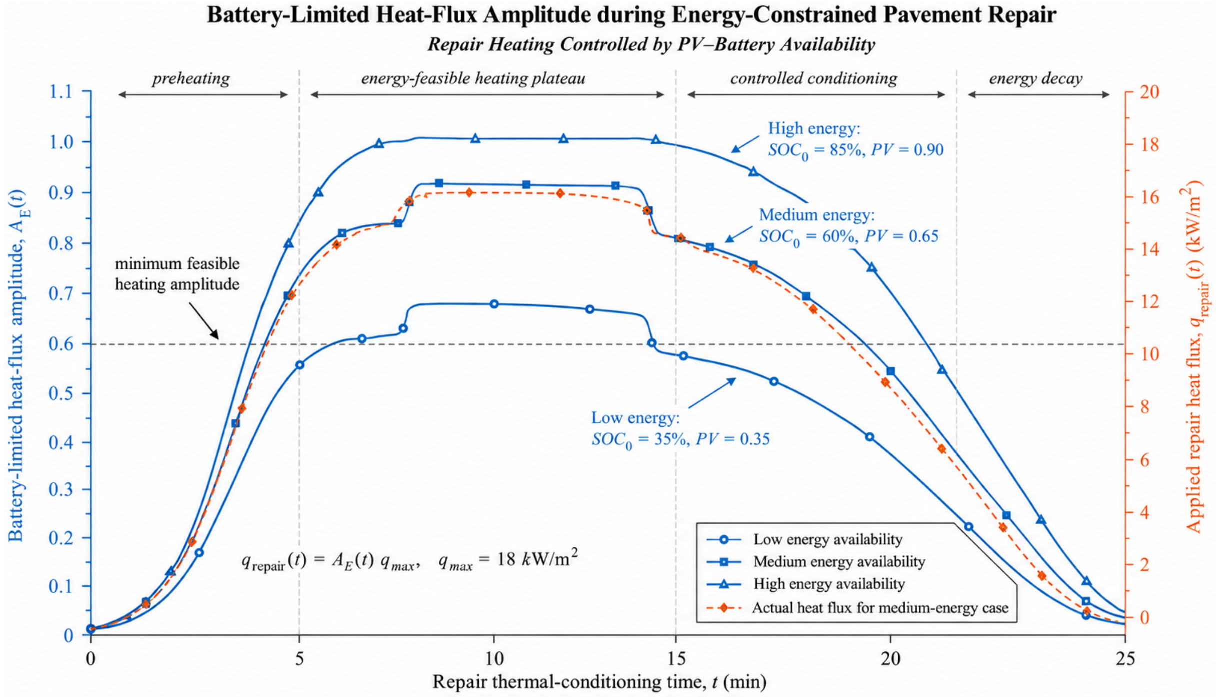

Figure 5. PV battery-controlled heat flux amplitude for energy-constrained pavement repair thermal conditioning.

3.4. CERIG-Net-Based Repair Strategy Optimization and Model Evaluation

The proposed AI model is formulated as a Crack–Energy–Repair Interaction Graph Network, denoted as CERIG-Net, that learns the coupled relationship between XFEM crack evolution, energy-constrained thermal repair, interface bonding, and post-maintenance pavement performance. Instead of treating the generated simulation dataset as a conventional flat feature table, CERIG-Net converts each simulated pavement repair scenario into a physics-guided graph representation. In this graph, the main physical and operational components of the maintenance process are represented as interacting nodes, including the crack state node, material property node, energy availability node, thermal conditioning node, repair interface node, structural response node, and repair strategy node. This graph structure allows the model to preserve the causal sequence of the simulated repair process, where crack geometry and material stiffness affect stress concentration and XFEM damage evolution, energy availability controls the applied repair heat flux, heat flux determines the repair zone temperature response, temperature influences bonding quality, and bonding quality affects post-repair crack growth, interface damage, and service life gain.

CERIG-Net learns these physical dependencies through a graph message-passing mechanism in which each node updates its internal representation by receiving information from physically connected neighboring nodes. For example, the energy availability node transfers information related to battery state of charge, PV contribution, and heat flux amplitude to the thermal conditioning node; the thermal node communicates the repair zone temperature response to the repair interface node; and the interface node transfers bonding and damage information to the structural response node. In parallel, the crack state and material property nodes influence the structural response node through the crack length, crack depth, crack inclination, fracture energy, asphalt stiffness, and loading conditions. Rather than fitting direct statistical correlations between input features and output labels, CERIG-Net uses repeated message-passing layers to learns the hidden interaction pathways that control pavement repair effectiveness. This makes the model more suitable for the proposed simulation framework, since the repair decision depends on coupled physical mechanisms instead of isolated variables.

Model generalization was addressed by combining broad scenario coverage, physics-guided representation, held-out evaluation, and uncertainty-aware prediction, since relying solely on statistical interpolation could limit the results to a narrow simulation range. The training database spanned variations in crack length, crack depth, crack inclination, material and fracture properties, traffic loading, repair geometry, bonding quality, thermal conditioning duration, heat flux intensity, and PV battery energy availability, thereby exposing CERIG-Net to substantially different structural–thermal–energy combinations during learning. The training and evaluation samples were separated so that predictive performance was assessed on pavement repair cases that were not used for parameter optimization, thereby reducing the likelihood of the reported performance reflecting direct memorization of individual simulation scenarios. More importantly, the heterogeneous graph structure constrains information exchange to physically meaningful pathways such as material-to-crack, crack-to-structural response, energy-to-thermal, thermal-to-interface, and interface-to-repair performance interactions. The physics-guided loss terms further penalize predictions that violate the structural, fracture, thermal, and energy relationships embedded in the simulation framework, providing an additional regularization mechanism beyond conventional data-driven training. CERIG-Net also incorporates an uncertainty estimation branch that produces confidence information for predicted repair responses, allowing cases with comparatively high predictive uncertainty to be distinguished from well-supported predictions within the simulated domain. These mechanisms improve robustness to unseen combinations of the investigated numerical conditions; however, they do not by themselves guarantee generalization to all real pavement environments. Field application will require external validation; where systematic differences between simulated and measured responses are observed, it will also be necessary to incorporate model recalibration, transfer learning, or domain adaptation using laboratory and field maintenance data.

The output stage of CERIG-Net is designed as a multi-task prediction and strategy ranking system. The model simultaneously predicts key simulation-derived responses, including crack growth length, maximum principal stress, average repair zone temperature, interface damage, repair durability index, energy feasibility, and service life gain. These outputs are then used to rank the candidate pavement maintenance strategies, including delayed repair, crack sealing, localized patch repair, thin overlay, and deep repair intervention. The final strategy is selected using a physics-constrained decision score that penalizes excessive crack propagation, high stress concentration, severe interface damage, high repair energy demand, and failure risk while rewarding energy-feasible repair execution, improved bonding, higher durability, and longer service life extension. Therefore, CERIG-Net functions as both a predictive surrogate model and a repair decision optimizer, enabling the proposed framework to identify the most structurally effective and energy-feasible pavement maintenance strategy from the simulation-generated scenarios.

Figure 6 illustrates the proposed CERIG-Net architecture, which converts each simulation-derived pavement repair case into a physics-guided heterogeneous graph. The graph represents the main interacting domains of the maintenance process, including material properties, energy availability, crack condition, repair interface, structural response, and candidate repair strategy. Instead of treating the dataset as independent tabular variables, CERIG-Net encodes node features, edge relations, node types, and interaction types into latent representations that preserve the physical dependency between crack evolution, energy-limited thermal conditioning, interface bonding, and post-repair durability. The deep reasoning core combines heterogeneous graph encoding, multi-head graph attention, physics-guided message-passing, cross-domain interaction fusion, and residual graph refinement to produce a latent repair state embedding z_G. This embedding is then used to predict key repair responses, including crack growth Δa, maximum principal stress $\sigma_{\max}$, average repair temperature T_{avg}, interface damage D_{int}, repair durability R_d, energy feasibility FE, and service life gain ΔN_f. The uncertainty branch performs estimation of μ and σ^2, allowing the model to quantify confidence in the predicted repair responses. Finally, the strategy-ranking layer compares the candidate maintenance actions S_1–S_5, including delay, sealing, patching, overlay, and deep repair, and selects the optimal maintenance decision S^* based on structural performance, energy feasibility, durability, and service life improvement.

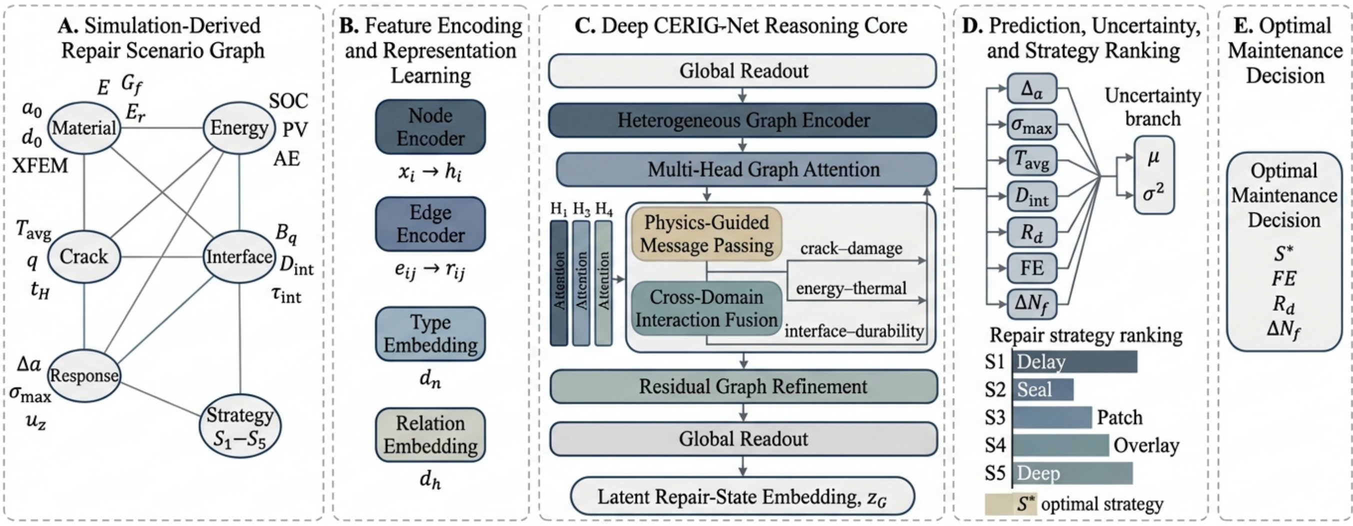

Figure 6. CERIG-Net architecture for learning physics-guided crack–energy–repair interactions and recommending optimized maintenance strategies.

To distinguish CERIG-Net mathematically from conventional graph architectures, consider a graph node v_i with representation $\mathbf{h}_i^{(\ell)}$ at layer ℓ. A standard graph convolutional network (GCN) performs neighborhood aggregation using a shared transformation matrix and topology-dependent normalization

$$\mathbf{h}_i^{(\ell+1)} = \sigma\left(\sum_{j\in\mathcal{N}(i)\cup\{i\}} \frac{1}{\sqrt{d_i d_j}} \mathbf{W}^{(\ell)} \mathbf{h}_j^{(\ell)}\right), \tag{22}$$

where d_i and d_j are node degrees and $\mathbf{W}^{(\ell)}$ is shared across neighboring interactions. This formulation propagates information according to graph connectivity, but does not explicitly distinguish the physical meaning of different node or edge types. A conventional graph attention network (GAT) replaces fixed normalized aggregation by learned attention:

$$\alpha_{ji}^{(\ell)} = \text{softmax}_{j\in\mathcal{N}(i)}\left[\text{LeakyReLU}\left(\mathbf{a}^T\left[\mathbf{W}\mathbf{h}_j^{(\ell)} \| \mathbf{W}\mathbf{h}_i^{(\ell)}\right]\right)\right], \tag{23}$$

$$\mathbf{h}_i^{(\ell+1)} = \sigma\left(\sum_{j\in\mathcal{N}(i)} \alpha_{ji}^{(\ell)} \mathbf{W}\mathbf{h}_j^{(\ell)}\right). \tag{24}$$

Although GATs allow neighboring nodes to contribute with different learned importance, the standard formulation still treats the interaction primarily through node embeddings, and cannot explicitly encode whether an edge represents a material–crack, energy–thermal, thermal–interface, or interface–structural dependency. Thus, CERIG-Net instead initializes node representations according to their physical type:

$$\mathbf{h}_i^{(0)} = \phi_{\tau_i}(\mathbf{x}_i), \qquad \mathbf{r}_{ji} = \phi_e(\mathbf{e}_{ji}, \rho_{ji}) \tag{25}$$

where τ_i denotes the node type and ρ_{ji} denotes the physical interaction type associated with edge (j,i). The attention coefficient explicitly includes the encoded physical relation:

$$\alpha_{ji}^{(\ell)} = \text{softmax}_{j\in\mathcal{N}(i)}\left[\mathbf{a}^T\left(\mathbf{W}_h\mathbf{h}_j^{(\ell-1)}\|\mathbf{W}_h\mathbf{h}_i^{(\ell-1)}\|\mathbf{W}_e\mathbf{r}_{ji}\right)\right] \tag{26}$$

and the corresponding physics-aware message and node update are as follows:

$$\mathbf{m}_{ji}^{(\ell)} = \alpha_{ji}^{(\ell)}\psi\left(\mathbf{h}_j^{(\ell-1)},\mathbf{h}_i^{(\ell-1)},\mathbf{r}_{ji}\right), \qquad \mathbf{M}_i^{(\ell)} = \sum_{j\in\mathcal{N}(i)}\mathbf{m}_{ji}^{(\ell)}, \tag{27}$$

$$\mathbf{h}_i^{(\ell)} = \text{GRU}\left(\mathbf{h}_i^{(\ell-1)},\mathbf{M}_i^{(\ell)}\right) + \mathbf{h}_i^{(\ell-1)}. \tag{28}$$

Therefore, the principal distinction is that while a GCN aggregates neighboring states using topology-based weights and a GAT additionally learns neighbor importance, CERIG-Net conditions message transfer on both the node state and the physical interaction represented by the connecting edge. In the graph, information is restricted to physically defined pathways such as material-to-crack, crack-to-response, energy-to-thermal, thermal-to-interface, interface-to-response, and response-to-strategy interactions. In this way, the heterogeneous representation retains the mechanistic organization of the simulated repair process and prevents all variables from being treated as interchangeable graph entities.

A second distinction concerns the learning objective. In GCN and GAT, baselines are trained using only the task-dependent predictive losses:

$$\mathcal{L}_{\text{data}} = \lambda_1\mathcal{L}_{\Delta a} + \lambda_2\mathcal{L}_\sigma + \lambda_3\mathcal{L}_T + \lambda_4\mathcal{L}_D + \lambda_5\mathcal{L}_{R_d} + \lambda_6\mathcal{L}_{F_E} + \lambda_7\mathcal{L}_S \tag{29}$$

whereas CERIG-Net augments this objective by including physics-based consistency penalties:

$$\mathcal{L}_{\text{CERIG}} = \mathcal{L}_{\text{data}} + \lambda_8(\mathcal{L}_q + \mathcal{L}_E + \mathcal{L}_R), \tag{30}$$

$$\mathcal{L}_q = \left\|\widehat{q}_{\text{repair}} - A_E q_{\max}\right\|_2^2, \qquad \mathcal{L}_E = \left\|\widehat{F}_E - I(E_{\text{available}} \geq E_{\text{repair}})\right\|_2^2, \tag{31}$$

$$\mathcal{L}_R = \left\|\widehat{R}_d - \Phi\left(\widehat{\Delta a},\widehat{\sigma}_{\max},\widehat{D}_{\text{int}},\widehat{F}_E\right)\right\|_2^2. \tag{32}$$

In this way, the advantage of CERIG-Net is not simply increased graph model complexity; rather, it is the combined effect of heterogeneous physical representation, relation-conditioned message-passing, and explicit consistency with the simulated energy and repair mechanisms.

Algorithm 1 summarizes the complete CERIG-Net computational procedure for physics-constrained pavement repair strategy optimization. The algorithm starts from the simulation-derived dataset $\mathcal{D} = \{X_i, Y_i\}_{i=1}^{N_s}$ in which each case contains pavement geometry, XFEM crack descriptors, material properties, energy variables, thermal conditioning inputs, repair interface parameters, structural responses, and candidate strategy labels. Instead of feeding these variables directly into a conventional tabular model, each scenario is first converted into a heterogeneous graph $G_i = (V_i, E_i)$ in which the node set includes the material node v_m, energy node v_e, crack node v_c, thermal conditioning node v_t, repair interface node v_{int}, response node v_r, and strategy node v_s. The material node stores properties such as E, G_f, E_r, ν, and ρ; the energy node represents SOC, PV, A_E, $q_{\max}$, and available energy; the crack node includes a_0, d_0, θ_c, the XFEM state, and D_c; the thermal node contains q_{repair}, t_H, T_{avg}, h_c, and T_{amb}; the interface node includes B_q, D_{int}, τ_{int}, K_n, and K_s; the response node includes Δa, $\sigma_{\max}$, u_z, R_d, and ΔN_f; and the strategy node includes the candidate maintenance actions S_1–S_5. The physical edges are then defined to preserve the simulated dependency pathways such as material-to-crack, crack-to-response, energy-to-thermal, thermal-to-interface, interface-to-response, response-to-strategy, and strategy-to-response interactions. During training, node and edge features are encoded into latent embeddings. CERIG-Net applies multi-layer graph attention and physics-guided message-passing so that each node updates its state using information from physically connected neighbors. This allows the model to learn how energy availability controls heat flux, heat flux controls thermal conditioning, temperature affects interface bonding, interface damage modifies stress redistribution, and these combined responses collectively determine repair durability and strategy selection. The model then simultaneously predicts multiple simulation-derived outputs, including $\widehat{\Delta a}$, $\hat{\sigma}_{\max}$, $\hat{T}_{\text{avg}}$, $\hat{D}_{\text{int}}$, $\hat{R}_d$, $\widehat{FE}$, $\widehat{\Delta N_f}$, and $\hat{P}(S)$, while an uncertainty branch estimates μ and σ^2 to represent prediction confidence. The loss function combines regression losses, feasibility classification loss, strategy-ranking loss, and physics consistency penalties, including the heat flux constraint $q_{\text{repair}} = A_E q_{\max}$, energy feasibility condition $FE = \mathbb{I}(E_{\text{available}} \geq E_{\text{repair}})$, and durability consistency between R_d, crack growth, stress, interface damage, and feasibility. After training and validation, CERIG-Net evaluates each candidate repair strategy using a physics-constrained decision score $J_i(s)$ which penalizes crack growth, maximum stress, interface damage, energy demand, and failure risk while rewarding repair durability and service life gain. Strategies that violate energy feasibility receive an additional penalty Ω_E, ensuring that the final recommendation is not only structurally effective but also operationally feasible under the available repair energy. The selected strategy $S_i^* = \arg\min_{s \in \mathcal{S}} J_i(s)$ is the repair action that provides the best balance between crack growth control, stress reduction, interface integrity, energy feasibility, durability improvement, and service life extension. Finally, the model is evaluated using regression metrics such as R^2, RMSE, and MAE, classification metrics such as accuracy, precision, recall, and F1-score, and decision-level indicators such as strategy ranking consistency, energy feasibility agreement, and Pareto dominance.

Algorithm 1: CERIG-Net training and physics-constrained pavement repair strategy optimization

Input: Simulation-derived dataset $\mathcal{D} = \{X_i, Y_i\}_{i=1}^{N_s}$; candidate repair strategies $\mathcal{S} = \{S_1, S_2, S_3, S_4, S_5\}$; maximum repair heat flux $q_{\max}$; learning rate η; maximum epochs $E_{\max}$; loss weights $\lambda_1, \ldots, \lambda_8$; decision weights $\omega_1, \ldots, \omega_7$.

Output: Trained CERIG-Net model Θ^*; predicted repair responses $\hat{Y}$; ranked repair strategies $\mathcal{R}$; optimal maintenance decision S^*.

Function `BuildGraph`(X_i)
- Define physical node set $V_i = \{v_m, v_e, v_c, v_t, v_{\text{int}}, v_r, v_s\}$
- Assign material node features $x_m = [E, G_f, E_r, \nu, \rho]$
- Assign energy node features $x_e = [SOC, PV, A_E, q_{\max}, E_{\text{available}}]$
- Assign crack node features $x_c = [a_0, d_0, \theta_c, \text{XFEM}, D_c]$
- Assign thermal node features $x_t = [q_{\text{repair}}, t_H, T_{\text{avg}}, h_c, T_{\text{amb}}]$
- Assign interface node features $x_{\text{int}} = [B_q, D_{\text{int}}, \tau_{\text{int}}, K_n, K_s]$
- Assign response node features $x_r = [\Delta a, \sigma_{\max}, u_z, R_d, \Delta N_f]$
- Assign strategy node features $x_s = [S_1, S_2, S_3, S_4, S_5]$
- Define physical dependency edges: $E_i = \{v_m \to v_c,\ v_c \to v_r,\ v_e \to v_t,\ v_t \to v_{\text{int}},\ v_{\text{int}} \to v_r,\ v_r \to v_s,\ v_s \to v_r\}$
- Attach edge attributes e_{ij} representing interaction type, direction, and strength
- **return** graph $G_i = (V_i, E_i, X_i, E_i^{attr})$

Function `MessagePassing`(G_i, Θ)
- Initialize node embeddings $h_k^{(0)} = \phi_n(x_k)$ for each node $v_k \in V_i$
- Initialize edge embeddings $r_{jk} = \phi_e(e_{jk})$ for each edge $(j,k) \in E_i$
- **for** $\ell = 1$ **to** L **do**
  - **foreach** *node* $v_k \in V_i$ **do**
    - Compute attention weight for each neighbor $v_j \in \mathcal{N}(k)$: $\alpha_{jk}^{(\ell)} = \text{softmax}\Big(a^T [W_h h_j^{(\ell-1)} \| W_h h_k^{(\ell-1)} \| W_e r_{jk}]\Big)$
    - Compute physical message: $m_{jk}^{(\ell)} = \alpha_{jk}^{(\ell)} \psi(h_j^{(\ell-1)}, h_k^{(\ell-1)}, r_{jk})$
  - **end**
  - Aggregate messages: $M_k^{(\ell)} = \sum_{j \in \mathcal{N}(k)} m_{jk}^{(\ell)}$
  - Update node state: $h_k^{(\ell)} = \text{GRU}(h_k^{(\ell-1)}, M_k^{(\ell)})$
  - Apply residual refinement: $h_k^{(\ell)} = h_k^{(\ell)} + h_k^{(\ell-1)}$
- **end**
- Compute graph-level embedding: $z_G = \text{Readout}\Big(\{h_k^{(L)} : v_k \in V_i\}\Big)$
- **return** $z_G, \{h_k^{(L)}\}$

Algorithm 1: *Cont.*

Initialize CERIG-Net parameters Θ
Split $\mathcal{D}$ into training, validation, and testing sets
foreach *simulation case* $X_i \in \mathcal{D}$ **do**
  $G_i \leftarrow \texttt{BuildGraph}(X_i)$
end
Normalize continuous node features and encode categorical repair strategies
for *epoch* $= 1$ **to** $E_{\max}$ **do**
  Shuffle training graphs $\mathcal{G}_{train}$
  foreach *mini-batch* $\mathcal{B} \subset \mathcal{G}_{train}$ **do**
    foreach *graph* $G_i \in \mathcal{B}$ **do**
      $(z_G, \{h_k\}) \leftarrow \texttt{MessagePassing}(G_i, \Theta)$
      Predict multi-task outputs: $\widehat{\Delta a}, \widehat{\sigma}_{\max}, \widehat{T}_{\text{avg}}, \widehat{D}_{\text{int}}, \widehat{R}_d, \widehat{FE}, \widehat{\Delta N_f}, \widehat{P}(S) \leftarrow \text{Heads}(z_G)$
      Estimate uncertainty: $(\mu, \sigma^2) \leftarrow \text{UncertaintyHead}(z_G)$
      Compute physical heat-flux consistency: $\mathcal{L}_q = ||\widehat{q}_{\text{repair}} - A_E q_{\max}||_2^2$
      Compute energy feasibility consistency: $\mathcal{L}_E = ||\widehat{FE} - \mathbb{I}(E_{\text{available}} \geq E_{\text{repair}})||_2^2$
      Compute durability consistency: $\mathcal{L}_R = ||\widehat{R}_d - \Phi(\widehat{\Delta a}, \widehat{\sigma}_{\max}, \widehat{D}_{\text{int}}, \widehat{FE})||_2^2$
    end
    Compute total multi-task loss:

$$\mathcal{L}_{\text{CERIG}} = \lambda_1 \mathcal{L}_{\Delta a} + \lambda_2 \mathcal{L}_{\sigma} + \lambda_3 \mathcal{L}_T + \lambda_4 \mathcal{L}_D + \lambda_5 \mathcal{L}_{R_d} + \lambda_6 \mathcal{L}_{FE} + \lambda_7 \mathcal{L}_S + \lambda_8 (\mathcal{L}_q + \mathcal{L}_E + \mathcal{L}_R)$$

    Update model parameters: $\Theta \leftarrow \Theta - \eta \nabla_{\Theta} \mathcal{L}_{\text{CERIG}}$
  end
  Validate CERIG-Net on $\mathcal{G}_{val}$
  if *validation loss does not improve for patience window* **then**
    Stop training and restore best parameters Θ^*
    break
  end
end
foreach *test repair scenario* $G_i \in \mathcal{G}_{test}$ **do**
  $(z_G, \{h_k\}) \leftarrow \texttt{MessagePassing}(G_i, \Theta^*)$
  Predict repair responses $\widehat{Y}_i = \{\widehat{\Delta a}, \widehat{\sigma}_{\max}, \widehat{T}_{\text{avg}}, \widehat{D}_{\text{int}}, \widehat{R}_d, \widehat{FE}, \widehat{\Delta N_f}\}$
  foreach *candidate strategy* $s \in \mathcal{S}$ **do**
    Estimate strategy-specific response $\widehat{Y}_i(s)$
    Compute physics-constrained decision score:

$$J_i(s) = \omega_1 \widehat{\Delta a}(s) + \omega_2 \widehat{\sigma}_{\max}(s) + \omega_3 \widehat{D}_{\text{int}}(s) + \omega_4 \widehat{E}_{\text{repair}}(s) + \omega_5 \widehat{R}_{\text{risk}}(s) - \omega_6 \widehat{R}_d(s) - \omega_7 \widehat{\Delta N_f}(s)$$

    if $\widehat{FE}(s) = 0$ **then**
      Apply infeasibility penalty: $J_i(s) \leftarrow J_i(s) + \Omega_E$
    end
  end
  Rank strategies in ascending order of $J_i(s)$
  Select optimal strategy: $S_i^* = \arg\min_{s \in \mathcal{S}} J_i(s)$
end
Evaluate regression performance using R^2, RMSE, and MAE
Evaluate feasibility and strategy classification using accuracy, precision, recall, and F1-score
Evaluate decision quality using strategy-ranking consistency, energy-feasibility agreement, and Pareto dominance
return Θ^*, predicted responses $\widehat{Y}$, ranked strategies $\mathcal{R}$, and optimal decisions S^*

Evaluation Metrics and Mathematical Formulation

The performance of CERIG-Net was evaluated using regression, classification, ranking, uncertainty, and decision-level metrics to ensure that the model accurately predicts simulation-derived pavement responses and selects physically feasible repair strategies. For the regression outputs, including crack growth length Δa, maximum principal stress $\sigma_{\max}$, average repair zone temperature T_{avg}, interface damage D_{int}, repair durability index R_d, and service life gain ΔN_f, the prediction accuracy was assessed using the coefficient of determination R^2, root mean square error (RMSE), mean absolute error (MAE), and mean absolute percentage error (MAPE). These metrics are defined as follows [10]:

$$R^2 = 1 - \frac{\sum_{i=1}^{N}(y_i - \hat{y}_i)^2}{\sum_{i=1}^{N}(y_i - \bar{y})^2} \tag{33}$$

$$RMSE = \sqrt{\frac{1}{N}\sum_{i=1}^{N}(y_i - \hat{y}_i)^2} \tag{34}$$

$$MAE = \frac{1}{N}\sum_{i=1}^{N}|y_i - \hat{y}_i| \tag{35}$$

$$MAPE = \frac{100}{N}\sum_{i=1}^{N}\left|\frac{y_i - \hat{y}_i}{y_i + \epsilon}\right| \tag{36}$$

where y_i is the simulation-derived target value, $\hat{y}_i$ is the CERIG-Net predicted value, $\bar{y}$ is the mean of the observed target values, N is the number of test samples, and ϵ is a small constant added to avoid division by zero.

For the binary energy feasibility prediction task, where the model must determine whether a repair action is feasible under the available PV battery energy condition, classification performance was evaluated using accuracy, precision, recall, F1-score, and specificity. These metrics are formulated as follows [9]:

$$Accuracy = \frac{TP + TN}{TP + TN + FP + FN} \tag{37}$$

$$Precision = \frac{TP}{TP + FP} \tag{38}$$

$$Recall = \frac{TP}{TP + FN} \tag{39}$$

$$F1 = 2 \times \frac{Precision \times Recall}{Precision + Recall} \tag{40}$$

$$Specificity = \frac{TN}{TN + FP} \tag{41}$$

where TP, TN, FP, and FN represent true positive, true negative, false positive, and false negative predictions, respectively. In this study, a true positive case indicates that CERIG-Net correctly identifies an energy-feasible repair scenario, while a false positive case indicates that the model incorrectly recommends a repair as feasible despite insufficient energy availability.

For the repair strategy classification task, the candidate maintenance strategies are defined as follows:

$$\mathcal{S} = \{S_1, S_2, S_3, S_4, S_5\} = \{\text{delay repair}, \text{crack sealing}, \text{localized patch}, \text{thin overlay}, \text{deep repair}\}. \tag{42}$$

The strategy prediction accuracy was evaluated using multi-class accuracy:

$$Accuracy_S = \frac{1}{N}\sum_{i=1}^{N}\mathbb{I}(\hat{S}_i = S_i) \tag{43}$$

where S_i is the simulation-derived optimal strategy, $\hat{S}_i$ is the predicted strategy, and $\mathbb{I}(\cdot)$ is the indicator function.

Because the proposed model ranks multiple candidate repair strategies rather than only assigning one class label, ranking quality was evaluated using top-k accuracy and mean reciprocal rank (MRR). These are expressed as

$$Top\text{-}k = \frac{1}{N}\sum_{i=1}^{N}\mathbb{I}\left(S_i \in \hat{\mathcal{S}}_i^{(k)}\right), \tag{44}$$

$$MRR = \frac{1}{N}\sum_{i=1}^{N}\frac{1}{rank_i}, \tag{45}$$

where $\hat{\mathcal{S}}_i^{(k)}$ is the set of the top-k ranked strategies predicted by CERIG-Net for scenario i and $rank_i$ is the ranking position of the correct repair strategy. A higher MRR indicates that the correct or simulation-consistent repair strategy is placed near the top of the predicted ranking list.

The physics-constrained repair decision score was evaluated to verify whether the selected strategy achieves a balanced trade-off among structural performance, energy feasibility, durability, and service life improvement. The decision score for strategy s is defined as [30]:

$$\begin{aligned} J_i(s) = \omega_1\widehat{\Delta a}_i(s) + \omega_2\widehat{\sigma}_{\max,i}(s) + \omega_3\widehat{D}_{\text{int},i}(s) + \omega_4\widehat{E}_{\text{repair},i}(s) \\ + \omega_5\widehat{R}_{\text{risk},i}(s) - \omega_6\widehat{R}_{d,i}(s) - \omega_7\widehat{\Delta N}_{f,i}(s). \end{aligned} \tag{46}$$

In Equation (46), $J_i(s)$ denotes the composite decision score assigned to candidate repair strategy s for pavement scenario i, the term $\widehat{\Delta a}_i(s)$ denotes the predicted post-repair crack growth response, $\widehat{\sigma}_{\max,i}(s)$ is the predicted maximum principal stress, $\widehat{D}_{\text{int},i}(s)$ represents the predicted repair interface damage, and $\widehat{E}_{\text{repair},i}(s)$ is the predicted energy demand required to execute the repair. Furthermore, $\widehat{R}_{\text{risk},i}(s)$ represents the predicted repair risk indicator, $\widehat{R}_{d,i}(s)$ denotes the predicted repair durability index, and $\widehat{\Delta N}_{f,i}(s)$ represents the predicted service life gain. The hat notation indicates quantities predicted by CERIG-Net for each candidate repair strategy.

The corresponding decision weights were defined as $\omega_1 = 0.25$, $\omega_2 = 0.15$, $\omega_3 = 0.15$, $\omega_4 = 0.15$, $\omega_5 = 0.10$, $\omega_6 = 0.10$, and $\omega_7 = 0.10$, satisfying $\sum_{j=1}^{7}\omega_j = 1$. The largest weight was assigned to crack growth control, as suppression of continued fracture propagation represents the primary structural objective of the maintenance decision. Maximum principal stress, interface damage, and repair energy demand were assigned equal secondary importance, while repair risk, durability, and service life gain were included as complementary decision quality criteria. The positive terms in Equation (46) correspond to quantities to be minimized, whereas durability and service life gain appear with negative signs because they are desirable quantities to be maximized. The weighting coefficients were prescribed as engineering priority coefficients rather than being estimated from the CERIG-Net test results.

The optimal repair strategy is selected as follows:

$$S_i^* = \arg\min_{s\in\mathcal{S}} J_i(s). \tag{47}$$

where $\mathcal{S}$ denotes the complete set of candidate pavement repair strategies and S_i^* is the strategy that produces the minimum decision score for scenario i. To ensure that an energy-infeasible strategy is not selected, an infeasibility penalty is added when the predicted feasibility indicator is zero:

$$J_i'(s) = J_i(s) + \Omega_E\left[1 - \widehat{FE}_i(s)\right] \tag{48}$$

where Ω_E is a large penalty coefficient and $\widehat{FE}_i(s) \in \{0,1\}$ is the predicted feasibility state.

The agreement between the predicted optimal strategy and the simulation-derived optimal strategy was evaluated using decision agreement [31]:

$$DA = \frac{1}{N}\sum_{i=1}^{N}\mathbb{I}(\hat{S}_i^* = S_i^*). \tag{49}$$

In addition, energy feasibility agreement was computed as

$$EFA = \frac{1}{N}\sum_{i=1}^{N}\mathbb{I}\left(\widehat{FE}_i = FE_i\right), \tag{50}$$

where FE_i is the simulation-derived feasibility label and $\widehat{FE}_i$ is the predicted feasibility state.

For multi-objective repair evaluation, the Pareto dominance condition was used to determine whether a predicted repair strategy provides a non-dominated balance between crack control, repair energy, durability, and service life gain. A strategy s_a dominates another strategy s_b if [32]

$$s_a \prec s_b \quad \text{if} \quad f_m(s_a) \le f_m(s_b)\ \forall m \quad \text{and} \quad \exists m : f_m(s_a) < f_m(s_b), \tag{51}$$

where $f_m(\cdot)$ represents the m-th objective function. In this study, the objective vector is defined as

$$\mathbf{f}(s) = \left[\Delta a(s), \sigma_{\max}(s), D_{\text{int}}(s), E_{\text{repair}}(s), -R_d(s), -\Delta N_f(s)\right]. \tag{52}$$

The negative signs for R_d and ΔN_f are used because durability and service life gain are maximized, while the other objectives are minimized.

Because CERIG-Net includes an uncertainty branch, uncertainty calibration was evaluated using the negative log-likelihood (NLL) and prediction interval coverage probability (PICP). Assuming a Gaussian predictive distribution, the NLL is

$$NLL = \frac{1}{2N}\sum_{i=1}^{N}\left[\log(\hat{\sigma}_i^2) + \frac{(y_i - \hat{\mu}_i)^2}{\hat{\sigma}_i^2}\right], \tag{53}$$

where $\hat{\mu}_i$ and $\hat{\sigma}_i^2$ are the predicted mean and variance, respectively. The PICP is defined as

$$PICP = \frac{1}{N}\sum_{i=1}^{N}\mathbb{I}(y_i \in [\hat{\mu}_i - z_{\alpha/2}\hat{\sigma}_i,\ \hat{\mu}_i + z_{\alpha/2}\hat{\sigma}_i]), \tag{54}$$

where $z_{\alpha/2}$ is the standard normal critical value for the selected confidence level. These uncertainty metrics evaluate whether CERIG-Net provides reliable confidence estimates for safety-sensitive pavement repair decisions.

4. Discussion, Results, and Comparison

Table 5 provides the first quantitative evidence that the proposed energy-constrained pavement maintenance strategy changes the crack evolution trajectory rather than merely delaying the visual appearance of damage. Before repair activation, the no-repair and repaired cases follow the same deterioration path, where the crack length increases from 35.0 mm at the initial state to 39.8 mm at 20,000 cycles and then to 48.1 mm at the repair trigger point of 40,000 cycles, while the XFEM damage index rises from 0.08 to 0.23 and the maximum principal stress increases from 1.42 MPa to 2.37 MPa. This confirms that the pavement enters the intervention stage after a physically meaningful accumulation of crack damage, not at an arbitrary point. Once the thermal repair is activated at 40,000$^+$ cycles, the effective crack length decreases from 48.1 mm to 35.8 mm, the repaired damage index falls from 0.23 to 0.11, and the maximum principal stress decreases from 2.37 MPa to 1.62 MPa, producing immediate reductions of 25.6% in crack growth and 31.6% in stress. The later loading stages show that the repair does not unrealistically stop crack growth; instead, it suppresses the crack driving response and keeps the repaired trajectory below the unrepaired path. At 100,000 cycles, the no-repair crack reaches 94.7 mm, exceeding the 75 mm critical threshold, whereas the repaired crack remains at 53.8 mm, with a positive threshold margin of +21.2 mm. At the same final stage, the XFEM damage index is reduced from 0.94 to 0.51 and the maximum principal stress is reduced from 3.85 MPa to 2.22 MPa, corresponding to final improvements of 43.2% in crack growth control and 42.3% in stress reduction. These results establish the structural foundation for the following energy and repair strategy tables: the repair is mechanically effective because it lowers crack growth, damage accumulation, and stress concentration, but its full interpretation requires the subsequent thermal conditioning, interface bonding, energy feasibility, and CERIG-Net ranking results to explain why a specific repair strategy can remain durable and feasible under limited work zone energy.

To further assess the physical representativeness of the XFEM crack evolution response, the predicted deterioration behavior was compared with independent laboratory-based observations and experimentally validated XFEM studies of asphalt pavement cracking. Li et al. [22] investigated reflective crack propagation in asphalt overlays under repeated wheel loading and reported close agreement between experimentally observed cracking and three-dimensional XFEM predictions, with crack propagation errors remaining below approximately 8%. Similarly, Alrashydah and Papagiannakis [4] evaluated XFEM crack propagation using the Texas Overlay Test and demonstrated that the numerical crack growth response reproduced the experimentally observed fatigue and fracture behavior of asphalt concrete. Islam et al. [23] further validated an XFEM-based asphalt overlay model using indirect and direct tensile laboratory measurements, confirming the capability of the method to represent crack initiation and subsequent propagation from pre-existing pavement cracks. In addition, Wu et al. [24] combined semi-circular bending fracture tests with XFEM simulations and showed that asphalt reflective cracking develops through fracture energy-controlled mixed-mode propagation, with crack growth accelerating as loading severity and duration increase. These experimentally supported observations are consistent with the response obtained in Table 6, where crack length, XFEM damage, and maximum principal stress increase progressively with accumulated loading while the maintenance intervention suppresses subsequent crack propagation. Because the published studies employ different specimen geometries, asphalt mixtures, temperatures, loading protocols, and boundary conditions, the comparison is not treated as a direct point-by-point calibration of absolute crack length; however, it does provide independent experimental support for the crack initiation, progressive damage, mixed-mode fracture, and cyclic crack growth mechanisms represented by the adopted XFEM formulation. The corresponding comparison is summarized in Table 7.

Table 5. Compact experimental configuration setup for the simulation-driven CERIG-Net pavement crack maintenance framework.

Experiment Block	Finite-Element/XFEM Simulation Configuration					Energy-Constrained Repair Configuration				Dataset and CERIG-Net Configuration				Training and Evaluation Setup				
	FE Domain	Layer System	Crack Model	Mesh Setting	Load/ BCs	Heat Flux	Energy State	Thermal Window	Repair Interface	Feature Groups	Graph Nodes	Learning Core	AI Targets	Split	Training Params.	Loss Terms	Decision Rule	Metrics
A. Finite-element pavement simulation and XFEM crack evolution configuration																		
Pavement FE model	3D	6 layers	XFEM	C3D8T/C3D8	Fixed + lateral	$q_{\max} = 18$	SOC = 60%	$t_H = 15$ min	Cohesive	8 groups	7 nodes	Encoder	σ, u, T	70/30	Seed = 42	MSE/MAE	ODB output	R^2, RMSE
Layer geometry	1.20×0.90 m	1.67 m depth	Surface crack	25–50 mm	$u_z = 0$ bottom	$q = A_E q_{\max}$	PV = 0.65	$T_0 = 28\,^\circ$C	Bonded	6 thicknesses	Material node	Node emb.	Layer resp.	70/30	Norm. = min–max	Geom. loss	Layer map	MAE, MAPE
Layer thickness	3D block	50/70/100/ 200/250/1000 mm	$a_0 = 35$–75 mm	5–50 mm	Side restraint	8–18 kW/m^2	SOC = 20–100%	55–85°C	$B_q = 0.4$–1.0	Geometry	Material/ response	GNN encoder	u_z, σ	70/30	Batch = 32–64	MSE	FE response	RMSE
Material assignment	Elastic-thermal	$E = 80$–4800 MPa	$G_I = 350$–650	Layer mesh	$\nu = 0.33$–0.45	Thermal input	E_{avail}	$k = 1.10$–1.80	$K_n = 1$–5×10^6	E, ν, ρ, k, c_p	Material node	Encoder input	$\sigma_{\max}, T$	70/30	LR = 10^{-3}	MSE/MAE	Sensitivity	R^2, RMSE
XFEM crack setup	Surface layer	50 mm asphalt	$d_0 = 15$–45 mm	5–8 mm	$p = 550$–800 kPa	0 kW/m^2	Pre-repair	No heating	Initial bond	a_0, d_0, θ_c, D_c	Crack node	Graph encoder	$\Delta a, D_c$	70/30	Epoch = 200	Crack loss	Crack update	MAE, RMSE
Crack propagation	Damage zone	Aged asphalt	$\theta_c = 0$–25°	XFEM refined	$N = 10^3$–10^5	Inactive	N/A state	Service stage	Traction law	$\sigma_n^0, \tau_s^0, G_I, G_{II}$	Crack edge	MP layers	STATUSXFEM	70/30	Patience = 20	Damage loss	Crack state	Prop. error
Repair-zone FE model	Local repair	300–600 mm	Post-crack	6–10 mm	80–120 kN	8–18 kW/m^2	FE = 0/1	5–25 min	$D_{int} = 0$–1	Repair size	Interface node	Fusion	D_{int}, τ_{int}	70/30	Dropout = 0.2	Interface loss	Repair active	Int. error
B. Energy-constrained repair operation and generated simulation dataset configuration																		
Energy-limited heating	Thermal step	Repair zone	XFEM case	Thermal mesh	Film BC	8–18 kW/m^2	20–100%	5–25 min	$B_q = 0.4$–1.0	Energy/thermal	Energy node	E-T path	T_{avg}, FE	70/30	LR = 10^{-3}	q loss	FE label	Acc., F1
PV-battery condition	Work zone	Surface repair	Thermal-XFEM	Coupled mesh	$h_c = 8$–15	$A_E = 0$–1	PV = 0.20–0.95	$T_0 = 20$–35	$K_s = 0.5$–3×10^6	SOC, PV, A_E	Energy/thermal	Fusion	q, B_q	70/30	Dropout = 0.1–0.3	Energy const.	$FE \in \{0, 1\}$	EFA
Thermal conditioning	Heat repair	Target zone	Post-crack	C3D8T	Convection	$q = A_E q_{\max}$	SOC/PV	$T_{tar} = 55$–85	Interface recovery	q, t_H, T_{avg}	Thermal node	Message pass.	T field	70/30	Hidden = 64–128	Thermal loss	$T \geq 65$°C	RMSE, MAE
Generated dataset	ODB source	FE outputs	XFEM labels	History data	Pre/post state	Energy labels	FE = 0/1	Thermal field	Interface output	8 feature sets	7 node types	Hetero-graph	$\Delta a, \sigma, T, D_{int}$	70/30	Standardization	Multi-task	S^*	R^2, F1
Repair-strategy set	Actions	5 strategies	Strategy crack	5 cases	Post-load	Energy constraint	Feasible state	5–25 min	B_q state	Strategy code	Strategy node	Ranking head	S_1–S_5	70/30	One-hot	CE/ranking	S1-S5	Top-k, MRR
C. CERIG-Net architecture, training configuration, and model-evaluation protocol																		
CERIG-Net graph	Scenario graph	Layer vector	Crack node	Adjacency	Load vector	Energy vector	SOC/PV	Thermal vector	Interface vector	8 groups	7 nodes	Hetero encoder	7 heads	70/30	Hidden = 64–128	Graph loss	$J(s)$	All metrics
Graph reasoning core	FE graph	Layer emb.	Crack emb.	Edge attr.	Load emb.	Energy emb.	FE edge	Thermal emb.	Interface emb.	Node/edge emb.	7 nodes	3–5 MP; 4–8 heads	z_G	70/30	Dropout = 0.2	Phys. loss	Residual	Val. loss
Multi-task prediction	Graph output	Layer resp.	Crack output	Resp. mesh	Load resp.	Energy resp.	FE output	Thermal resp.	Interface resp.	Sim. outputs	Response node	Pred. heads	$\Delta a, \sigma_{\max}, T_{avg}, D_{int}, R_d, \Delta N_f$	Test set	AdamW	MSE + MAE	Prediction	R^2, RMSE, MAE
Feasibility/ uncertainty	Energy graph	Thermal layer	Risk state	Unc. graph	Repair load	Energy feas.	FE label	Thermal adequacy	Bond conf.	Energy targets	Energy node	Unc. branch	FE, μ, σ^2	Test set	Batch = 32–64	BCE + NLL	Ω_E	Acc., F1, NLL, PICP
Strategy optimization	Decision graph	Repair layer	Crack score	Strategy edges	Post-load	Energy demand	Feasible repair	Repair window	Durability	Decision vars.	Strategy node	Ranking layer	$S^*, R_d, \Delta N_f$	Test set	Epoch = 200	Rank + constraint	$\arg\min J(s)$	Top-k, MRR, DA
Decision evaluation	Graph output	Layer contrib.	XFEM contrib.	Output emb.	Repair resp.	Energy agree.	FE = 0/1	Thermal consistency	Repair durability	Pred./sim.	Decision node	Readout	Optimal decision	Indep. test	Seed = 42	CERIG loss	Pareto	DA, EFA, Pareto

https://doi.org/10.3390/math14173149

Table 6. Detailed XFEM crack growth, damage index, and stress response evolution before and after energy-constrained pavement maintenance.

Loading Stage	Crack Length Response			XFEM Damage Response			Stress Displacement Response			Repair Effect Indicators			Status	
	N Cycles	No Repair Δa (mm)	Repaired Δa (mm)	No Repair D_c	Repaired D_c	Damage Drop (%)	No Repair $\sigma_{\max}$ (MPa)	Repaired $\sigma_{\max}$ (MPa)	u_z After Repair (mm)	$R_{\Delta a}$ (%)	R_σ (%)	Threshold Margin (mm)	XFEM State	Repair Condition
Initial state	0	35.0	35.0	0.08	0.08	0.0	1.42	1.42	0.31	0.0	0.0	+40.0	Initial crack	No repair
Early loading	20,000	39.8	39.8	0.15	0.15	0.0	1.87	1.87	0.38	0.0	0.0	+35.2	Stable growth	No repair
Repair trigger	40,000	48.1	48.1	0.23	0.23	0.0	2.37	2.37	0.47	0.0	0.0	+26.9	Propagating	Before activation
Immediate post-repair	40,000+	48.1	35.8	0.23	0.11	52.2	2.37	1.62	0.35	25.6	31.6	+39.2	Repaired crack	Thermal repair applied
Mid post-repair	60,000	61.3	38.7	0.41	0.18	56.1	2.84	1.79	0.41	36.9	37.0	+36.3	Suppressed growth	Interface stable
Late post-repair	80,000	76.6	45.0	0.66	0.31	53.0	3.30	2.02	0.49	41.3	38.8	+30.0	Below threshold	Durability retained
Final loading	100,000	94.7	53.8	0.94	0.51	45.7	3.85	2.22	0.58	43.2	42.3	+21.2	Post-repair growth	Service life extended

Table 7. Comparison of the XFEM crack evolution response with published laboratory observations of asphalt pavement cracking.

Reference	Experimental/Field Condition	Reported Crack Response	Present XFEM Response	Agreement
Li et al. (2021) [22]	Laboratory asphalt overlay specimens subjected to repeated wheel loading; crack propagation measured and compared with 2D and 3D XFEM.	Cracks propagated from approximately 3 to 30 mm. For the 3D model, initial/final cracking errors were 4.7%/1.7% for crack pouring and 7.8%/5.7% for crack paste treatment; all errors were below 8%.	Crack length increases progressively from 35.0 to 48.1 mm before intervention and reaches 94.7 mm at 100,000 cycles without repair; repair limits the final crack length to 53.8 mm.	Strong agreement in progressive cyclic crack growth and post-treatment suppression; published 3D XFEM error $<$ 8%.
Alrashydah and Papagiannakis (2023) [4]	Texas Overlay Test under cyclic opening displacement, with experimental crack growth measurements used for XFEM assessment.	XFEM crack propagation curves closely followed the experimental response and reproduced the measured fatigue life and fracture toughness behavior more closely than the corresponding analytical solution.	The model predicts continuous damage accumulation under repeated loading, with crack length increasing to 94.7 mm in the unrepaired state and remaining substantially lower after maintenance.	Good trend-level agreement for cyclic fatigue propagation and progressive crack extension; supports the adopted XFEM crack growth formulation.
Islam et al. (2017) [23]	Indirect and direct tensile laboratory tests on asphalt specimens combined with an XFEM model of an HMA overlay subjected to wheel loading.	Laboratory tensile responses were used to validate crack initiation, traction–separation behavior, and crack evolution before applying the validated model to pavement overlays with pre-existing cracks.	The aged asphalt surface contains an initial XFEM crack and exhibits progressive crack extension, increasing damage, and increasing principal stress under repeated wheel loading.	Consistent physical response for crack initiation and propagation from a pre-existing asphalt crack under traffic loading.
Wu et al. (2023) [24]	Semi-circular bending fracture tests on asphalt specimens followed by XFEM simulation of reflective cracking in a typical pavement structure.	Laboratory-derived fracture energy reproduced the SCB fracture response. Pavement simulations identified mixed Mode-I/Mode-II reflective cracking, with Mode I dominant; overloading and prolonged loading accelerated propagation.	The present formulation uses mixed-mode fracture-energy criteria and predicts accumulated crack growth and damage under repeated wheel loading rather than instantaneous failure.	Strong mechanistic agreement in fracture energy-controlled, mixed-mode, and load-dependent crack propagation.

Figure 7 provides a detailed mechanistic interpretation of how energy-constrained thermal conditioning governs the structural and interface performance of the repaired pavement system. Subfigure (a) shows that the maximum principal stress decreases as the average repair zone temperature increases, indicating that stronger thermal conditioning softens and stabilizes the repaired region, reduces crack tip stress concentration, and improves the post-repair load transfer condition. Subfigure (b) extends this interpretation to the repair interface, where the interface stress τ_{int} declines with increasing T_{avg}, confirming that insufficient heating under the low-energy case keeps the interface mechanically stressed, while the high-energy case produces a more relaxed and stable bonding condition. Subfigure (c) directly links this thermal improvement to bonding quality and interface damage: as T_{avg} approaches and exceeds the bonding threshold of $T_{\text{th}} = 65\ ^{\circ}\text{C}$, the bonding quality index B_q increases while the interface damage D_{int} decreases, demonstrating that the repair is controlled not by temperature alone but by the combined thermal bonding response. Subfigure (d) synthesizes these coupled effects in the $T_{\text{avg}} - B_q$ space, where the transition from weak thermal bonding to a low-stress/high-efficiency repair region shows that the most favorable repair condition occurs only when sufficient temperature and bonding quality are achieved together. Subfigure (e) confirms the same trend from a durability perspective as the repair durability index R_d rises sharply from the low-energy condition to the high-energy condition, proving that energy-supported heating improves long-term repair performance through reduced stress and stronger interface integrity. Finally, subfigure (f) connects the entire mechanism to crack control performance, showing that crack growth reduction $R_{\Delta a}$ increases with repair zone temperature, especially beyond the bonding threshold. Overall, the figure links the energy-constrained repair concept to the generated simulation dataset described in the study, where temperature field, interface stress, bonding quality, interface damage, repair durability, and crack growth reduction are extracted as coupled outputs for AI-based repair strategy optimization. This figure acts as a bridge between the thermal conditioning stage and the CERIG-Net decision stage, demonstrating why the model must evaluate repair strategies using coupled structural, thermal, interface, and energy feasibility indicators rather than crack growth alone.

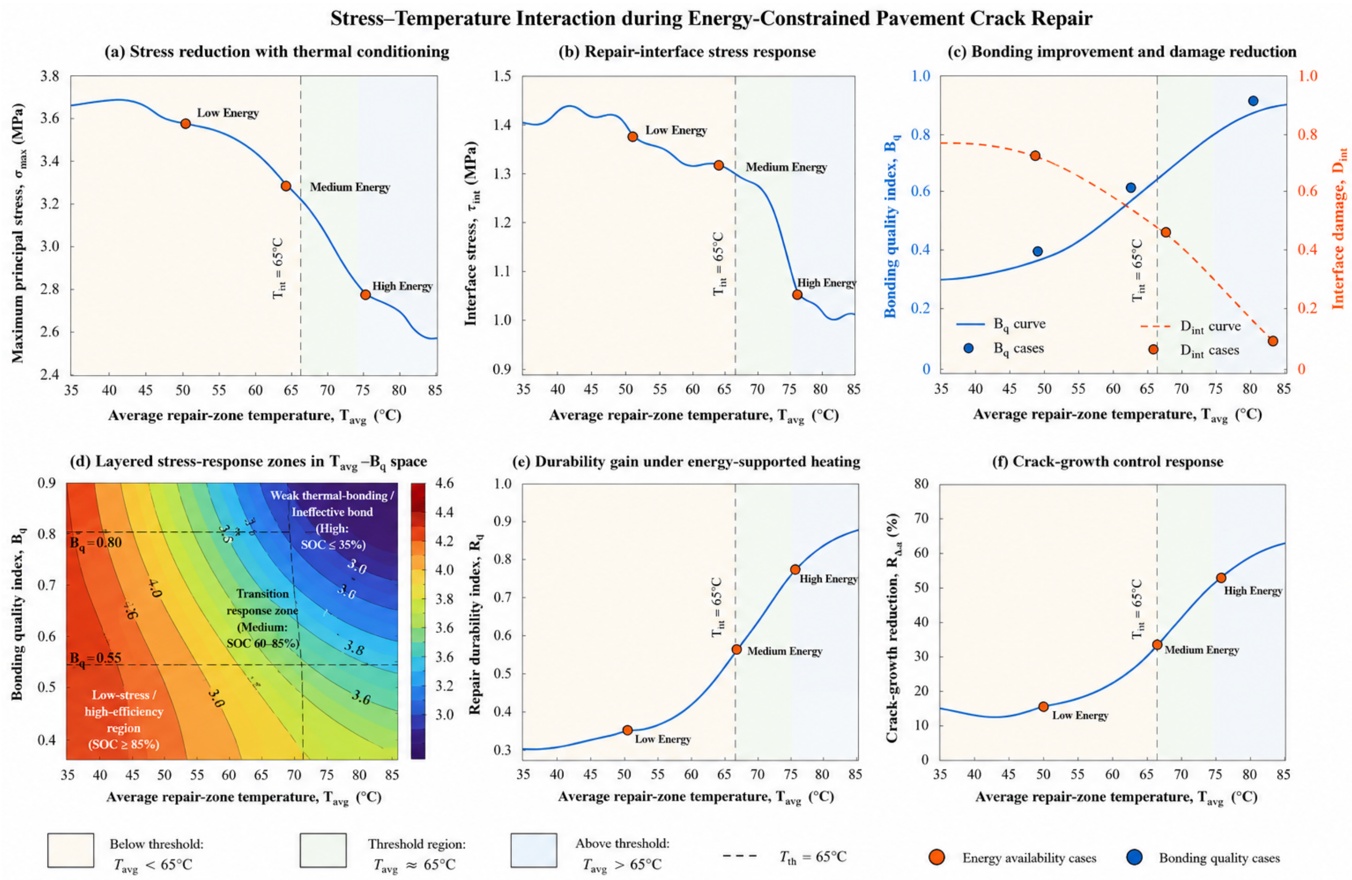

Figure 7. Spatial Evolution of XFEM damage index during energy-constrained pavement crack repair.

Figure 8 illustrates the accumulated XFEM damage field during energy-constrained pavement crack repair, showing how damage develops spatially before repair activation and how the repair zone controls subsequent crack evolution. In subfigures (a) and (b), corresponding to $N = 10k$ and $N = 25k$ loading cycles, the accumulated damage remains concentrated along the initial crack paths, where the high-intensity red and yellow bands indicate localized XFEM damage accumulation and the surrounding dark blue field shows that the damage is still spatially confined. At $N = 40k$ cycles in subfigure (c), the repair intervention is activated; the dashed repair zone boundary encloses the dominant damaged region, confirming that the maintenance action is applied at the stage where crack propagation has become sufficiently developed but has not yet spread across the entire pavement surface. After repair activation, subfigures (d), (e), and (f) show the post-repair accumulated damage at $N = 55k$, $75k$, and $100k$ cycles, respectively. The damage field continues to evolve, but its growth becomes more controlled within and around the repair zone. This agrees with the crack growth reduction trend reported earlier in the manuscript, with the repaired crack trajectory remaining below the no-repair response after maintenance activation. The isolated high-damage spots near the upper region of the field indicate residual stress concentration and local crack driving effects that remain after repair, showing that the proposed strategy produces realistic damage suppression. This figure complements the previous crack growth and XFEM damage index curve by providing spatial evidence of how accumulated damage progresses across the pavement domain while also supporting the logic underlying the generated dataset in Section 3.3, in which XFEM status, crack growth, interface damage, repair durability, and energy feasibility are extracted as coupled simulation outputs for AI-based repair strategy optimization. In this way, the figure demonstrates that the AI model is trained on spatially meaningful damage patterns rather than only simplified scalar crack length values, thereby connecting the finite-element/XFEM simulation results to the CERIG-Net learning stage.

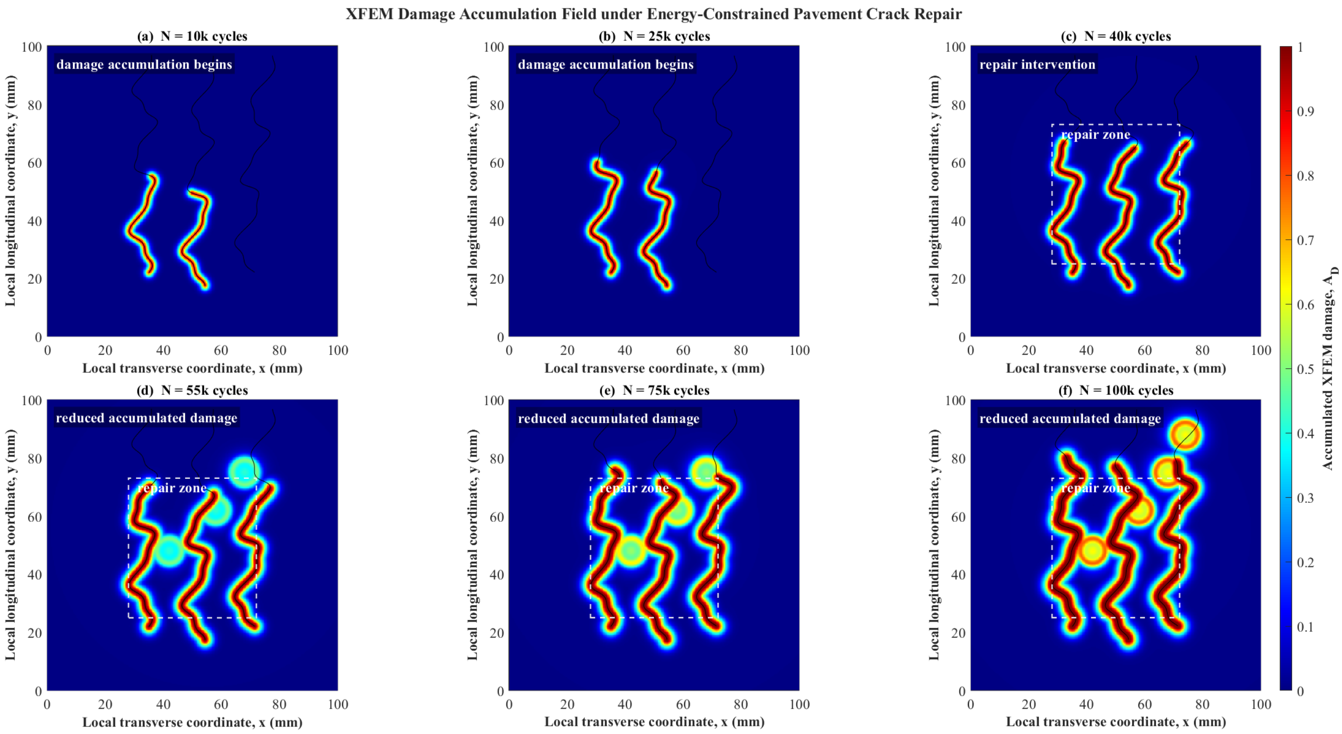

Figure 8. Coupled stress–temperature interaction, interface bonding, and crack control response during energy-constrained pavement repair.

Figure 9 presents the spatial evolution of the XFEM damage index during energy-constrained pavement crack repair, providing a field-based explanation of how damage initiates, propagates and becomes partially controlled after maintenance activation. In subfigures (a) and (b), at $N = 10k$ and $N = 25k$ loading cycles, the damage remains concentrated along the early crack paths; the red and yellow bands indicate high localized XFEM damage, while the surrounding dark blue region remains almost undamaged. This confirms that before repair, pavement deterioration is still governed by localized crack tip damage rather than widespread surface failure. At $N = 40k$ cycles in subfigure (c), the repair intervention is activated and the dashed repair zone boundary encloses the main damaged region, showing that maintenance is introduced at the stage where crack propagation has become significant but is still spatially manageable. After repair activation, subfigures (d), (e), and (f) show controlled post-repair growth at $N = 55k$, $75k$, and $100k$ cycles. The damage field continues to evolve, which is physically realistic because repair does not fully remove fracture activity; however, the dominant damage remains concentrated within and near the repair zone rather than spreading freely across the pavement domain. The isolated high-damage regions near the upper part of the field indicate residual stress concentration and possible secondary crack driving zones under repeated loading, while the repair-zone boundary demonstrates how the maintenance intervention confines and delays damage expansion. This spatial behavior is consistent with the manuscript's reported crack growth reduction after maintenance, where the repaired response remains below the unrepaired trajectory and the final crack length is reduced from approximately 94.7 mm to 53.8 mm. Overall, the figure strengthens the results by showing that the proposed energy-constrained repair strategy does not unrealistically eliminate XFEM damage, but suppresses and localizes its accumulation, supporting the generated dataset logic in which XFEM status, crack growth, interface damage, repair durability, and energy feasibility are extracted as simulation-derived variables for repair strategy optimization using CERIG-Net.

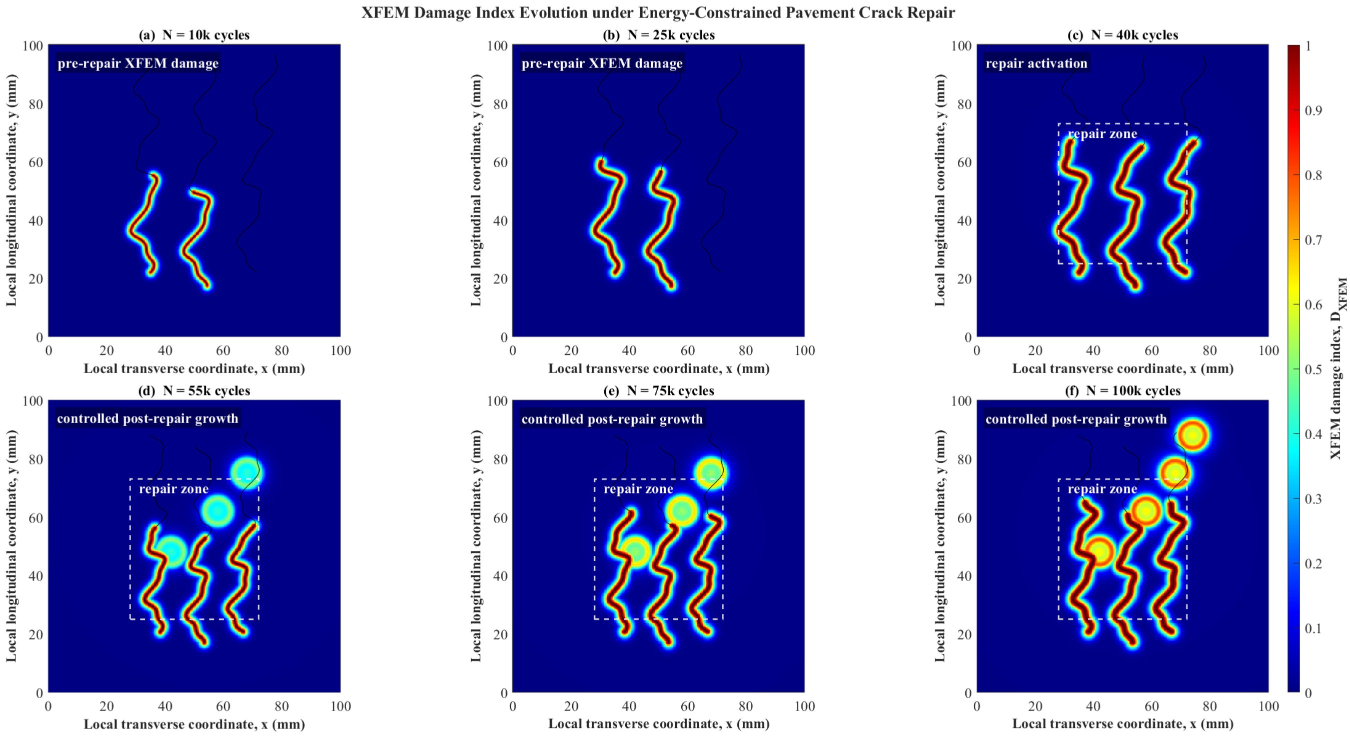

Figure 9. Accumulated XFEM damage field and repair zone control under energy-constrained pavement crack maintenance.

Table 8 explains why the repaired pavement response depends strongly on the available PV battery energy during thermal conditioning. The low-energy case, with $SOC_0 = 35\%$, $PV = 0.35$, and $E_{\text{avail}} = 2.94$ kWh/m^2, produces only $A_E^{peak} = 0.64$, an average heat flux of 8.3 kW/m^2, and an average repair zone temperature of 51.3 °C, which remains 13.7 °C below the 65 °C bonding threshold. Consequently, the bonding quality is weak ($B_q = 0.41$), the interface damage remains relatively high ($D_{\text{int}} = 0.42$), and the repair is classified as thermally limited with $FE = 0$. Increasing the energy state to the medium case ($SOC_0 = 60\%$, $PV = 0.65$) raises the available energy to 4.84 kWh/m^2, increases the peak heat flux amplitude to 0.89, and improves T_{avg} to 63.2 °C, which is only 1.8 °C below the bonding threshold. This produces a clear improvement in bonding quality ($B_q = 0.63$), reduces interface damage to 0.27, and brings the repair feasibility near the threshold. The high-energy case provides the strongest 15-min response, where $SOC_0 = 85\%$, $PV = 0.90$, and $E_{\text{avail}} = 6.38$ kWh/m^2 allow $A_E^{peak} = 0.99$, $q_{avg} = 14.7$ kW/m^2, and $T_{avg} = 75.1$ °C, exceeding the bonding threshold by 10.1 °C; as a result, the bonding quality rises to 0.91, interface damage falls to 0.12, and the repair state becomes strong thermal bonding.

The extended-heating cases further confirm that repair duration alone is not sufficient if energy availability is low: extending the low-energy case to 25 min increases T_{avg} only to 57.3 °C, still below the threshold and infeasible, whereas medium and high extended heating achieve 68.6 °C and 79.5 °C, respectively, with improved bonding and reduced interface damage. Therefore, this table connects directly to the previous crack growth table by showing that the observed reductions in crack growth, XFEM damage, and stress response are physically supported by adequate thermal conditioning, interface bonding, and energy feasibility. It also supports the logic of the following repair strategy comparison, since the optimal maintenance action cannot be selected only from structural recovery and must also satisfy the coupled thermal energy condition that controls bonding quality and long-term durability.

The outputs of the structural, thermal energy, interface, and durability models are combined in a single table for the five candidate pavement maintenance strategies in order to provide a comparative assessment of the output from each of the other models along with a final decision on the pavement repair strategy based on the model outputs. Table 9 is the main table that ties together the results of the previous crack growth and thermal conditioning models to reach the final decision on which repair strategy to take based on the model outputs. The maximum principal stress is still high, at 3.85 MPa; together with the high interface damage of $D_{\text{int}} = 0.88$ and low durability index of $R_d = 0.18$, this leads to the worst decision score of $J(s) = 0.814$, and a ranking of 5 for the delay repair case $S0$. Crack sealing $S1$ is also a good solution, with 23.4% reducing crack growth and 21.0% reducing stress, but has a limited heat flux response $(A_E^{peak} = 0.64, q_{avg} = 8.3\ \text{kW/m}^2)$, moderate temperature (57.8 °C), and weak bonding quality $(B_q = 0.50)$; thus, it is a low-ranking solution, with the interface damage remaining relatively high at 0.41. The decision score of localized patching $S2$ is 0.374, with a better repair response, yielding a reduction in crack growth of 61.7 mm, a reduction in stress to 2.55 MPa, an increase in B_q to 0.71, and an improvement in durability to 0.72. Thin overlay (S3) appears to be the best solution, as it offers a high level of mechanical recovery and energy feasibility; final (required) crack growth is reduced to 53.8 mm, crack growth reduction is 43.2%, the maximum stress is reduced to 2.22 MPa, thermal conditioning is increased to 73.4 °C, bonding quality is improved to 0.87, interface damage is reduced to 0.19, durability is improved to 0.86, and the gain in service life is increased to 6.7 years, with the required repair energy being moderate at 4.84 kWh/m^2. A higher decision score is achieved because the energy demand of 7.24 kWh/m^2 is much greater for deep repair $S4$ than for the other three, although its purely structural performance is the best, with the lowest crack length (49.7 mm), highest crack growth reduction (47.5%), lowest stress (2.04 MPa), and highest durability (0.89). It is important to note that this table indicates that chosen the maintenance strategy should not just be the strategy with the highest crack suppression factor; rather, it is the strategy that provides optimal crack control, stress reduction, thermal adequacy, interface bonding, durability of the repair, and extension of service life while also reducing energy demand.

The superior overall performance of the thin overlay strategy can be attributed to the balance it provides between structural reinforcement, crack bridging, thermal adequacy, interface recovery, and energy demand. Compared with crack sealing, thin overlay treats a substantially larger portion of the deteriorated surface layer, providing greater structural continuity across the cracked region rather than acting mainly as a localized crack-filling intervention. This broader treatment redistributes the wheel-induced stress field over a wider area, reduces the stress concentration surrounding the existing crack, and provides greater resistance to continued XFEM crack propagation. This behavior is reflected in the reduction of the final crack length to 53.8 mm and the maximum principal stress to 2.22 MPa, compared with 72.5 mm and 3.04 MPa for crack sealing. Localized patching provides greater structural recovery than sealing, but its more confined repair geometry produces a stronger transition between repaired and existing pavement regions, and consequently a less favorable combination of bonding, interface damage, and stress redistribution than the overlay treatment. Accordingly, localized patching achieves $B_q = 0.71$, $D_{\text{int}} = 0.28$, and $R_d = 0.72$, whereas thin overlay improves these values to $B_q = 0.87$, $D_{\text{int}} = 0.19$, and $R_d = 0.86$, respectively. Thin overlay also achieves a repair zone temperature of 73.4 °C while using a moderate repair energy demand of 4.84 kWh/m^2, providing sufficient thermal conditioning for interface bonding without requiring the substantially greater energy input associated with deep repair.

Deep repair produces the strongest purely structural response because it replaces or rehabilitates a greater depth of the damaged pavement, resulting in the lowest final crack length of 49.7 mm, lowest maximum stress of 2.04 MPa, and highest durability index of 0.89. However, these additional structural gains over the thin overlay approach are comparatively small relative to the increase in required repair energy from 4.84 to 7.24 kWh/m^2. Deep repair also requires a higher thermal conditioning state, with $A_E = 0.99$, and an average repair temperature of 78.5 °C. Consequently, its improvement in crack growth reduction from 43.2% to 47.5% and service life gain from 6.7 to 7.4 years is accompanied by a substantially greater energy requirement. Within the coupled structural–thermal–energy decision framework, this trade-off increases the decision score of deep repair to $J(s) = 0.239$, compared with $J(s) = 0.216$ for the thin overlay strategy. While thin overlay is not identified as being universally superior to deeper rehabilitation, under the investigated crack condition and PV battery constraints it provides the most favorable compromise between structural recovery, interface integrity, repair durability, service life extension, and energy-efficient execution.

Table 10 extends he previous comparison of the strategies to the scenario level in order to provide an understanding of the behavior of the proposed repair framework for varying crack severities, energy states, repair actions and risk conditions. The results clearly show that the response to crack repair is significantly improved when the amount of available energy is increased from $SOC = 35\%$ and $PV = 0.35$ to $SOC = 85\%$ and $PV = 0.90$, as the first crack group (C01–C03) is seeded with a smaller and more moderate crack severity. The crack length for the case of crack sealing is 70.8 mm compared, to 51.7 mm for the thin overlay case; the maximum stress for crack sealing is 3.03 MPa, whereas for thin overlay it is 2.12 MPa; similarly, the durability index for crack sealing is 0.54, while for thin overlay it is 0.88. In C04–C06, similar trends can be observed for the medium severity condition. With crack sealing, an infeasible repair state occurs for low energy (FE = 0), high risk, and a final crack length of 76.1 mm, while the high-energy then overlay case leads to a lower crack length of 53.8 mm and lower stress of 2.22 MPa with low risk. In more severe crack states, C07–C09 and C10–C12 show how treatment depth and the energy available to the repair process affect the choice of repair. With $a_0 = 65$ mm and $D_c = 0.36$, a low-energy patch is still not feasible and brings high risk (with $\Delta a = 82.4$ mm, $\sigma = 2.19$ MPa and $D = 0.90$). The high-energy deep repair approach shows a better response, with $\Delta a = 58.0$ mm, $\sigma_{\max} = 2.35$ MPa, $R_d = 0.88$, and low risk compared to the low-energy patch approach, which gives $\Delta a = 91.5$ mm, $\sigma_{\max} = 3.90$ MPa, $R_d = 0.37$, and a very high risk classification. Therefore, this table establishes the relationship between the previous thermal and strategy results at a finer granular level, indicating that it is not possible to generalize the repair decision from only one scenario because of its reliance on the combination of different factors involved: crack severity, bonding quality, available PV battery energy, and selected intervention types. Additionally, the results reinforce the viability of CERIG-Net, since the model must be able to learn relationships that are inherently nonlinear and dependent on each scenario in order to identify when sealing, patching, deep repair, or overlay is the most logical and viable maintenance option.

Table 8. Expanded energy-constrained thermal repair results under low, medium, and high PV battery availability.

Energy Case	PV Battery Repair Energy Input				Heat Flux Response			Temperature Response			Interface and Feasibility Response			Repair State
	SOC_0 (%)	PV Index	t_H (min)	E_{avail} (kWh/m²)	A_E^{peak}	q_{peak} (kW/m²)	q_{avg} (kW/m²)	T_{avg} (°C)	T_{max} (°C)	T Margin vs. 65 °C	B_q	D_{int}	FE	
Low	35	0.35	15	2.94	0.64	11.6	8.3	51.3	58.5	−13.7	0.41	0.42	0	Thermally limited
Medium	60	0.65	15	4.84	0.89	16.1	12.0	63.2	70.5	−1.8	0.63	0.27	1	Near-threshold feasible
High	85	0.90	15	6.38	0.99	17.8	14.7	75.1	82.8	+10.1	0.91	0.12	1	Strong thermal bonding
Low + extended heating	35	0.35	25	4.08	0.64	11.6	7.1	57.3	64.1	−7.7	0.49	0.36	0	Duration insufficient
Medium + extended heating	60	0.65	25	6.22	0.88	15.9	10.4	68.6	76.4	+3.6	0.76	0.22	1	Feasible improved bonding
High + extended heating	85	0.90	25	8.46	0.99	17.8	12.8	79.5	87.6	+14.5	0.94	0.10	1	High-confidence repair

Table 9. Full comparative repair strategy results under XFEM crack evolution, energy-constrained thermal conditioning, and post-repair loading.

Strategy	Structural Response				Thermal Energy Response				Interface and Durability				Decision Output		
	Δa_{100k} (mm)	$R_{\Delta a}$ (%)	$\sigma_{\max}$ (MPa)	R_σ (%)	A_E^{peak}	q_{avg} (kW/m²)	T_{avg} (°C)	FE	B_q	D_{int}	R_d	ΔN_f (yr)	E_{rep} (kWh/m²)	$J(s)$	Rank
S0: Delay repair	94.7	0.0	3.85	0.0	0.00	0.0	28.0	1	0.00	0.88	0.18	0.0	0.00	0.814	5
S1: Crack sealing	72.5	23.4	3.04	21.0	0.64	8.3	57.8	1	0.50	0.41	0.55	1.9	2.12	0.541	4
S2: Localized patch	61.7	34.8	2.55	33.8	0.79	10.7	66.9	1	0.71	0.28	0.72	3.9	3.66	0.374	3
S3: Thin overlay	53.8	43.2	2.22	42.3	0.89	12.0	73.4	1	0.87	0.19	0.86	6.7	4.84	0.216	1
S4: Deep repair	49.7	47.5	2.04	47.0	0.99	14.7	78.5	1	0.92	0.14	0.89	7.4	7.24	0.239	2

Table 10. Scenario-level simulation results used to evaluate repair behavior under different crack severities, energy states, and repair strategies.

Case	Initial Crack State			Energy State			Repair Setup			Simulation Outputs			Decision Outputs	
	a_0 (mm)	d_0 (mm)	D_c	SOC (%)	PV	A_E	Strategy	t_H (min)	B_q	Δa (mm)	$\sigma_{\max}$ (MPa)	R_d	FE	Risk
C01	35	15	0.12	35	0.35	0.64	Seal	15	0.41	70.8	3.03	0.54	0	Medium
C02	35	15	0.12	60	0.65	0.89	Patch	15	0.63	59.6	2.49	0.71	1	Low
C03	35	15	0.12	85	0.90	0.99	Overlay	15	0.91	51.7	2.12	0.88	1	Low
C04	50	25	0.23	35	0.35	0.64	Seal	15	0.41	76.1	3.27	0.49	0	High
C05	50	25	0.23	60	0.65	0.89	Patch	15	0.63	61.7	2.55	0.72	1	Medium
C06	50	25	0.23	85	0.90	0.99	Overlay	15	0.91	53.8	2.22	0.86	1	Low
C07	65	35	0.36	35	0.35	0.64	Patch	20	0.49	82.4	3.51	0.44	0	High
C08	65	35	0.36	60	0.65	0.88	Overlay	20	0.76	63.5	2.68	0.75	1	Medium
C09	65	35	0.36	85	0.90	0.99	Deep	20	0.94	55.4	2.19	0.90	1	Low
C10	75	45	0.48	35	0.35	0.64	Patch	25	0.49	91.5	3.90	0.37	0	Very high
C11	75	45	0.48	60	0.65	0.88	Overlay	25	0.76	68.1	2.95	0.71	1	Medium
C12	75	45	0.48	85	0.90	0.99	Deep	25	0.94	58.0	2.35	0.88	1	Low

Figure 10 presents the crack depth sensitivity analysis under energy-constrained pavement crack repair, showing how normalized crack depth (d/h) and crack location (ξ_L) influence stress concentration, XFEM damage, crack growth tendency, and post-repair durability. Subfigure (a) shows the normalized stress sensitivity surface S_σ, where higher crack depths generally produce stronger stress concentration, especially around the marked regions C2 and C3; this indicates that deeper cracks are more structurally critical because they transfer higher tensile and shear demand into the surrounding asphalt layer and repair zone. Subfigure (b) extends this behavior to the XFEM damage sensitivity S_D, where the elevated ridges show that deeper cracks and unfavorable crack locations lead to a higher crack damage tendency, confirming that stress concentration and XFEM damage accumulation are physically connected. Subfigure (c) presents the normalized crack growth sensitivity $S_{\Delta a}$, which follows a similar pattern but emphasizes the propagation response: as crack depth increases, the surface rises, showing that deeper cracks are more likely to continue growing even after repair unless the selected strategy provides sufficient structural confinement and bonding support. In contrast, subfigure (d) shows the normalized repair durability response S_R, where higher durability is generally associated with lower normalized crack depth and more favorable crack locations, while durability decreases in regions where stress, damage, and crack growth sensitivities are high. Together, these four surfaces provide a connected interpretation: regions with high S_σ, S_D, and $S_{\Delta a}$ correspond to crack states that are more difficult to repair and more likely to experience residual post-repair deterioration, whereas regions with high S_R indicate repair conditions where the energy-constrained intervention is more durable. This figure complements the previous scenario-level and strategy comparison results by explaining why repair decisions cannot depend only on the selected treatment type, as they must also account for crack depth and location, stress sensitivity, damage tendency, and expected durability. In the context of CERIG-Net, these sensitivity surfaces justify the use of physics-guided graph learning, since the model must learn nonlinear interactions between crack geometry, structural response, damage evolution, repair energy, and durability in order to reliably rank different maintenance strategies.

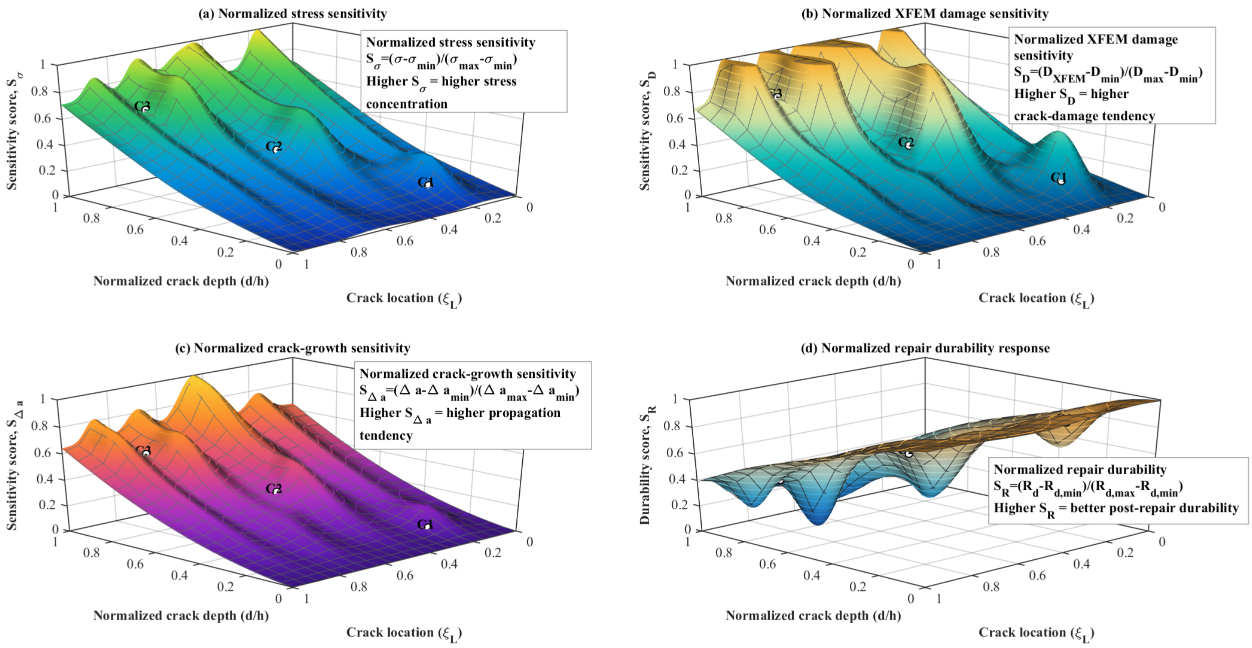

Figure 10. Crack depth sensitivity analysis under energy-constrained pavement crack repair.

https://doi.org/10.3390/math14173149

Table 11 demonstrates that the predicted repair performance is influenced differently by uncertainties in material properties, initial crack geometry, and repair energy availability. Among the crack geometry variables, initial crack depth d_0 produces the strongest structural effect, with an increase from 15 to 45 mm raising the final crack length from 49.5 to 70.4 mm and the maximum principal stress from 2.04 to 3.08 MPa while reducing the durability index from 0.90 to 0.68 and the service life gain from 7.3 to 4.0 years. Initial crack length a_0 shows a similarly important influence, confirming that more severe initial defects reduce the ability of the repair to suppress subsequent deterioration. Material and fracture properties also affect the response, particularly the mode-I fracture energy G_{Ic} and tensile strength σ_n^0. Increasing G_{Ic} from 350 to 650 N/m reduces the final crack length from 63.2 to 48.9 mm and increases R_d from 0.76 to 0.91, demonstrating the importance of fracture resistance in controlling post-initiation crack propagation. The interface fracture energy G_{int} has a stronger effect on interface integrity than the elastic interface stiffness, with increasing G_{int} reducing D_{int} from 0.31 to 0.12. Energy availability is also a dominant source of uncertainty: increasing the battery state of charge from 35% to 85% reduces final crack length from 70.8 to 51.7 mm, maximum stress from 3.03 to 2.12 MPa, and interface damage from 0.42 to 0.12 while increasing durability from 0.54 to 0.88. A comparable response is obtained for the energy amplitude parameter A_E, confirming that sufficient energy delivery is essential for achieving adequate thermal conditioning and interface recovery. Overall, the sensitivity results indicate that crack depth, initial crack severity, fracture resistance, and energy availability are the principal factors governing uncertainty in repair effectiveness, while parameters such as crack inclination and interface stiffness produce comparatively smaller variations. This behavior confirms that reliable repair strategy selection requires simultaneous consideration of structural condition, fracture properties, and available work zone energy as opposed to optimization based on any single parameter.

Table 11. Multi-factor sensitivity of pavement repair performance to material properties, initial crack geometry, and energy availability.

Parameter	Investigated Range	Final Crack Length (mm)	$\sigma_{\max}$ (MPa)	D_{int}	R_d	ΔN_f (yr)	Sensitivity Rank
Material and fracture property uncertainty							
Surface asphalt modulus, E_1	2500–5000 MPa	58.9–50.6	2.47–2.05	0.23–0.16	0.80–0.89	5.6–7.2	6
Tensile strength, σ_n^0	1.20–1.80 MPa	61.4–49.8	2.58–2.01	0.25–0.15	0.78–0.90	5.1–7.4	4
Mode-I fracture energy, G_{Ic}	350–650 N/m	63.2–48.9	2.66–1.98	0.27–0.14	0.76–0.91	4.8–7.6	3
Mode-II fracture energy, G_{IIc}	500–850 N/m	59.7–50.7	2.48–2.06	0.23–0.16	0.80–0.89	5.5–7.2	7
Interface stiffness, K_n	$1.0-5.0 \times 10^6$ MPa/m	57.6–51.5	2.38–2.09	0.26–0.14	0.78–0.91	5.4–7.3	8
Interface fracture energy, G_{int}	150–400 N/m	59.8–50.9	2.45–2.07	0.31–0.12	0.74–0.92	4.9–7.5	5
Initial crack geometry uncertainty							
Initial crack length, a_0	35–75 mm	48.7–68.1	1.99–2.95	0.14–0.32	0.91–0.71	7.5–4.3	2
Initial crack depth, d_0	15–45 mm	49.5–70.4	2.04–3.08	0.15–0.35	0.90–0.68	7.3–4.0	1
Crack inclination, θ_c	0°–25°	51.6–58.7	2.10–2.47	0.17–0.24	0.89–0.79	7.1–5.5	9
Repair energy uncertainty							
Battery state of charge, SOC	35–85%	70.8–51.7	3.03–2.12	0.42–0.12	0.54–0.88	2.1–7.1	1
Energy amplitude, A_E	0.64–0.99	69.5–51.9	2.98–2.13	0.42–0.12	0.55–0.88	2.2–7.0	2
Heating duration, t_H	5–25 min	62.7–51.3	2.63–2.11	0.39–0.10	0.63–0.90	3.6–7.3	4

Note: The nominal reference case corresponds to the thin overlay repair response ($\Delta a = 53.8$ mm, $\sigma_{\max} = 2.22$ MPa, $D_{\mathrm{int}} = 0.19$, $R_d = 0.86$, and $\Delta N_f = 6.7$ yr). Sensitivity rank denotes the relative influence of each parameter on the coupled structural–interface–durability response, with lower rank indicating greater influence.

Table 12 tests whether CERIG-Net can successfully learn the simulation-based relationships from the previous tables, which determine the maintenance performance based on crack severity, thermal energy availability, interface response, repair durability, and repair strategy. The model has very high predictive accuracy for the regression tasks: crack growth prediction, $R^2 = 0.983$; maximum principal stress, $R^2 = 0.978$; repair zone temperature, $R^2 = 0.989$; interface damage, $R^2 = 0.973$; repair durability, $R^2 = 0.981$; and service life gain, $R^2 = 0.976$. These values show that CERIG-Net predicts not just one individual value but the coupled structural and thermal interface response from the XFEM and energy constrained repair simulations. The low error values are further confirmation of this explanation, with the prediction error of crack growth being 1.76 mm and 1.18 mm for the RMSE and MAE, respectively, while the prediction errors for maximum stress, repair temperature, and service life gain are 0.079 MPa, 1.54 °C, and 0.39 years, respectively. These errors are small enough given the engineering range of the simulation to be able to differentiate between weak, moderate, and strong repair responses. Thus, CERIG-Net can predict the feasibility of a repair from the thermal and/or energy perspective with accuracy of 97.6/97.1% and can classify the maintenance class from S0–S4 with accuracy of 96.2/95.8% for the classification tasks. An important property of the ranking task is its performance, with 95.6% ranking accuracy, 95.6% Top-1 accuracy, and $MRR = 0.961$. The repair problem is not just a classification problem but a strategy prioritization problem in which the best treatment should be ranked above feasible alternatives. The uncertainty indicators provide evidence of model reliability, as NLL ranges from 0.054 to 0.079, PICP ranges from 94.3% to 96.0%, and mean variance values are low, which is consistent with the confidence estimates and prediction quality.

Table 12. Full CERIG-Net prediction and decision validation results for simulation-derived pavement repair outputs.

CERIG-Net Task	Prediction Target			Regression/Classification Metrics				Uncertainty Metrics			Decision Metrics	
	Output Type	**Unit/ Class**	**Test Samples**	R^2	**RMSE**	**MAE**	**F1/Acc.**	**NLL**	**PICP**	**Mean σ^2**	**Top-1**	**MRR**
Crack growth prediction, Δa	Regression	mm	Test set	0.983	1.76	1.18	-	0.068	95.1%	0.032	-	-
Maximum principal stress, $\sigma_{\max}$	Regression	MPa	Test set	0.978	0.079	0.054	-	0.073	94.6%	0.039	-	-
Repair temperature, T_{avg}	Regression	°C	Test set	0.989	1.54	1.03	-	0.061	95.9%	0.027	-	-
Interface damage, D_{int}	Regression	0–1	Test set	0.973	0.024	0.017	-	0.079	94.3%	0.043	-	-
Repair durability, R_d	Regression	0–1	Test set	0.981	0.029	0.020	-	0.066	95.6%	0.030	-	-
Service life gain, ΔN_f	Regression	years	Test set	0.976	0.39	0.28	-	0.077	94.8%	0.041	-	-
Energy feasibility, FE	Binary	0/1	Test set	-	-	-	97.6/97.1%	0.054	96.0%	0.025	-	-
Repair strategy, S^*	Multi-class	S0–S4	Test set	-	-	-	96.2/95.8%	0.062	95.2%	0.033	96.2%	0.966
Strategy ranking	Ranking	S0–S4	Test set	-	-	-	95.6%	0.069	94.7%	0.037	95.6%	0.961

Figure 11 presents the pre-repair and post-repair stress hot spot behavior of the pavement crack repair zone, providing a spatial explanation of how the energy-constrained maintenance action redistributes stress and improves repair efficiency. Subfigure (a) shows the pre-repair stress hot spot field, where the highest $\sigma_{\max}^{pre}$ values are concentrated along the crack paths and inside the repair zone boundary, with hot spots H1–H4 identifying the most critical stress amplification regions before intervention. This confirms that the unrepaired cracked pavement is controlled by localized stress concentration around the crack tips and crack edges, which is consistent with the earlier XFEM damage and crack growth results. Subfigure (b) shows the post-repair stress redistribution field, where the stress intensity inside the repair zone is visibly reduced after maintenance, indicating that the repair material and interface bonding help to transfer the load more uniformly across the treated region. Subfigure (c) directly quantifies this improvement using the absolute stress reduction map $\Delta\sigma = \sigma^{pre} - \sigma^{post}$, where the strongest reductions occur near the original crack paths and hot spot zones, proving that the repair is most effective exactly where pre-repair stress concentration was highest. Subfigure (d) classifies the hot spot field into low, moderate, high, and critical zones, showing that the critical regions correspond to the upper portion of the pre-repair stress field and the crack interaction paths inside the repair boundary. Subfigure (e) further supports this interpretation through the stress concentration factor map $K_\sigma = \sigma_{\max}^{pre}/\sigma_{ref}$, where values greater than 1 identify stress amplification zones that require repair prioritization. Finally, subfigure (f) converts the stress redistribution into a repair efficiency map $\eta_\sigma = 100(\sigma^{pre} - \sigma^{post})/\sigma^{pre}$, showing that the repair zone achieves meaningful stress relief across a large portion of the damaged region, with the strongest efficiency concentrated around the former crack hot spots. Overall, this figure connects the crack growth, thermal conditioning, and repair strategy results by demonstrating that the selected maintenance intervention reduces scalar crack length and damage index while also spatially redistributing the stress field, suppressing critical hot spots, and improving repair efficiency within the treated pavement zone. This makes the figure especially important in light of the CERIG-Net validation results, as it shows how the AI model learns from physically meaningful stress reduction and hot spot control patterns rather than relying solely on simplified numerical indicators.

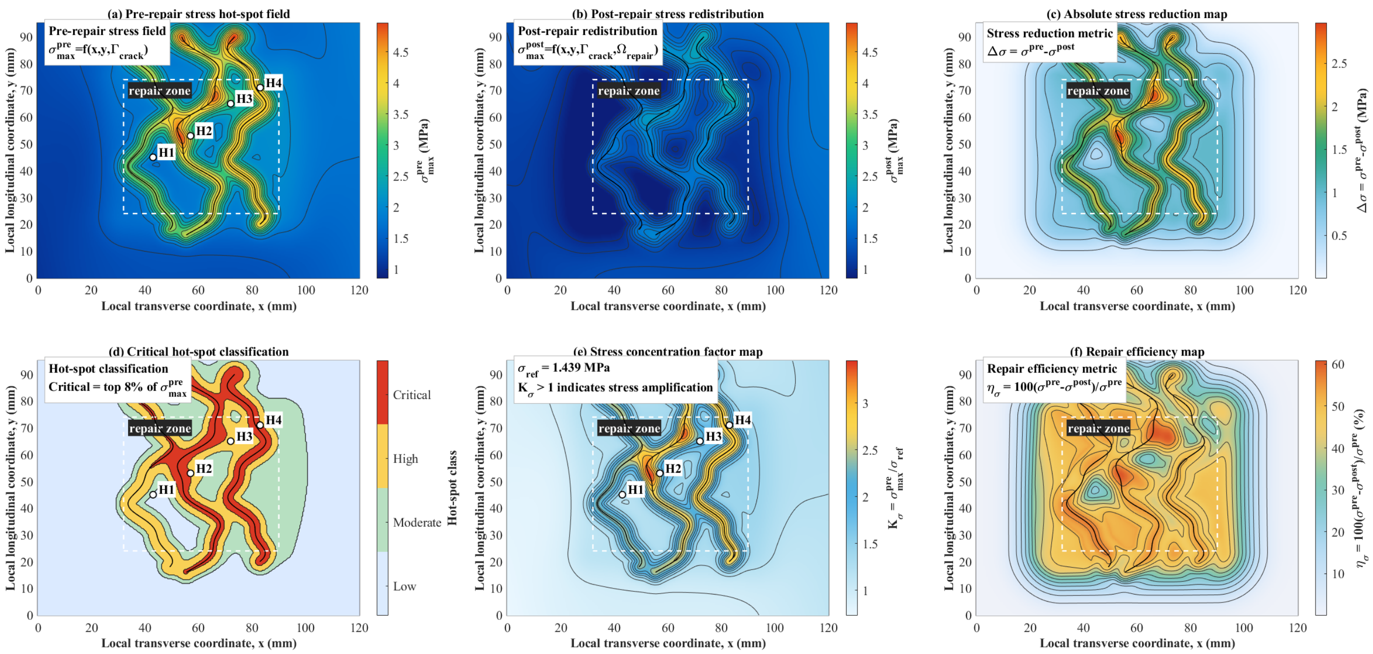

Figure 11. Pre- and post-repair stress hot spot control, stress reduction, and repair efficiency under energy-constrained pavement maintenance.

To provide a direct comparison between CERIG-Net and conventional graph learning architectures, two additional graph baselines were considered using the same input variables, graph connectivity, training–validation–test partitions, and evaluation metrics. The standard GCN baseline applies normalized neighborhood aggregation over the graph without relation-specific edge encoding, physics consistency losses, uncertainty estimation, or the repair strategy ranking mechanism. The standard GAT baseline uses learned node-to-node attention over the same graph topology but does not explicitly distinguish the physical meaning of relationships such as material–crack, energy–thermal, thermal–

interface, interface–response, and response–strategy. These baselines complement the existing random forest, flat MLP, and tabular attention models, enabling the contribution of heterogeneous graph representation and physics-guided learning to be evaluated separately from the general benefit of graph-based modeling.

Table 13 provides a direct comparison between conventional tabular learners, standard graph architectures, CERIG-Net ablations, and the complete physics-guided model. A clear progression is observed as increasingly structured information is introduced into the learning process. The random forest baseline records the weakest overall performance, with $R^2_{\Delta a} = 0.912$, $RMSE_{\Delta a} = 5.21$ mm, $F1_{S^*} = 87.6\%$, and decision agreement of 84.7%. Replacing the tree-based learner with a flat MLP improves the corresponding values to 0.932, 4.46 mm, 90.1%, and 87.6%, respectively, while the tabular attention network further increases $R^2_{\Delta a}$ to 0.946 and reduces $RMSE_{\Delta a}$ to 3.82 mm. These improvements indicate that nonlinear feature interaction and attention mechanisms are beneficial; however, the tabular models still process the crack, material, energy, thermal, interface, and repair variables primarily as correlated features rather than as physically differentiated components of the maintenance system.

Table 13. Expanded ablation and baseline comparison for CERIG-Net under pavement repair strategy optimization.

Model Variant	Regression Performance			Classification Performance			Ranking Performance			Decision Reliability	
	$R^2_{\Delta a}$	$RMSE_{\Delta a}$ (mm)	$R^2_{R_d}$	$Acc._{FE}$	$F1_{FE}$	$F1_{S^*}$	Top-1	Top-3	MRR	DA	EFA
Random forest baseline	0.912	5.21	0.904	89.2%	88.5%	87.6%	85.2%	94.3%	0.852	84.7%	89.2%
Flat MLP without graph structure	0.932	4.46	0.918	91.4%	90.7%	90.1%	88.2%	95.2%	0.883	87.6%	91.4%
Tabular attention network	0.946	3.82	0.934	92.8%	92.1%	91.7%	90.4%	96.4%	0.908	89.6%	92.8%
Standard GCN	0.955	3.31	0.944	93.7%	93.1%	92.5%	91.5%	96.8%	0.918	90.8%	93.7%
Standard GAT	0.962	2.87	0.951	94.6%	94.0%	93.2%	92.7%	97.1%	0.929	91.7%	94.6%
Graph model without physics loss	0.969	2.52	0.958	95.5%	95.0%	93.8%	93.6%	97.4%	0.937	92.5%	95.5%
CERIG-Net without uncertainty branch	0.976	2.13	0.971	96.2%	95.7%	94.8%	94.5%	97.8%	0.948	93.9%	96.2%
CERIG-Net without ranking loss	0.978	1.98	0.974	96.8%	96.2%	94.2%	93.4%	97.5%	0.934	92.9%	96.8%
Full CERIG-Net	0.983	1.76	0.981	97.6%	97.1%	95.8%	96.2%	98.6%	0.966	95.6%	97.6%

The standard GCN and GAT baselines provide a more rigorous assessment of whether the gains of CERIG-Net arise merely from graph-based learning. The GCN achieves $R^2_{\Delta a} = 0.955$, $RMSE_{\Delta a} = 3.31$ mm, $F1_{S^*} = 92.5\%$, and $MRR = 0.918$, outperforming the tabular attention network and confirming the benefit of explicitly representing interactions among pavement state variables. The GAT further improves these results to $R^2_{\Delta a} = 0.962$, $RMSE_{\Delta a} = 2.87$ mm, $F1_{S^*} = 93.2\%$, Top-1 accuracy of 92.7%, and $MRR = 0.929$, showing that learned attention provides an additional advantage over fixed neighborhood aggregation. Nevertheless, both standard architectures remain below the graph model without physics loss, which reaches $R^2_{\Delta a} = 0.969$, $RMSE_{\Delta a} = 2.52$ mm, $F1_{S^*} = 93.8\%$, and decision agreement of 92.5%. This result indicates that the improvement cannot be attributed to graph representation alone; explicitly preserving the heterogeneous crack–energy–thermal interface response relationships provides an additional benefit beyond standard GCN and GAT formulations.

The ablation results further quantify the contribution of the physics-guided, uncertainty, and ranking components. Introducing the complete physics-guided CERIG-Net improves $R^2_{\Delta a}$ from 0.969 for the graph model without physics loss to 0.983 while reducing

$RMSE_{\Delta a}$ from 2.52 to 1.76 mm. Over the same comparison, $R^2_{R_d}$ increases from 0.958 to 0.981, energy feasibility accuracy increases from 95.5% to 97.6%, strategy F1-score increases from 93.8% to 95.8%, Top-1 ranking accuracy increases from 93.6% to 96.2%, and decision agreement increases from 92.5% to 95.6%. These gains support the role of the physics consistency constraints in preventing the graph learner from relying exclusively on statistical correlations and in encouraging agreement with the energy feasibility, thermal conditioning, interface damage, and durability relationships represented by the underlying simulation framework.

The remaining ablations show that the uncertainty and ranking components contribute primarily to decision reliability rather than simply increasing regression accuracy. Removing the uncertainty branch decreases Top-1 accuracy from 96.2% to 94.5%, MRR from 0.966 to 0.948, and decision agreement from 95.6% to 93.9%. Similarly, removing the ranking loss produces relatively strong regression performance, with $R^2_{\Delta a} = 0.978$ and $RMSE_{\Delta a} = 1.98$ mm, but causes a more pronounced deterioration in strategy-level performance: $F1_{S^*}$ decreases to 94.2%, Top-1 accuracy to 93.4%, MRR to 0.934, and decision agreement to 92.9%. The full CERIG-Net achieves the strongest combined performance, with $R^2_{\Delta a} = 0.983$, $RMSE_{\Delta a} = 1.76$ mm, $R^2_{R_d} = 0.981$, $F1_{FE} = 97.1\%$, $F1_{S^*} = 95.8\%$, Top-1 and Top-3 accuracy of 96.2% and 98.6%, respectively, $MRR = 0.966$, $DA = 95.6\%$, and $EFA = 97.6\%$. Relative to the standard GAT, the full model improves $R^2_{\Delta a}$ by 0.021, reduces crack growth RMSE by 1.11 mm, and increases decision agreement by 3.9 percentage points. Within the simulation-derived evaluation domain, these results demonstrate that the advantage of CERIG-Net arises from the combined use of heterogeneous physical graph representation, relation-conditioned message passing, physics-guided consistency constraints, uncertainty modeling, and explicit repair strategy ranking rather than from the use of a generic graph neural network alone.

Figure 12 illustrates the crack tip displacement field response associated with XFEM-based crack evolution, providing a detailed local view of how displacement discontinuity, crack opening, and displacement gradient concentration develop around the crack front. Subfigure (a) presents the measured displacement vector field, where the displacement arrows radiate around the crack tip and reveal the localized deformation pattern generated by crack opening and stress concentration. This confirms that the crack tip region is the dominant zone controlling fracture response, which supports the use of XFEM enrichment in the pavement crack simulation. Subfigure (b) shows the horizontal crack tip displacement field, where the strongest displacement intensity is concentrated immediately ahead of the crack tip, indicating that horizontal displacement discontinuity contributes to crack extension along the pavement surface direction. Subfigure (c) presents the vertical crack tip opening field, where the positive and negative lobes around the crack tip represent asymmetric opening and closing behavior, reflecting the mixed-mode nature of pavement cracking under wheel loading and thermal repair effects. Subfigure (d) shows the fitted XFEM crack tip displacement field, which closely reproduces the localized displacement concentration around the crack tip, demonstrating that the XFEM approximation can represent the measured displacement pattern without requiring continuous remeshing. Subfigure (e) combines the horizontal and vertical responses into an equivalent displacement magnitude field, showing that the highest displacement demand remains concentrated near the crack tip and gradually decays away from the fracture zone. Finally, subfigure (f) identifies the crack tip gradient hot spot field, where steep displacement gradients are localized near the crack front, indicating the regions most vulnerable to crack propagation. Overall, this figure complements the previous XFEM damage and stress hot spot figures by showing the displacement-based mechanism behind crack evolution: stress concentration generates localized crack tip displacement, displacement gradients drive damage accumulation, and the resulting crack growth response becomes a key simulation-derived input for evaluating repair effectiveness and training CERIG-Net to rank energy-constrained pavement maintenance strategies.

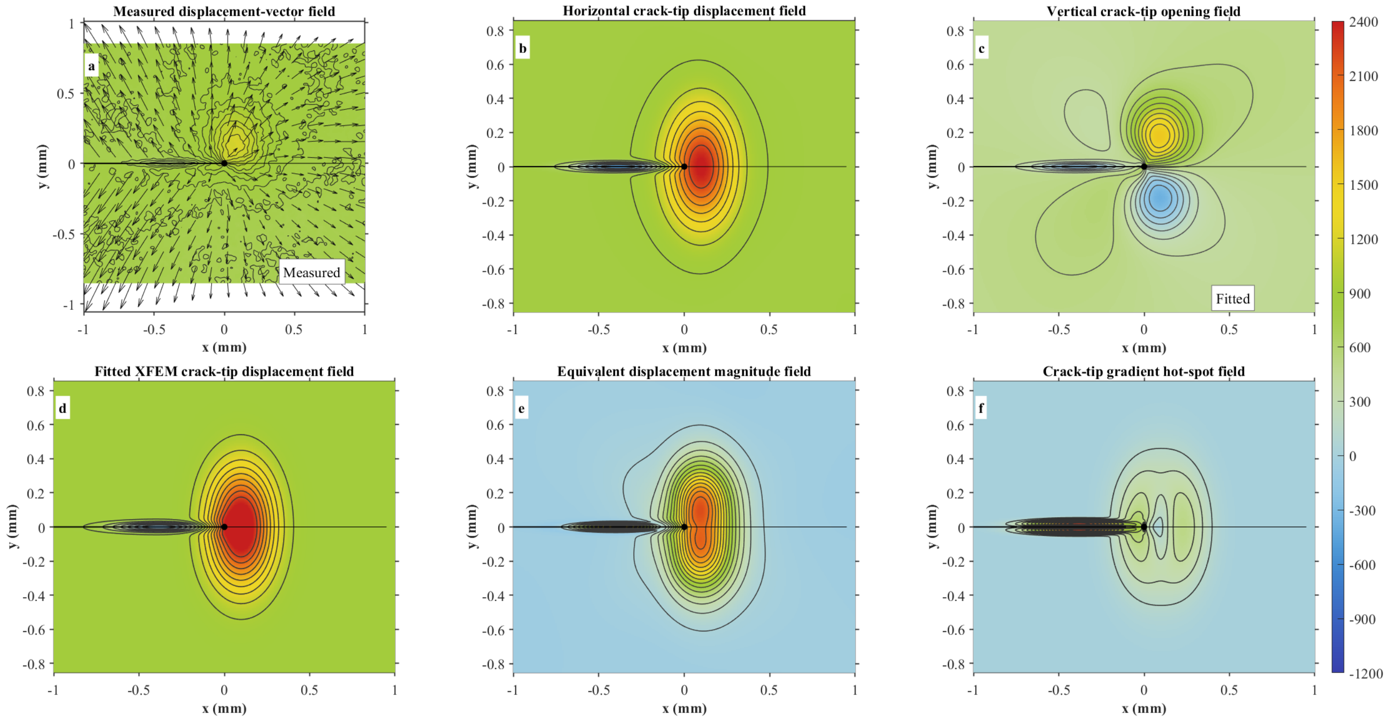

Figure 12. XFEM crack tip displacement, opening, and gradient hot spot fields under pavement crack evolution.

Table 14 consolidates the complete simulation-to-decision logic of the proposed framework by comparing the baseline no-repair condition, the structurally strongest repair option, the best balanced repair option, and the final CERIG-Net-selected maintenance decision. The baseline no-repair case confirms the severity of the untreated deterioration path, where the crack reaches 94.7 mm, the maximum principal stress remains high at 3.85 MPa, the durability index is only 0.18, and no gain in service life is achieved, representing progressive crack propagation and structural weakening. In contrast, the deep repair option provides the best structural-only recovery, reducing the crack length to 49.7 mm, lowering the maximum principal stress to 2.04 MPa, achieving the highest crack growth reduction of 47.5%, and producing the strongest durability index of 0.89, with a service life gain of 7.4 years. However, this option also requires the highest thermal energy support, with $T_{avg} = 78.5$ °C, $A_E = 0.99$, and stronger energy demand, which explains why it is not selected as the final optimal decision despite its superior structural performance. The thin overlay strategy provides a more balanced response, reducing the crack length to 53.8 mm, decreasing the maximum stress to 2.22 MPa, achieving 43.2% crack growth reduction, reaching a thermally adequate repair zone temperature of 73.4 °C, maintaining energy feasibility $(FE = 1)$, improving bonding quality to $B_q = 0.87$, and producing a high durability index of 0.86 with a service life gain of 6.7 years. Therefore, CERIG-Net selects the thin overlay option because it provides the best compromise between crack suppression, stress reduction, feasible thermal conditioning, interface bonding recovery, durability improvement, and energy-aware practicality. The final improvement row confirms the magnitude of this decision relative to the no-repair condition: crack length is reduced by 40.9 mm, maximum stress decreases by 1.63 MPa, crack growth reduction improves by

43.2%, average repair temperature increases by 45.4 °C, bonding quality improves by 0.87, durability increases by 0.68, and service life improves by 6.7 years.

Table 14. Final optimal repair decision and performance interpretation produced by the full CERIG-Net framework.

Decision Item	Structural Benefit			Energy/Thermal Feasibility			Durability and Decision Quality			Interpretation
	Δa (mm)	$\sigma_{\max}$ (MPa)	$R_{\Delta a}$ %	T_{avg} (°C)	A_E	FE	B_q	R_d	ΔN_f (yr)	
No-repair baseline	94.7	3.85	0.0	28.0	0.00	1	0.00	0.18	0.0	Progressive deterioration
Best structural-only choice: Deep repair	49.7	2.04	47.5	78.5	0.99	1	0.92	0.89	7.4	Highest structural recovery but larger energy demand
Best balanced choice: Thin overlay	53.8	2.22	43.2	73.4	0.89	1	0.87	0.86	6.7	Selected optimal strategy
CERIG-Net selected decision	53.8	2.22	43.2	73.4	0.89	1	0.87	0.86	6.7	Optimal pavement maintenance decision
Decision improvement vs. no-repair baseline	−40.9	−1.63	+43.2	+45.4	+0.89	feasible	+0.87	+0.68	+6.7	Crack control, bonding recovery, and service life extension

Figure 13 presents the convergence behavior of the full CERIG-Net training process and its major task-specific loss components. The figure also provides important evidence that the model does not exhibit significant overfitting within the investigated simulation domain. Subfigure (a) shows that the total training and validation losses decrease together during the warm-up/transient stage and remain closely aligned as training progresses toward the stable convergence region. The absence of a widening gap between the two curves near the best validation epoch around epoch 160 indicates that the learned model is not simply fitting the training graphs at the expense of validation performance. Instead, the validation loss continues to improve in parallel with the training loss until the best validation checkpoint is reached, after which early stopping prevents unnecessary additional fitting. Subfigure (b) shows a similar pattern for XFEM damage prediction, where both the training and validation losses decrease smoothly and stabilize without divergence, supporting the conclusion that the model generalizes its crack response learning beyond the training subset. Subfigure (c) demonstrates that the energy feasibility loss follows the same consistent behavior, indicating that the model learns to distinguish feasible and infeasible PV battery repair states without unstable validation degradation. Subfigure (d) further shows that the repair strategy ranking loss decreases steadily for both training and validation, suggesting that the ordering of candidate repair actions is learned in a stable manner rather than memorized from the training set. Subfigure (e) confirms that the physics consistency loss also decreases and stabilizes at a low level on both subsets, which supports that the physics-guided constraints improve generalization instead of only improving in-sample fitting. Finally, subfigure (f) shows that the validation performance metrics, including damage R^2, ranking accuracy, and repair F1-score, improve progressively and then plateau at high stable values, again without any late-stage collapse or oscillatory behavior that would indicate overfitting. It should also be emphasized that these validation curves correspond to the dedicated validation subset used for model selection and early stopping, whereas the final results reported in the subsequent tables are obtained on the independent test subset. Overall, Figure 13 indicates stable optimization, good validation agreement, and no clear evidence of significant overfitting in the CERIG-Net training process. Although the validation and convergence results demonstrate that CERIG-Net generalizes effectively across unseen cases within the investigated simulation domain, a distinction must be made between numerical generalization and direct generalization to field pavement maintenance. The training database is generated from a controlled finite-element/XFEM environment, and cannot fully reproduce the field-level variability associated with material heterogeneity, pavement aging, moisture, seasonal temperature changes, construction tolerances, irregular traffic spectra, uncertain repair placement, interface contamination, and measurement noise. The potential simulation-to-reality gap is reduced by exposing CERIG-Net to broad variations in crack geometry, material and fracture properties, loading conditions, repair configuration, interface quality, thermal conditioning, and PV battery energy availability. In addition, the heterogeneous graph structure preserves physically meaningful dependency pathways, while the physics-guided loss constrains predictions according to structural, fracture, thermal, interface, and energy relationships rather than relying exclusively on statistical correlations. The uncertainty estimation branch provides an additional safeguard by identifying predictions associated with lower confidence within sparsely represented regions of the simulated parameter space. Nevertheless, while these mechanisms improve robustness within and around the modeled domain, they do not constitute direct evidence of field transferability. Consequently, laboratory and field measurements remain necessary for external validation of CERIG-Net, followed where required by recalibration, transfer learning, or domain adaptation before operational deployment for pavement maintenance.

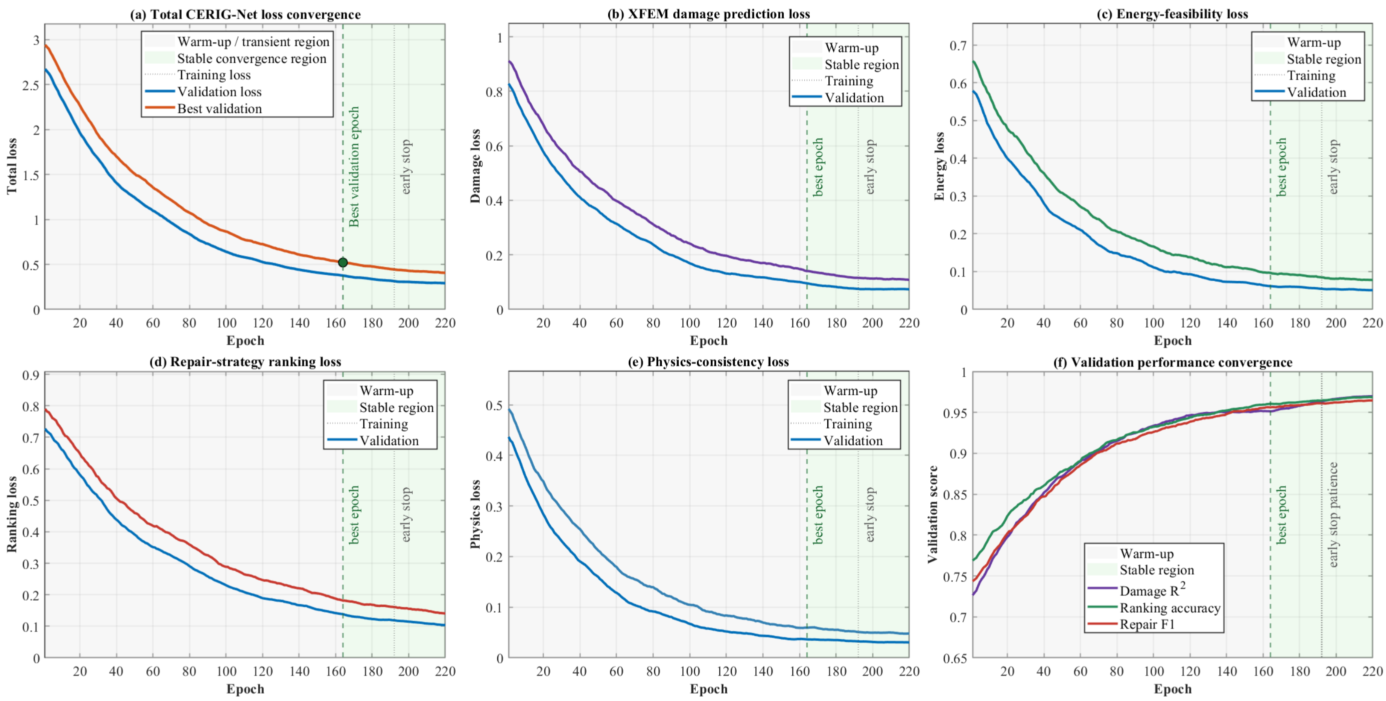

Figure 13. CERIG-Net loss convergence and validation performance during physics-guided repair strategy learning.

5. Conclusions and Future Work

This study has developed and numerically evaluated a simulation-driven framework for energy-constrained pavement crack maintenance by integrating XFEM-based crack evolution, PV battery-controlled thermal conditioning, cohesive repair interface behavior, and repair strategy assessment based on the developed CERIG-Net framework. CERIG-Net formulates pavement maintenance as a coupled structural–thermal energy decision problem in which crack propagation, repair activation, energy-limited heating, interface response, post-repair stress redistribution, and maintenance performance are evaluated within the same computational environment. Under the investigated numerical conditions, the results show that available PV battery energy directly influences the attainable repair heat flux, repair zone temperature, bonding quality, interface damage, and resulting durability, demonstrating that thermally assisted repair effectiveness depends not only on the selected structural treatment but also on whether sufficient energy is available to achieve adequate thermal conditioning and interface recovery. Among the evaluated maintenance strategies, thin overlay provided the most favorable overall balance under the reference pavement and energy conditions, reducing the simulated final crack length from 94.7 mm in the delayed-repair case to 53.8 mm, decreasing the maximum principal stress from 3.85 MPa to 2.22 MPa, reducing interface damage to 0.19, achieving a durability index of 0.86, and producing an estimated service life gain of 6.7 years while remaining energy-feasible. Deep repair produced slightly stronger purely structural recovery, reducing the final crack length to 49.7 mm and the maximum stress to 2.04 MPa, but required 7.24 kWh/m^2 of repair energy compared with 4.84 kWh/m^2 for the thin overlay strategy. Thus, CERIG-Net's selection of thin overlay should not be interpreted as indicating general superiority but rather its providing the best compromise among crack suppression, stress reduction, thermal adequacy, interface integrity, durability, estimated service life improvement, and energy demand for the specific investigated conditions. CERIG-Net demonstrated strong predictive and strategy ranking performance on held-out cases generated within the simulation domain and provided a consistent mechanism for integrating crack state, material properties, repair energy availability, thermal response, interface behavior, durability, and candidate maintenance actions; however, because the training and evaluation database remains simulation-derived and does not fully represent field variability associated with material heterogeneity, pavement aging, moisture, construction quality, traffic spectra, repair workmanship, environmental exposure, and measurement uncertainty, the present numerical results do not establish field-level generalization, operational superiority over conventional pavement management practices, or readiness for direct real-world deployment. The reported AI performance should be interpreted as evidence of generalization within the investigated numerical parameter space, rather than as direct validation under unrestricted field conditions. Future work should prioritize laboratory and field validation of both the XFEM-based repair responses and CERIG-Net predictions using measured crack propagation, repair zone temperature, interface bonding, post-repair stress response, and long-term deterioration data in order to quantify the simulation-to-reality gap and support model recalibration where required. Subsequent extensions may incorporate transfer learning or domain adaptation, seasonal temperature and moisture variation, viscoelastic and aging-dependent asphalt behavior, additional repair strategies, explicit cost and carbon emission objectives, and larger-scale pavement management constraints. Network-level maintenance planning, real-time sensing integration, digital twin updating, and uncertainty-aware adaptive repair scheduling should be considered only after performing successful external validation.

Author Contributions: Conceptualization, N.L., M.Q.A.-J. and M.A.; methodology, N.L., M.Q.A.-J., M.A. and A.A.; software, N.L. and M.A.; validation, M.Q.A.-J., A.A., N.H.A. and K.H.A.; formal analysis, N.L., M.A. and A.A.; investigation, N.L., M.Q.A.-J. and M.A.; resources, N.H.A., K.H.A., M.K.A. and S.A.A.; data curation, N.L., M.A. and M.K.A.; writing—original draft preparation, N.L., M.Q.A.-J. and M.A.; writing—review and editing, A.A., N.H.A., K.H.A., M.K.A. and S.A.A.; visualization, N.L. and M.A.; supervision, M.Q.A.-J. and S.A.A.; project administration, M.Q.A.-J., A.A. and S.A.A. All authors have read and agreed to the published version of the manuscript.

Funding: The authors extend their appreciation to the Deanship of Scientific Research at Northern Border University, Arar, KSA for funding this research work through the project number NBU-FPEJ-2026-2119-01.

Data Availability Statement: The data presented in this study are available on request from the corresponding author. The data are not publicly available due to security and research confidentiality considerations related to the generated simulation dataset.

Acknowledgments: The authors extend their appreciation to the Deanship of Scientific Research at Northern Border University, Arar, KSA for funding this research work through the project number NBU-FPEJ-2026-2119-01.

Conflicts of Interest: The authors declare no conflicts of interest.

References

1. Min, W.; Lu, P.; Liu, S.; Wang, H. A Review of Crack Sealing Technologies for Asphalt Pavement: Materials, Failure Mechanisms and Detection Methods. *Coatings* **2025**, *15*, 836. [CrossRef]
2. Alae, M.; Ling, M.; Haghshenas, H.F.; Zhao, Y. Three-Dimensional Finite Element Analysis of Top-Down Crack Propagation Mechanisms in Asphalt Pavements. *Eng. Fract. Mech.* **2021**, *248*, 107736. [CrossRef]
3. Xia, X.; Han, D.; Zhao, Y.; Xie, Y. Investigation of Asphalt Pavement Crack Propagation Based on Finite Element Simulation. *Case Stud. Constr. Mater.* **2023**, *19*, e02247. [CrossRef]
4. Alrashydah, E.; Papagiannakis, A.T. Asphalt Concrete Crack Propagation Parameters from XFEM Simulation. *Int. J. Pavement Eng.* **2023**, *24*, 1–14. [CrossRef]
5. Xie, J.; Xu, H.; Huang, T. Simulation Study on Crack Extension Law of Asphalt Pavement. *Front. Built Environ.* **2024**, *10*, 1463012. [CrossRef]
6. Li, S.; Ma, T.; Wang, D. Photovoltaic Pavement and Solar Road: A Review Article. *Sustain. Energy Technol. Assess.* **2023**, *55*, 102933. [CrossRef]
7. Wang, S.; Zhang, H.; Du, C.; Wang, Z.; Tian, Y.; Yao, X. Mechanical Performance of Patched Pavements with Different Patching Shapes Based on 2D and 3D Finite Element Simulations. *Infrastructures* **2024**, *9*, 61. [CrossRef]
8. Chen, S.; Wei, L.; Huang, C.; Qin, Y. A Review on the Technologies and Efficiency of Harvesting Energy from Pavements. *Energies* **2025**, *18*, 3959. [CrossRef]
9. Al-Jamal, M.Q.; Alsarhan, A.; Aljamal, Q.; AlJamal, M.; Khassawneh, B.S.; Salhi, A.; Hayat, H. Integrating Generative Design and Artificial Intelligence for Optimized Energy-Efficient Composite Facades in Next-Generation Smart Buildings. *Sustainability* **2026**, *18*, 2379. [CrossRef]
10. Al-Jamal, M.Q.; Alsarhan, A.; Aljamal, Q.; AlJamal, M.; Khassawneh, B.S.; Al Nuaim, A.; Al Nuaim, A. AI-Enabled System-of-Systems Decision Support: BIM-Integrated AI-LCA for Resilient and Sustainable Fiber-Reinforced Façade Design. *Information* **2026**, *17*, 126. [CrossRef]
11. Shajan, A.M.; Piska, R.; Natarajan, S. Study of Mixed-Mode Fracture in Functionally Graded Material Using an Adaptive Phase-Field Fracture Model. *Compos. Struct.* **2024**, *327*, 117708. [CrossRef]
12. Tamagusko, T.; Correia, M.G.; Ferreira, A. Machine Learning Applications in Road Pavement Management: A Review, Challenges and Future Directions. *Infrastructures* **2024**, *9*, 213. [CrossRef]
13. Boonsiripant, S.; Athan, C.; Jedwanna, K.; Lertworawanich, P.; Sawangsuriya, A. Comparative analysis of deep neural networks and graph convolutional networks for road surface condition prediction. *Sustainability* **2024**, *16*, 9805. [CrossRef]
14. Lu, L.; D'Avigneau, A.M.; Pan, Y.; Sun, Z.; Luo, P.; Brilakis, I. Modeling heterogeneous spatiotemporal pavement data for condition prediction and preventive maintenance in digital twin-enabled highway management. *Autom. Constr.* **2025**, *174*, 106134. [CrossRef]
15. Zhou, Q.; Al-Qadi, I.L. Graph neural networks to simulate flexible pavement responses using three-dimensional finite element analysis data. *Transp. Res. Rec. J. Transp. Res. Board* **2024**, *2678*, 1111–1127. [CrossRef]
16. Liu, F.; Al-Qadi, I.L. Physics-informed graph neural network for 3D spatiotemporal structural response modeling of flexible pavements. *Eng. Appl. Artif. Intell.* **2025**, *162*, 112391. [CrossRef]
17. Du, C.; Liu, Q.; Wang, C.; Zhang, Z.; Liu, P.; Oeser, M. Effects of Patching on the Cracking Performance of Asphalt Pavements Based on a Macrostructure-Based Heterogeneous Finite Element Method. In *Eleventh International Conference on the Bearing Capacity of Roads, Railways and Airfields*; CRC Press: Boca Raton, FL, USA, 2022; pp. 403–412.
18. Zhang, Y.; Ma, T.; Yang, H.; Cao, S.; Wang, Y. Solar Energy Harvesting from the Photovoltaic/Thermal (PV/T) Pavement: Energy Performance Analyses and Comparison Considering Ground Influence. *Sustain. Cities Soc.* **2023**, *99*, 104895. [CrossRef]

19. Latifi, M.; Darvishvand, F.G.; Khandel, O.; Nowsoud, M.L. A Deep Reinforcement Learning Model for Predictive Maintenance Planning of Road Assets: Integrating LCA and LCCA. *arXiv* **2021**, arXiv:2112.12589.
20. Yao, L.; Dong, Q.; Jiang, J.; Ni, F. Deep Reinforcement Learning for Long-Term Pavement Maintenance Planning. *Comput.-Aided Civ. Infrastruct. Eng.* **2020**, *35*, 1230–1245. [CrossRef]
21. Jiang, Z.; Li, C.; Lacidogna, G. Crack propagation and intelligent prediction in asphalt pavements under moving loads. *Int. J. Pavement Res. Technol.* **2026**, 1–16. [CrossRef]
22. Li, Q.; Chen, Z.; Luo, S. Reflection Crack Analysis of Asphalt Overlay on Cement Concrete Pavement Based on XFEM. *Adv. Civ. Eng.* **2021**, *2021*, 1230447. [CrossRef]
23. Islam, M.R.; Vallejo, M.J.; Tarefder, R.A. Crack Propagation in Hot Mix Asphalt Overlay Using Extended Finite-Element Model. *J. Mater. Civ. Eng.* **2017**, *29*, 04016296. [CrossRef]
24. Wu, Y.; Xue, J.; Yu, Y.; Shi, C.; Fan, Y.; Wang, H.; Yang, J.; Gong, M.; Huang, W. Research of Reflective Crack in Asphalt Pavement Using SCB Specimen and XFEM: From Laboratory Test to Numerical Simulation. *Constr. Build. Mater.* **2023**, *406*, 133419. [CrossRef]
25. Hayajneh, M.T.; AL-Oqla, F.M.; AL-Jamal, M.Q. Statistical modeling and optimization of the mechanical performance of natural fiber-reinforced polyolefin composites by applying response surface methodology. *J. Compos. Mater.* **2026**, 00219983261455138. [CrossRef]
26. Muixí, A.; Marco, O.; Rodríguez-Ferran, A.; Fernández-Méndez, S. A Combined XFEM Phase-Field Computational Model for Crack Growth Without Remeshing. *Comput. Mech.* **2021**, *67*, 231–249. [CrossRef]
27. Jafari, A.; Broumand, P.; Vahab, M.; Khalili, N. An eXtended Finite Element Method Implementation in COMSOL Multiphysics: Solid Mechanics. *Finite Elem. Anal. Des.* **2022**, *202*, 103707. [CrossRef]
28. Kim, Y.-R.; Allen, D.H.; Little, D.N. Damage-Induced Modeling of Asphalt Mixtures Through Computational Micromechanics and Cohesive Zone Fracture. *J. Mater. Civ. Eng.* **2005**, *17*, 477–484. [CrossRef]
29. Jiang, H.; Ren, Y.; Liu, Z.; Zhang, S.; Wang, X. Evaluations of Failure Initiation Criteria for Predicting Damages of Composite Structures Under Crushing Loading. *J. Reinf. Plast. Compos.* **2018**, *37*, 1279–1303. [CrossRef]
30. Marler, R.T.; Arora, J.S. The Weighted Sum Method for Multi-Objective Optimization: New Insights. *Struct. Multidiscip. Optim.* **2010**, *41*, 853–862. [CrossRef]
31. Azzouz, R.; Bechikh, S.; Ben Said, L. Dynamic Multi-Objective Optimization Using Evolutionary Algorithms: A Survey. In *Recent Advances in Evolutionary Multi-Objective Optimization*; Springer: Berlin/Heidelberg, Germany, 2016; pp. 31–70.
32. Courant, R. Variational methods for the solution of problems of equilibrium and vibrations. *Bull. Am. Math. Soc.* **1943**, *49*, 1–23. [CrossRef]